Exchange bias in Co/MnPd SYSTEM

Cristina Claudia Macovei

THÈSE

présentée par

Cristina Claudia MACOVEI

pour obtenir le titre de

DOCTEUR DE L'UNIVERSITÉ JOSEPH FOURIER

Spécialité: **PHYSIQUE**

Décalage d'échange dans le système Co/MnPd

Data de soutenance: le 11 Mars 2008

Composition du Jury :

M. Labrune (rapporteur)
S. Mangin (rapporteur)
E. Beaugnon (président)
D. Fiorani (examinateur)
B. Rodmacq (examinateur)
D. Givord (directeur de thèse)

Thèse préparée au sein de l'**Institut Néel- CNRS- Grenoble**
25 Av des Martyrs, BP 166, 38042 Grenoble Cedex 9

Magnétisme *: « un joli sujet de conversation »*

Gustave Flaubert

Acknowledgments

This thesis was prepared in the Institut Néel -CNRS, Grenoble, and it would have not been realized without much help from numerous people. I thank Mr.**Joel Cibert** directory of the Institut Néel to accepting me in this great team.

I express my gratitude to Mr. **Michel Labrune** and Mr. **Stéphane Mangin** who accepted to report my thesis. I'm very grateful for the interest that they showed for my work, not only for the parts which are based on their model but also for the other parts of my work.

To Dr. **Dino Fiorani**, Mr. **Eric Beaugnon** and Mr. **Bernard Rodmacq** a special thank you for accepting to be part of the Jury.

I would like to thank my supervisor Dr. **Dominique Givord** for accepting me as his PhD student and for his useful advice on experiments. I learned about him as both a devoted teacher and a person who always thinks of the development of science. Things I learned from him are not only experimental skills but also patience in work, which I think is very important for scientific research and the fact that not every time the things are looking good but never giving up the hope.

I special thank you to the group MCBT from the Institut Néel. I would like to thank **Olivier Bourgeois** who was kind to co-supervise the work during my PhD and also a great thank you to **Emmanuel Andre** from who I learned a lot of things about lithography.

Beside, this thesis would not been completed if there had not been help from many staffs in Institut Nèel including: **Ian Vogel** and **Stefania Pizzini** thank you for all the discussions about exchange bias systems, **Nora Dempsey** thank you for the kindness and all your help for the VSM measurements during my first days in the lab.

I would also like to thank all the persons from the technical department: **Didier Dufeu** "who will be the happiest when I'm leaving "(le VSM est bouché!!!!!!!!!!), **Eric Eyraud** for al the advises how to use the Squid, **Philippe David** to inviting me to all this great concerts, **Annick Liénard** for the SEM and EDX analysis. I would like to express my sincere thanks to them for their help during experimental time and not only.

Acknowledgements

I thank also to all the persons from the administration and informatics department especially: **Veronique Fauvel, Sabine Dominques -Gadal, Elliane Foret** and **Julien Michel** for al their help and support.

To all my roumanian friends from the lab: **Helga, Mihai, Bogdana, Natalia, Florin,** thank you for all the time spend together and for all the nice memories.

To all my friends from the group *grenoble321:* **Cristina, Justinian, Diana, Bogdan, Alina, Sorin** and all the others thank you for all the excursions and the great parties!!!!!!!

To **Liliana** and **Lucian** who have a special role in my life, I'm grateful that I hade the opportunity to share a part of my time with you.

Last but not least, I thank to **my family** who encourage and supported me during this period.

Finally an enormous hug for **Dan** (my husband), whom I discovered at the same time as my passion for physics…Thank you for your patience, love and support during al these years and your capacity to just put up with me!

To everyone THANK YOU!!!!!!!!!!!

Cristina Claudia Macovei Cenda
February, 2008
Grenoble

Content

Introduction

Chapter 1: Exchange bias: systems and models

1.1. The exchange bias phenomenon
1.1.1. Qualitative description……**18**

1.2. Physical parameters governing exchange-bias
1.2.1. Exchange bias and coercive field……..….19
1.2.2. Field cooling (FC) and zero field cooling (ZFC)……...20
1.2.3. Thickness dependence……....21
FM thickness
AFM thickness
1.2.4. Temperature dependence and blocking temperature……..22
1.2.5. Negative and positive exchange bias……..23
1.2.6. Asymmetry of the hysteresis loops-training effect…….24

1.3. Exchange bias systems……...**25**

1.4. Models and theories
1.4.1. Meiklejohn-Bean's model…….……...….26
1.4.2. Interfacial domain wall
1.4.2.1. Néel-Mauri's model……28
1.4.3. Frustration
1.4.3.1. Malozemoff's model……...30
1.4.4. Perpendicular coupling
1.4.4.1. Koon's model……..32
1.4.4.2. Kiwi's model……...34
1.4.5. Compensated versus non compensated interfaces
1.3.5.1. Stamps approach…….....36
1.4.6. Final remarks…….…….38

References Chapter 1……**39**

Chapter 2: Introduction to magnetization reversal processes and magnetic after effect

2.1. Coercivity
2.1.1. The classical Stoner-Wohlfarth model……..43
2.1.2. Magnetic reversal in real systems ……45
2.1.2.1. Nucleation and expansion……46
2.1.2.2. Domain wall pinning……47

2.2. Thermal activation in coercive systems……**48**
2.2.1. Fatuzzo-Labrune's model……..51
2.2.2. Large distribution of energy barriers……54
2.2.3. Coercive field model……56

References Chapter 2……**58**

Chapter 3: Experimental techniques

3.1. Sample preparation
3.1.1. Sputtering deposition…….. ……61
3.1.2. Film protection……63

3.2. Structural characterisation
3.2.1. X-ray diffraction (XRD)……..64
3.2.2. Scanning electronic microscope (SEM)……...65
3.2.3. Energy dispersive X-ray (EDX) analysis……....66
3.2.4. X-ray reflectometry (XRR)
3.2.4.1. The principle……68
3.2.4.2. Film density……..69
3.2.4.3. Film thickness……...70
3.2.4.4. Surface roughness ……71

3.3. Magnetization measurements
3.3.1. VSM magnetometer……72
3.3.3.1. Oxford VSM system……73
3.3.2. Squid magnetometer……....73
3.3.2.1. Quantum design system……75

References Chapter 3……**77**

Chapter 4: Preparation and structural characterisation of the sample

4.1. MnPd phase diagram……**79**

4.2. Sample preparation……**81**

4.3. Structural and topological characterisation
4.3.1. X-ray diffraction on MnPd sample (XRD)……....82
4.3.2. Scanning electronic microscope analysis (SEM)……...84
4.3.3. Energy dispersive X-ray (EDX) analysis……...85
4.3.4. X-ray reflectometry (XRR)……86
4.3.5. Co thickness derived from magnetization measurements……..88

4.4. Conclusions……**89**

References Chapter 4……**90**

Chapter 5: Exchange- biased hysteresis loops

5.1. Observing exchange bias at T=15K……..**91**

5.2. Exchange bias and coercive field as a function of temperature……**94**

5.3. Additional measurements of the hysteresis loops in sample S_1 and S_2
5.3.1. Hysteresis cycle as a function of the cooling temperature for sample S_1……..98
5.3.2. Applied field effects……100
Note on the Squid magnetometer remanent field value……101

5.4. Discussions
5.4.1. Experimental exchange bias compared to usual models……..103
5.4.2. Phenomenological description of exchange bias……..105

References Chapter 5……..**112**

Chapter 6: Magnetic after effect measurements

6.1. Time dependent measurements in sample S_1 and S_2

6.1.1. Time dependent effects on the 1st branch of the hysteresis cycle in sample S_1…...113

6.1.2. Thermal activation on the 2nd and 3rd branches of the hysteresis cycle……...118

6.2. Analysis and discussion of time dependent effects

6.2.1. Thermal activation on the 1st branch of the hysteresis cycle……...123

6.2.2. Activation volume along the 2nd and 3rd branches of the cycle……...125

6.2.3. General remarks concerning the activation volume……126

6.2.4. Coercive field model along the 2nd and 3rd branches of the cycle ……..127

References Chapter 6…….....**129**

Conclusions……...**131**

References Conclusion……...**135**

List of Figures……**137**

List of symbols and abbreviations……....**143**

Introduction

Exchange bias (EB) occurs in magnetic bilayers (or multilayers) as a result of the interfacial exchange coupling existing at an interface between a ferromagnetic material and an antiferromagnetic one. This phenomenon was discovered more than 50 years ago by Meiklejohn and Bean [1] and it was initially termed exchange anisotropy. It manifests itself as a shift of the ferromagnetic hysteresis cycle along the field axis. This shift appears when the bilayer is cooled under field from above the Néel temperature of the antiferromagnet. Qualitatively, the shift of the cycle may be understood as resulting from the broken symmetry of the antiferromagnetic-ferromagnetic coupling at the interface. In addition to the loop shift, an increase in the ferromagnet coercivity is most generally observed.

The exchange bias phenomenon is exploited in GMR sensors, based on spin-valve structures, to pin the ferromagnetic magnetization of one of the two ferromagnetic layers involved. A resistivity change occurs which results from the rotation of the other ferromagnetic layer magnetization, the free layer, with respect to that of the pinned layer. The exploitation of exchange bias in GMR sensors represents the first industrial application of antiferromagnetism. These GMR sensors are primarily used in reading heads of hard disk drives. Current effort along the same line aims at the development of MRAM s in which the same concept of EB-pinned ferromagnetic layers is involved.

The interfacial exchange-coupling between the ferromagnetic and antiferromagnetic materials involved in exchange bias systems, may involve various energy terms, which are strongly competing. As a result, complex frustrated interfacial magnetic configurations may exist, which are further very difficult to characterise experimentally. This explains that, despite intense recent experimental and theoretical effort, exchange-bias is not quantitatively understood. Yet, when one examines which are the most studied EB systems (Co or FeNi as a ferromagnet and CoO, NiO, FeMn, PtMn or IrMn as an antiferromagnet), it appears that they are perhaps not always the most appropriate to progress in the understanding of exchange-bias. In particular, in all these systems, except CoO, the Néel temperature of the antiferromagnet is above room temperature. In the present thesis, I have studied the EB properties of Co/MnPd. MnPd is an antiferromagnet which orders at T_N=170K. It was thus possible to study the exchange-bias properties of this system from low temperature up to the MnPd Néel temperature.

In the **first Chapter** of this manuscript, I present a brief overview of the experimental studies of exchange-bias systems and associated theoretical studies of this phenomenon. In particular, I try to identify which are the most significant contributions to the analysis of exchange-bias, and I discuss the validity of the hypotheses which are at the basis of the various models developed to describe this phenomenon.

The study of magnetic-after effects in EB systems, constitute an originality of my work. In the **second Chapter** of the present manuscript, I present the well known Fatuzzo-Labrune [2] model, very often used to analyse magnetization processes in hard magnetic films. This model is valid under the conditions that a small number of energy barriers (only one barrier in principle) is involved in the nucleation of reversed magnetic domains and similarly only one another barrier for their propagation. This appeared not to apply to the MnPd/Co system under all conditions. Then, models which assume the existence of a broad distribution of barriers are more appropriate. This is the case of the models used to describe magnetic after effects in hard magnets, which are presented in the second part of this Chapter

The various experimental tools used in the course of this work are presented in **Chapter 3**. Essentially, these are sputtering for sample preparation, X-ray diffraction and reflectometry for structural characterisation, and VSM and SQUID for magnetic measurements.

The preparation of the various samples is described in **Chapter 4**, as well as the results of their structural characterisation.

Chapter 5 is devoted to the description of the magnetic measurements on the various MnPd/Co samples. The hysteresis cycles were measured systematically from low temperature to above T_N and the temperature dependence of the exchange-bias field, H_E, and coercive field, H_c, derived. The specific influence of the applied field on exchange-bias close to T_N is examined. In the second part of this Chapter, a model is proposed in which the ferromagnetic molecular field on the antiferromagnet is formally equivalent to an applied external magnetic field. The model presents similarities to the Koon's [3] or Schulthess and Butler [4] approaches of exchange-bias. However, the very strong canting which emerges for the first antiferromagnetic layer leads to unexpected behaviours.

Chapter 6 is devoted to the description of magnetic after effect measurements and to their discussion. The behaviours characterising the first hysteresis cycle are found to differ very substantially from the ones observed on the subsequent cycles. The various behaviours are analysed quantitatively permitting a consistent picture to emerge. Finally, the temperature dependence of the coercive field is briefly discussed.

The main results of this work are summarised in the **conclusion** and perspectives are presented.

Introduction

Exchange bias (EB) ou le décalage d'échange est observé lorsque l'on met en contact un matériau ferromagnétique (FM) avec un matériau antiferromagnétique (AF). Ce phénomène a été découvert il y a plus de 50 ans par Meiklejohn et Bean [1] et il a été initialement appelé « anisotropie magnétique d'échange ». Le phénomène trouve son origine dans le couplage interfacial d'échange et il se manifeste par un décalage en champ magnétique du cycle d'hystérésis. Ce comportement apparaît lorsque la bicouche FM/AF est refroidie sous champ au-dessus de la température Néel de l'antiferromagnétique. Qualitativement, le décalage du cycle est le résultant de la brisure de la symétrie du couplage antiferromagnétique - ferromagnétique à l'interface. De plus, une augmentation de la cœrcivité du matériau ferromagnétique est conjointement observée.

Le phénomène de décalage d'échange est exploité dans les capteurs à magnétorésistance géante (GMR), à base de structures vanne de spin. Toute rotation de la aimantation de la couche ferromagnétique libre par rapport à la couche de référence (bloquée) induit une modification de la résistance. La couche de référence est piégée par couplage d'échange avec une couche antiferromagnétique, c'est qui fait des capteurs GMR la première application industrielle de l'antiferromagnétisme. Une des applications la plus courante ce sont les têtes de lecture de disques durs.

Le couplage d'échange entre les matériaux ferromagnétiques et antiferromagnétique impliqués dans les systèmes à décalage d'échange, qui présentent différents types de ordre magnétiques, peuvent faire appel à différentes terme d'énergie, qui sont fortement concurrentes. Par conséquence, des configurations interfaciales magnétiques très frustrées peuvent exister, dont la caractérisation expérimentale s'avère très complexe voire impossible. Cela explique que, malgré les efforts théoriques et expérimentaux récents, le décalage d'échange demeure quantitativement mal compris. Pourtant, quand on regarde les systèmes EB les plus étudiées (Co ou FeNi comme matériau ferromagnétique et CoO, NiO, FeMn, PtMn ou IrMn comme un matériau antiferromagnétique), il apparaît que ce sont peut-être pas les matériaux les plus appropriés pour avancer dans la compréhension de ce phénomène. En particulier, dans tous ces systèmes, à l'exception du CoO, la température de Néel du matériau antiferromagnétique est au-dessus de la température ambiante. Cette thèse a eu pour but l'étude du phénomène de décalage d'échange dans le système Co/MnPd. La température critique du MnPd étant de $T_N = 170K$, une analyse sur une large plage de températures a été possible.

Le **premier chapitre** de ce manuscrit fait le point sur les études expérimentales menées sur les systèmes au décalage d'échange ainsi que sur les modèles théoriques associés. En particulier, je tente d'identifier qui sont les plus importantes contributions à l'analyse de décalage d'échange, et je discute la validité des hypothèses qui sont à la base des différents modèles développés pour décrire ce phénomène.

L'étude des effets traînage dans les systèmes EB, constitue une originalité de mon travail. Dans le **deuxième chapitre** de ce mémoire, je présente le modèle du Fatuzzo Labrune [2], très souvent utilisé pour décrire le renversement de l'aimantation dans les couches magnétiques dures. Ce modèle est valable lorsqu'on considère une seule barrière d'énergie dans la nucléation des domaines magnétiques et une seule barrière pour la propagation des parois. L'expérience montre que ce n'est pas le cas pour le système Co/MnPd, en générale, pour lequel, les modèles qui supposent l'existence d'une large distribution des barrières d'énergie semblaient plus adéquats.

C'est le cas des modèles utilisés pour décrire les effets magnétiques dans les aimants dur, qui sont présentés dans la deuxième partie de ce chapitre.

Les différents outils expérimentaux utilisés dans le cadre de ces travaux sont présentés dans le **chapitre 3**. Essentiellement, il s'agit de la technique de la pulvérisation cathodique pour la préparation des échantillons, de la diffraction de rayons X et de la réflectométrie pour la caractérisation structurale, et du SQUID et VSM pour les mesures magnétiques.

La préparation des différents échantillons est décrite dans le **chapitre 4**, ainsi que les résultats de leur caractérisation structurale.

Le **chapitre 5** est consacré à la description des mesures magnétiques sur les différents échantillons Co/MnPd. Les cycles d'hystérésis sont mesurés systématiquement à partir de basses températures au-dessus de T_N et la variation en fonction de la température du champ coercitif, Hc, et du champ bias H_E sont déduites. L'influence spécifique du champ appliquée sur le champ bias aux températures proche du T_N, est examinée. Dans la deuxième partie de ce chapitre, un modèle est proposé dans lequel le champ magnétique moléculaire sur la couche antiferromagnétique est modélisé comme un champ magnétique extérieur appliqué. Le modèle présente des similitudes avec les approches du Koon [3] ou Schulthess et Butler [4] Cependant, la très forte tilt qui apparaît pour la première couche antiferromagnétique conduit à des comportements inattendus.

Le **chapitre 6** résume les mesures de traînage et leur interprétation. Les valeurs du volume d'activation sur la premier partie du cycle d'hystérésis sont presque identique a celles déterminée sur les parties suivant du cycle. Enfin, la dépendance en température du champ coercitif est brièvement discutée.

Les principaux résultats de ce travail sont énumérés dans la **conclusion** générale suivis par les perspectives.

References-Introduction

[1] W.H.MEIKLEJOHN, C.P.BEAN, *New magnetic anisotropy* Phys. Rev. Vol.102, p5, (1956).

[2] M.LABRUNE, S.ANDRIEU, F.RIO, *Time dependence of magnetization process of RE-TM alloys, J. Magn. Magn. Mater*. vol.80, p211 (1989).

[3] N.C.KOON, *Calculations of Exchange Bias in Thin Films with Ferromagnetic / Antiferro-magnetic Interfaces*, Phys. Rev. Lett. vol.78, p4865 (1997).

[4] T.C.SCHULTHESS, W.H.BUTLER, *Consequences of Spin-Flop Coupling in Exchange Biased Films,* Phys. Rev. Lett. vol.81, p4516 (1998).

References-Introduction

Chapter 1

Exchange bias: systems and models

1.1. The exchange-bias phenomenon

Exchange bias, also called *exchange anisotropy,* is a phenomenon which characterises systems in which antiferromagnetic (AFM) and ferromagnetic (FM) materials are coupled. This phenomenon manifests itself by a shift of the center of the hysteresis loop from H=0. It was discovered in 1956 by Meiklejohn and Bean when studying Co particles embedded in their native ferromagnetic oxide (CoO) [1]. These authors observed that the M-H loops measured at T=77K were displaced along the field axis (see Figure 1.1) when the particles were cooled under field through the Néel temperature of CoO (T_N=291K). Since the discovery of this effect, extensive work has been carried out to study various kinds of exchange bias systems. However, the microscopic origin of this phenomenon is still poorly understood [2]. Its present application in spin-valve based sensors and other application for magnetic recording has triggered a renewed interest into this phenomenon.

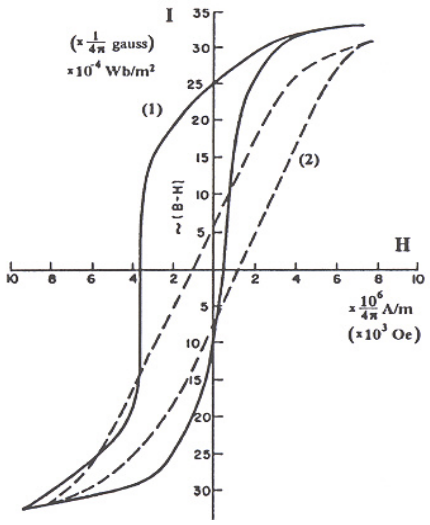

Figure 1.1*. Hysteresis loops at 77K of partially oxidized Co particles. Curve (1) shows the resulting loop cooling the compact in a 1T field. Curve (2) shows the loop when cooled in the absence of magnetic filed (zero field cooling-after [1]).*

A qualitative description of the exchange-bias phenomenon is presented in the following sections.

1.1.1. Qualitative description

Figure1.2. provides the Meiklejohn-Bean picture of exchange bias. When a field is applied in the temperature range $T_N < T < T_C$, (where T_C is the Curie temperature of the ferromagnetic layer) the FM spins line up with the field while the AFM spins remain random (see Figure 1.2 (i)).When cooling to $T < T_N$, in the presence of the field, due to the interaction at the interface, the AFM spins next to the FM align ferromagnetically to those of the FM layer. The other spin planes in the AFM "follow" the AFM order so as to produce zero net total magnetization(see Figure 1.2 (ii)).When the field is reversed, the FM spins start to rotate. However, the AFM spins remain unchanged (see Figure 1.2 (iii)). The interfacial interaction between the FM/AFM spins at the interface, tries to align ferromagnetically the FM spins at the interface, i.e. the AFM spins at the interface exert a macroscopic torque on the FM spins, to keep them in their original position (see Figure 1.2 (iii)).This is the origin of exchange bias.

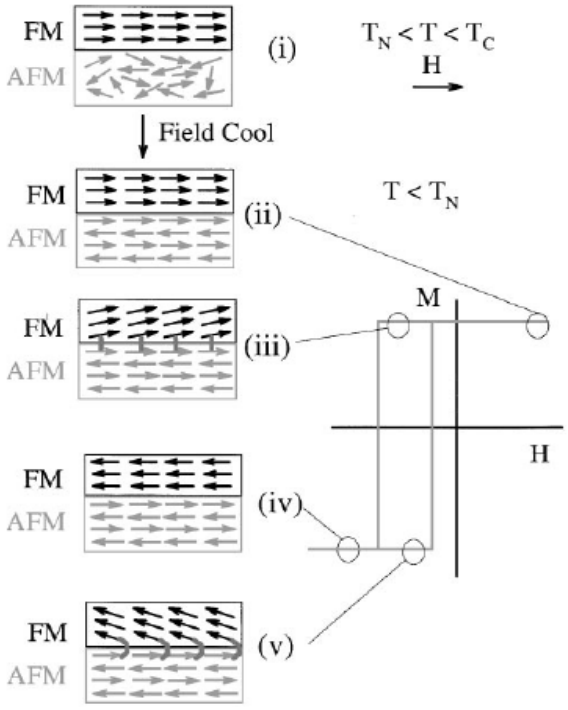

Figure 1.2. *Schematic diagram of the spin con-figuration of an FM/AFM bilayer at different stages (i) - (v) of an exchange- bias hysteresis loop (after [2]).*

This picture for EB provides a simple explanation for the phenomenon. However, it fails to predict the magnitude of exchange-bias field. The exchange-bias field, according to this model, is several orders of magnitude larger than the experimental one.

For example [8], in the system of FeMn / NiFe (NiFe = $Ni_{81}Fe_{19}$) it is plausible that the interfacial exchange interaction (J_{INT}) should be comparable to the effective exchange interactions of NiFe or FeMn, ($J_{FM} < J_{INT} < J_{AFM}$), namely, of order 10^{-14} SI. Applying Meiklejohn and Bean's model to FeMn/NiFe system with permalloy thickness of about 40nm, the exchange-bias field is predicted of about 0,5T. However, the observed exchange-bias field in the system is only 5mT.The factor of discrepancy needs to be explained.

1.2. Physical parameters governing exchange - bias

1.2.1. Exchange bias and coercive field

An interface coupling due to exchange anisotropy is observed when cooling the AFM/FM couple in the presence of a static magnetic field from temperature above T_N, below T_C ($T_N<T<T_C$) to a temperature $T<T_N$. After such a field cooling procedure the hysteresis loop of the AFM/FM system at $T<T_N$ is shifted along the field axis generally in the opposite direction to the cooling field direction ("*negative* "exchange bias). This loop shift defines the *exchange bias field*, H_E (see Figure 1.3).

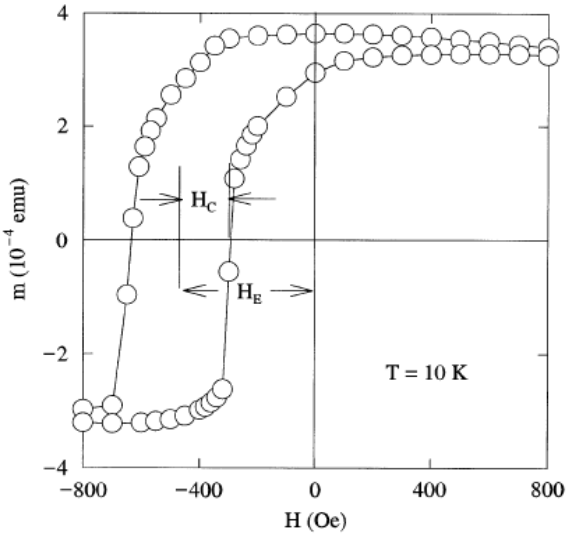

Figure 1.3. *Hysteresis loop, m(H), of a FeF_2/Fe bilayer at T=10K after field cooling . The exchange bias, H_E, and the coercivity, H_C, are indicated in Figure (after [2]).*

The *coercivity*, H_C, which is defined as the half width of the loop, increases generally as well after the cooling procedure. Both the loop shift and the increased coercivity disappear at, or close to, the AFM Néel temperature confirming that it is the presence of the AFM material, which causes these effects [1, 2]. The coercivity increase below T_B[1], tends to characterise low-anisotropy AFM systems [3].

It can be understood as follows: in the case of an AFM with small anisotropy, when the FM rotates it"drags" the AFM spins irreversibly, increasing the FM coercivity. For a large AFM anisotropy, the FM decouples from the AFM because it cannot drag the AFM spins, in this case the coercivity increase is much less [4, 5].

1.2.2. Field cooling (FC) and zero field cooling (ZFC)

As already mentioned to induce unidirectional anisotropy and thus exchange bias, the AFM/FM layer systems are usually cooled (or grown) below the AFM Néel temperature, in the presence of a static magnetic field, which allows the ferromagnetic layer to be saturated. Larger cooling fields do not further affect the FM layer. It is generally considered that the exchange bias field is zero after zero field cooling (ZFC).

However, Miltényi et Gierlings [7] have shown that exchange bias field H_E, can be tuned by cooling in zero field from different magnetization states (see Figure 1.4.), in agreement with several other studies [6], this confirms that the role of cooling field is not to induce H_E but only to have a single FM domain state above T_N and thus a maximum exchange bias effect.

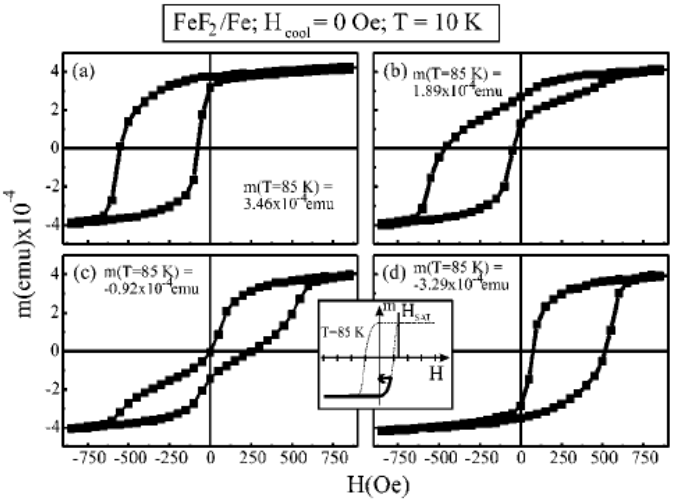

Figure 1.4. *Hysteresis loops for a FeF_2/Fe bilayer at T=10K cooled in zero field from T= 85K in different magnetization states (a) m = 3.46×10^{-4} emu, (b) m = 1.89×10^{-4} emu, (c) m = -0, 92 ×10^{-4} emu, (d) m= -3.29 ×10^{-4} emu (after [7]).*

[1] Blocking temperature of the system starting from which the exchange bias field vanishes.

It allows to select the desired value of exchange-bias using a simple postgrowth cooling procedure. The study was done on FeF_2/Fe and CoO/Co systems both of which allow for easy cooling and warming of the sample across the AFM Néel temperature, $T_N(FeF_2)$=78K and T_N(CoO)=291K.

1.2.3. Thickness dependence

FM thickness

Generally the exchange bias field is roughly inversely proportional to the thickness of the FM layers indicating that exchange bias is an interface effect.

$$H_E \propto \frac{1}{t_{FM}} \tag{1.1}$$

This relation holds for rather thick and continuous FM layers. However, if the FM layer is very thin, the relation is no longer valid which can be attributed to the fact that the FM layer becomes discontinuous. The dependence of coercive field on FM thickness is, more complex and may be strongly sample dependent [2, 8].

AFM thickness

In general, for thick AFM layers, typically over 20 nm, H_E does not depend on the thickness of the AFM layer .This is expected considering that exchange bias is an interface phenomenon and that, to approximation, the AFM magnetization does not couple to the applied field. However as the AFM thickness is reduced, H_E decreases abruptly and finally, for thin enough AFM layers (usually a few nm) H_E becomes zero, as shown in Figure 1.5. and Figure 1.6.

This decrease of H_E can be attributed to various phenomena. At very low thickness, the AFM structure can be affected. Also, it should be remembered that the total AFM anisotropy is involved in exchange bias as illustrated by the Meiklejohn-Bean condition for exchange bias:

$$K_{AFM}\, t_{AFM} \geq J_{INT}$$

where K_{AFM} is the anisotropy of the AFM layer, t_{AFM} the thickness of the AFM layer and J_{INT} the interface coupling constant.

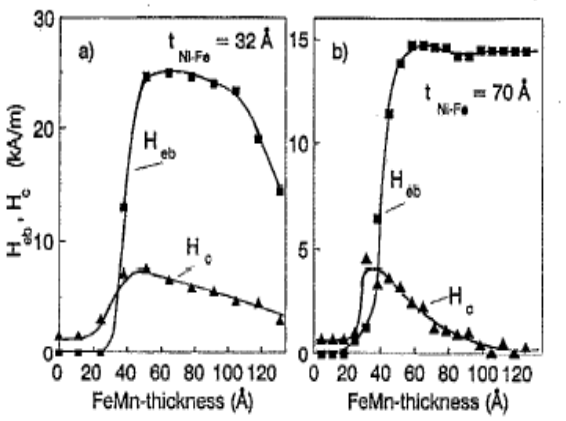

Figure 1.5. *Dependence of exchange bias H_E (square symbols) and coercivity H_C (triangular symbols) for the [111] oriented sample for 32 and 70Å $Ni_{80}Fe_{20}$ systems (after [8]).*

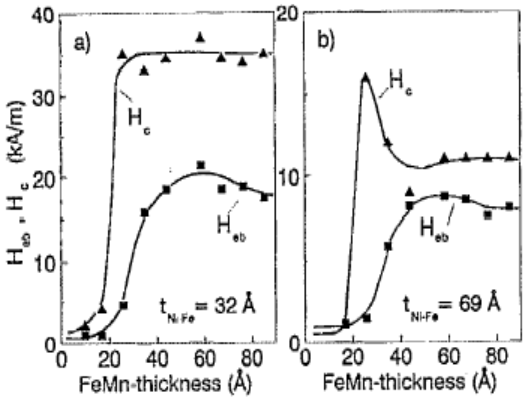

Figure 1.6. *Dependence of exchange bias H_E (square symbols) and coercivity H_C (triangular symbols) for the [011] oriented sample for 32 and 70Å $Ni_{80}Fe_{20}$ systems (after [8]).*

1.2.4. Temperature dependence and blocking temperature

Generally, the exchange bias field decreases as the temperature increases. The blocking temperature (T_B) is defined as the temperature at which the exchange bias vanishes. As already mentioned in very thin AFM films, T_B is in general close to T_N [9] (see Figure 1.7.). There are however systems in which T_B is much lower then T_N. This phenomenon seems to be related to the grain size and thickness of the AFM layer, through finite size effects.

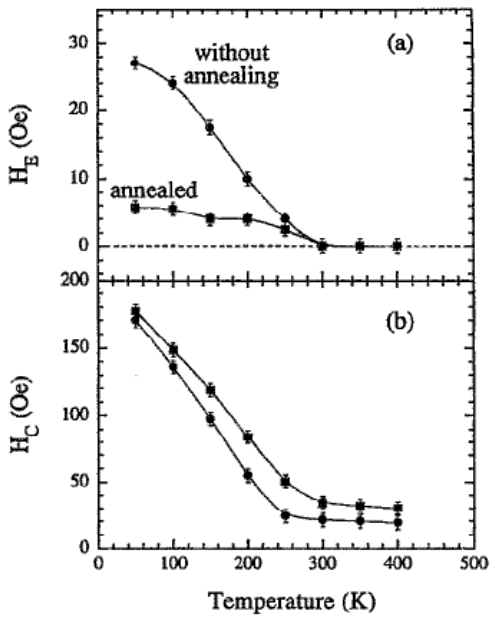

Figure 1.7. *Exchange-bias field H_E and coercive field H_C versus measurement temperature for two permalloy (200Å)/CoO samples: (square symbols) annealed at 1100°C for 36h prior to deposition, (circular symbols), without annealing (after [9]).*

1.2.5. Negative and positive exchange bias

The shift of the hysteresis loop is usually in the reversed direction of the cooling field, denoted as negative exchange bias or normal exchange bias. Positive exchange bias (PEB), i.e. a shift in the same direction of the cooling field, was first observed by Noguès *et al.* [11] in FeF_2/Fe bilayers cooled in a very high field(H_{FC}=7T) whereas negative exchange bias was observed when cooled in lower field (H_{FC}=0,2T).

PEB may constitute an important clue to understand the mechanism that governs EB in general. The value of the cooling field needed to obtain a positive shift of the hysteresis cycle is an important parameter influenced by the structure of the sample, and the interfacial coupling. In the case of a strong interfacial coupling a larger cooling field is necessary to obtain a positive shift [12].

To explain PEB, Kiwi *et al.* [13] have proposed that, at high cooling fields, the interface layer of the antiferromagnet aligns ferromagnetically with the external applied field and therefore ferromagnetically with the F itself. As the preferred orientation between the interface spins of the F layer and AFM layer is the antiparallel one (antiferromagnetic coupling), the EB becomes positive.

1.2.6. Asymmetry of the hysteresis loops-training effect

A curious characteristic of the exchange bias observed in several systems is the fact that the two branches of the hysteresis loop are different: the descending part is steeper and the ascending one is more rounded. Such an asymmetry is observed in exchange biased bilayers with thin antiferromagnetic layers or for systems containing low anisotropy antiferromagnets [14] (see Figure 1.8.).

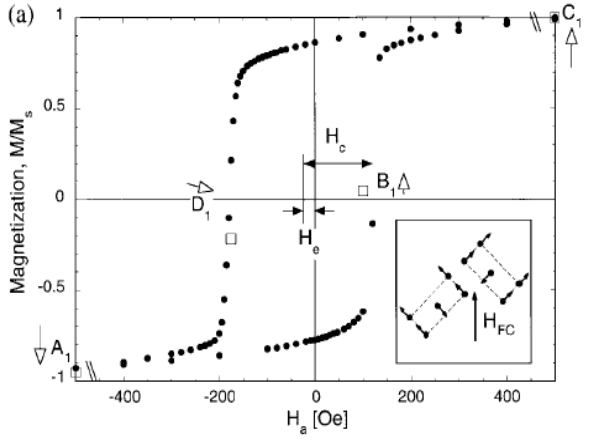

Figure 1.8. *Hysteresis loop for the Fe-MnF_2 sample and the orientation of the cooling field, H_{FC}=0.64T, relative to the MnF_2 domains (after [14]).*

This phenomenon is due to the fact that AFM moment configuration is not fully frozen and tends to follow the FM moments at the interface. After FM moments reversal, a torque exists in the AFM moments which favour progressive moment rotation at the expense of nucleation / propagation observed during the first half cycle [15, 16] (see Figure 1.9).

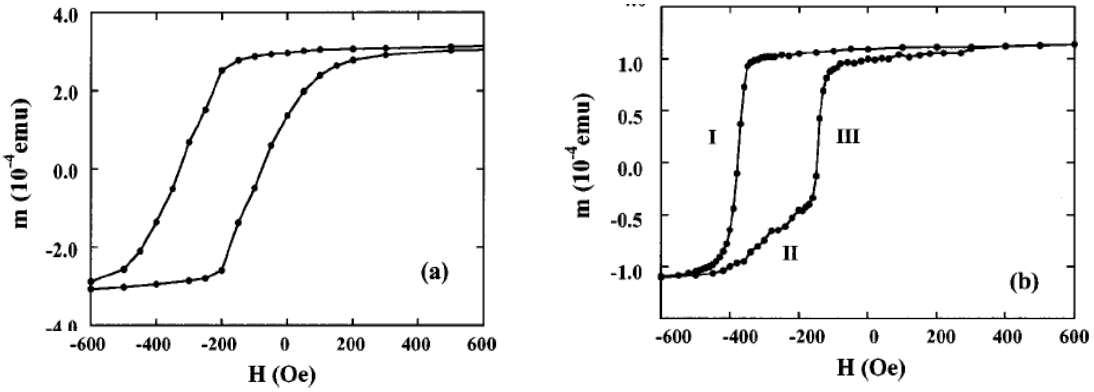

Figure 1.9. *Magnetic hysteresis loops of (a) a uniform FeF_2(200 Å)/Fe(150 Å)/Al(40 Å) film, and (b) a uniform FeF_2(200 Å)/networked-Fe(150 Å)Al(40 Å) at 10 K, after field cooling in 0.5T from 300 K. Different parts of the reversal process are labelled I, II, and III (after[15]).*

Further in many exchange-biased film systems, H_E depends on the number of measurements, a property often called a *training effect* [17, 18, 19, 20]. If several consecutive hysteresis loops are measured, the shift (H_E) of the consecutive loops will decrease. It was often found experimentally that $H_E - H_{E\infty} \propto 1/\sqrt{n}$, where n indicated the total number of consecutive loops (see Figure 1.10).

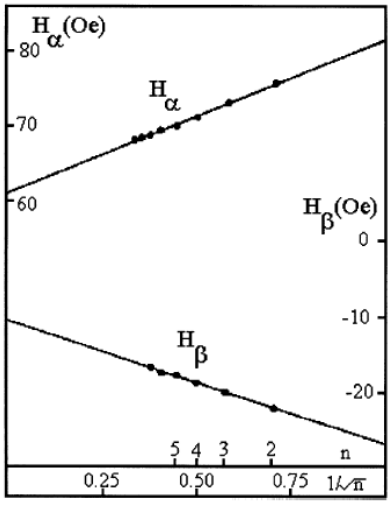

Figure 1.10*. Coercive fields for the increasing field branch, H_α, and decreasing field branch, H_β, of the hysteresis loop as a function of measurement order, n, for an Fe20Ni80/ FeNiMn bilayer at room temperature(after [20]).*

This phenomenon, often more important in polycrystalline AFM seems to be related to partial reorientation of the AFM domains due to FM magnetization reversal [21].

1.3. Exchange bias systems

After the discovery by Meiklejohn and Bean [1] in 1957, of exchange bias in Co/CoO small particles, exchange bias has been observed in a great number of materials. Initially most studies concerned exchange bias with oxide systems (Co or NiO) coupled to a simple ferromagnet such as Fe, Co FeNi .More recently most studies focused on exchange bias in films and in many instances the AFM was a metallic alloy in particular with Mn.

A brief summary of the different systems studied is presented in Table1, together with their essential magnetic properties [2].

It is unfortunate that the exchange bias parameters shown in this table are not always meaningful since they correspond to room temperature (where $\Delta\sigma$ represents the variation in interfacial exchange coupling energy which occurs when the FM layer magnetization is reversed and will be discussed more in detail in Chapter 5 section 5.4).

AFM material	$\Delta\sigma(10^{-3} * J/m^2)$	$T_B(K)$	$T_N(K)$
CoO	0.4	183	290
NiO	0.09	480	520
$Ir_{20}Mn_{80}$	0.19	520	690
$Pt_{56}Mn_{44}$	0.032	650	980
$Ni_{50}Mn_{50}$	0.27	520	1070
$Fe_{46}Mn_{54}$	0.09	330	490

Table1. *Calculated parameters associated to different metallic AFM's.*

1.4. Models and theories

Since the discovery of exchange-bias, many models have been introduced to explain the properties of this effect. Up to now, there is no model that can give a full explanation to this phenomenon.

1.4.1. Meiklejohn and Bean's model

In their paper, Meiklejohn and Bean proposed for the first time a model to explain the exchange-bias and its related effect. They assumed coherent rotation of the FM and AFM magnetization. The energy per unit interface can be written [1] as:

$$E = -\mu_0 H_{app} M_{FM} t_{FM} \cos(\theta - \beta) + K_{FM} t_{FM} \sin^2(\beta) + K_{AFM} t_{AFM} \sin^2(\alpha) - J_{INT} \cos(\beta - \alpha) \qquad (1.2)$$

where H_{app} is the applied magnetic field, M_{FM} the spontaneous magnetization of the ferromagnetic layer, t_{FM} the thickness of the FM layer, t_{AFM} the thickness of the AFM layer, K_{FM} the anisotropy of the FM layer (in J/m^3), K_{AFM} the anisotropy of the AFM layer (in J/m^3) and J_{INT} the interface coupling constant (in J/m^2), equal to $\Delta\sigma/2$.

The angles are defined as follows: α is the angle between M_{AFM} and the AFM anisotropy axis, β is the angle between M_{FM} and the FM anisotropy axis and θ is the angle between H and the FM anisotropy axis (see Figure 1.11.).

Neglecting the FM anisotropy, which in general is considerably smaller than K_{AFM} and minimizing the energy with respect to α and β, the exchange bias field is given by:

$$\mu_0 H_E = \frac{J_{INT}}{M_{FM}\, t_{FM}} \tag{1.3}$$

Another important result from this minimization is the condition:

$$t_{AFM}\, K_{AFM} \geq J_{INT} \tag{1.4}$$

which is required for the observation of exchange-bias.

When $K_{AFM}t_{AFM} >> J_{INT}$, the AFM magnetization remains frozen (α is a constant) when the FM magnetization rotates (β vanishes).By contrast for $K_{AFM}t_{AFM} << J_{INT}$, the FM moments drag with them the AFM moments during their reversal.

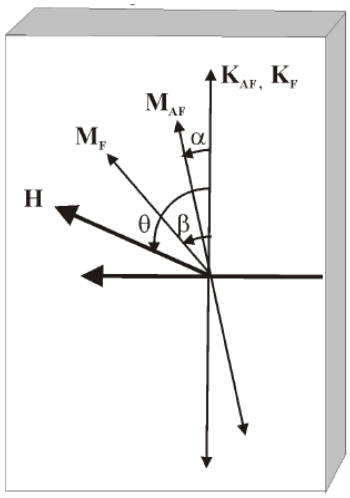

Figure 1.11. *Schematic diagram of angels involved in an exchange-bias system. The AFM and the FM anisotropy axes are assumed to be collinear (after [2]).*

1.4.2. Interfacial domain wall

In the following section, the main physical parameters governing exchange bias are described (section.1.2) and the various models performed to approach more qualitatively this phenomenon are presented (1.3).

1.4.2.1. Néel-Mauri's model

In order to account for the discrepancy of the Meiklejohn and Bean model with experiment, Néel in 1967 [22] and Mauri et *al.* [23] in 1987 proposed an explanation for the reduced bias fields by showing that the formation of a domain wall parallel to the interface dramatically lowers the energy required to reversed the magnetization. The Mauri model is illustrated in Figure 1.12. The infinitely thick AFM is assumed to have a uniaxial anisotropy in the z direction. To simplify the Figure, spins of only one sublattice are shown.

The FM spins rotate coherently, when the applied magnetic field is swept as to measure the hysteresis loop. The first interfacial AFM monolayer is oriented away from the FM spins making an angle α with the direction of the field cooling direction and with the anisotropy axis of the AFM layer. The next AFM monolayers are oriented away from the interfacial AFM spins as to form a domain wall parallel to the interface.

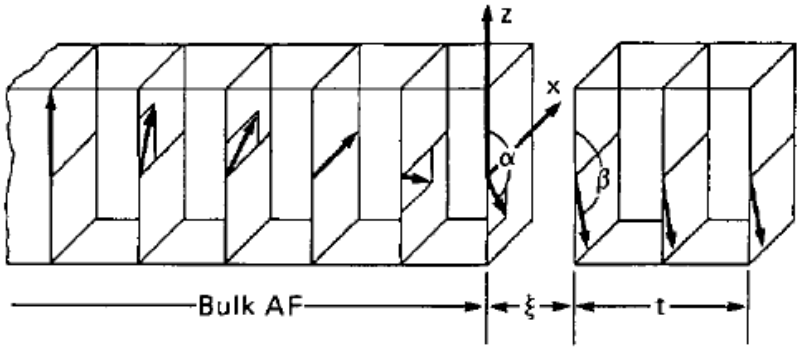

Figure 1.12. *Magnetic model for the interface of a thin ferromagnetic film on a thick antiferromagnetic substrate. The uniaxial anisotropy of the antiferromagnet is along the z axis. External magnetic field is applied opposite to z and the exchange coupling across the interface with thickness ξ is positive. The spins of only one sublattice of the antiferromagnet are shown (after Mauri et al. [23]).*

The spins of only one AFM sublattice are depicted, the spins of the other sublattice being oppositely oriented as to complete the AFM order.

Using the Stoner-Wohlfarth model, the energy can be written as:

$$E = -\mu_0 H_{app} M_{FM} t_{FM} \cos(\theta - \beta) + K_{FM} t_{FM} \sin^2(\beta) - J_{INT} \cos(\beta - \alpha) - 2\sqrt{A_{AFM} K_{AFM}}\,(1 - \cos(\alpha)) \tag{1.5}$$

where the first term is the Zeeman energy of the ferromagnet in an applied magnetic field, the second term is the anisotropy term of the FM layer, the third term is the interfacial exchange energy and, the forth term is the energy of the partial domain wall. The new parameter in the equation above is the exchange stiffness A_{AFM}. As in the case of Meiklejohn and Bean model, the interfacial exchange coupling parameter J_{INT} [J/m^2] is again left undefined.

The free energy can be written in units of $2\sqrt{A_{AFM} K_{AFM}}$, which is the energy per unit surface of a 90° domain wall in the AF layer:

$$e = k(1 - \cos(\beta)) + \mu \cos(\beta^2) + \lambda\left[1 - \cos(\alpha - \beta)\right] + (1 - \cos(\alpha)) \tag{1.6}$$

where: $\lambda = J_{INT} / (2\sqrt{A_{AFM} K_{AFM}})$, is the interface exchange, with J_{INT} being redefined as $J_{INT} = A_{FM-AFM} / \xi$, where ξ is the interface thickness. $\mu = K_{FM} t_{FM} / 2\sqrt{A_{AFM} K_{AFM}}$ is the reduced ferromagnet anisotropy, and $k = \mu_0 H_E M_{FM} t_{FM} / 2\sqrt{A_{AFM} K_{AFM}}$ is the reduced external magnetic field.

Mauri et al. [23] have calculated the magnetization curves by numerical minimization of the reduced free energy equation (1.6). Several values of the λ and μ parameters were considered providing quite realistic hysteresis loops. Their analysis highlighted two limiting cases, which delivers the following expressions for the exchange bias field:

$$\mu_0 H_E = -[(A_{FM-AFM} / \xi) / \mu_0 M_{FM} t_{FM}] \qquad \text{for } \lambda << 1 \tag{1.7}$$

$$\mu_0 H_E = -2(A_{AFM} K_{AFM})^{1/2} / t_{FM} M_{FM} \qquad \text{for } \lambda >> 1 \tag{1.8}$$

For the limiting case $\lambda << 1$ (strong coupling) the value of exchange bias field is similar to the value given by the Meiklejohn and Bean model. For this situation, practically no important differences between the predictions of the two models exist. When the coupling is weak $\lambda >> 1$, the Mauri model delivers a reduced exchange bias field which, practically is independent of the interfacial exchange energy. It depends on the domain wall energy and the parameters of the ferromagnet. The "$1/t_{FM}$" law is preserved by the Mauri model.

1.4.3. Frustration

1.4.3.1. Malozemoff's model

Malozemoff noted that the Néel –Mauri type of models were unlikely to provide a realistic description of EB systems because atomistically perfect uncompensated interfaces are assumed. Based on this idea Malozemoff (1987) proposed a new mechanism for exchange anisotropy postulating a random nature of the exchange interactions at the FM-AFM interface [24, 25]. Malozemoff noted that the exchange field created by a saturated ferromagnet on an antiferromagnet is equivalent to a random field. He argued than that, starting from an initially compensated interface, the antiferromagnet will spontaneously break up into magnetic domains of typical size δ, the AFM domain width (see Figure 1.13).

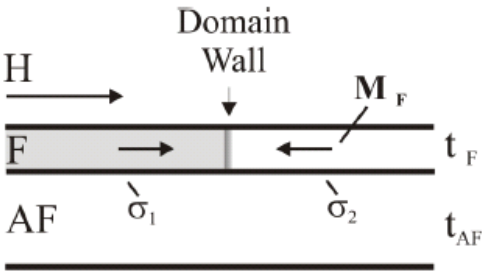

Figure 1.13. *Schematic side view of FM/AFM bilayer with FM domain wall driven by an applied field (after [24]).*

Assuming that the number of defects is equal to N, the interfacial energy becomes: $\sigma = \sigma_l / \sqrt{N}$ where $\sigma_l = \pm z \frac{J}{a^2}$ represents the interfacial energy per defect, a is the lattice parameter and z a parameter of the unity order.

When the antiferromagnet breaks up into domains, domain walls perpendicular to the interface are formed (see Figure 1.14).The exchange bias field is given by the competition between the interface energy gained when the domains are formed and the domain wall energy lost. One obtains:

$$\mu_0 H_E = \frac{\Delta\sigma}{2 M_{FM} t_{FM}} \tag{1.9}$$

where M_{FM} and t_{FM} are the magnetization and thickness of the ferromagnet.

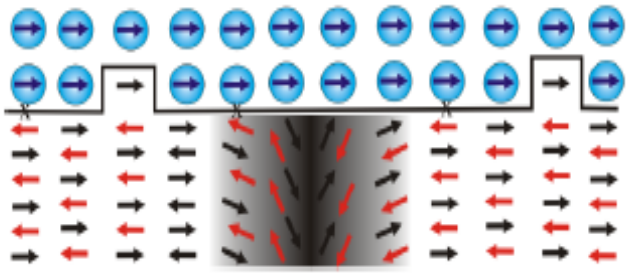

Figure 1.14. *Schematic view of a vertical domain wall in the AFM layer. It appears as an energetic favourable state of FM/AFM system with rough interfaces.*

By analyzing the stability of the magnetic domains in the presence of the random field, a characteristic length L of the frozen-in AFM domains and their characteristic height, h, are obtained: $L \approx \pi\sqrt{A_{AFM} / K_{FM}}$ and h = L/2, where A_{AFM} is the exchange stiffness constant and h is the characteristic height of the created AFM domains.

Once these domains are fixed, flipping the ferromagnetic orientation causes an energy change per unit area of $\Delta\sigma = 4zJ / \pi aL$, which further leads to the following expression for the EB field:

$$\mu_0 H_E = \frac{2z\sqrt{A_{AFM} K_{AFM}}}{\pi^2 M_{FM} t_{FM}} \tag{1.10}$$

This form is remarkably similar to equation (1.8) and therefore equally able to explain the order of magnitude of the exchange anisotropy effect, unfortunately the model is specifically formulated for single AFM systems and does not clearly propose how the model can be extended to polycrystalline systems.

1.4.4. Perpendicular coupling

1.4.4.1. Koon's model

In the system NiFe / FeMn, Jungblut *et al*. [8, 26] made the very surprising observation that the ferromagnetic moments were perpendicular to the antiferromagnetic ones.

Koon [27] tackled the problem of explaining EB in thin films with compensated FM/AFM interfaces by means of a micromagnetic calculation. His calculations indicate the stability of interfacial exchange coupling with a perpendicular orientation between the FM and AFM axes directions. He refers to the perpendicular interfacial coupling as "spin-flop" coupling (see Figure 1.15). To observe perpendicular interfacial coupling, his model specifies the structure and orientation of the AFM layer, and the relative orientation between the AFM and FM layer. The model utilizes a single-crystal body centered tetragonal (bct) AFM structure which gives place to have a fully uncompensated interfacial spin plane (1 0 0) or a fully compensated interfacial spin plane (1 1 0).

He included uniaxial anisotropy in the AFM crystal along the (0 0 1) axis, and the FM layer was modeled with no intrinsic anisotropy. The model was applied to two different cases of the AFM interfacial spin plane: (1) a fully compensated interface and (2) a fully uncompensated interface.

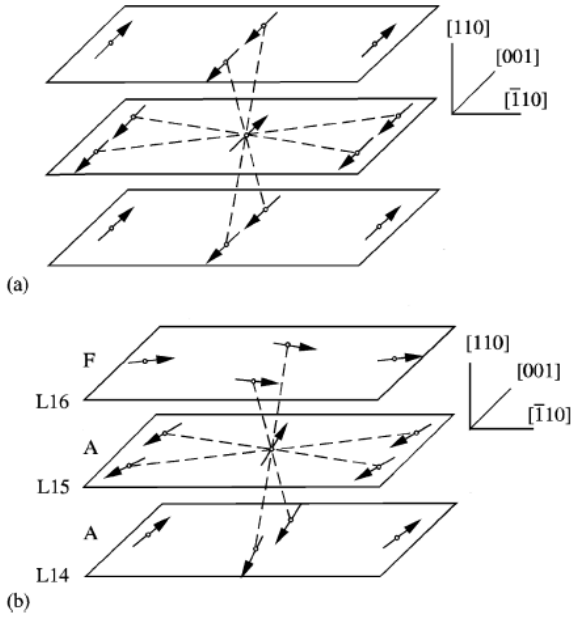

Figure 1.15. *(a) Magnetic structure of a <1 1 0 > oriented AFM body centered tetragonal crystal. The exchange bonds are represented by the dashed lines. (b) Lowest energy spin configuration near the interface plane. The interfacial AFM plane (L15) is fully compensated, and the interfacial FM plane (F16) is oriented perpendicular (90° coupling) (after [27]).*

For both cases, he calculated the interfacial energy density as a function of the angle between the FM spins and the Néel axis of the AFM spins. The fully uncompensated interface gives a collinear coupling, and a minimum at θ=0°. The fully compensated interface gives the surprising result of an energy minimum at θ=90° indicating perpendicular interfacial coupling between the FM and AFM spins (see Figure 1.16).

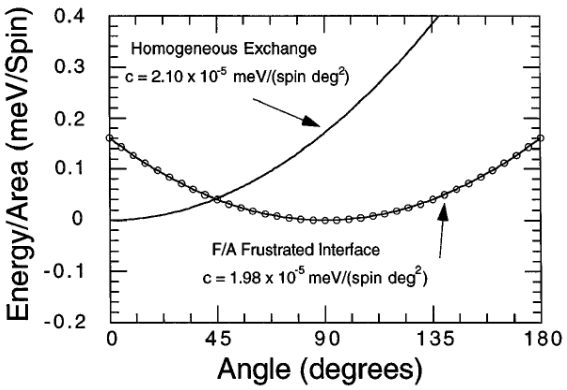

Figure 1.16. *Energy per unit area of a 15/15ML (110) FM/AFM bilayer as a function of the angle between FM and AFM magnetization axes. The dotted curve corresponds to a structurally identical film with only AFM or FM spins. For both films |J|=1meV (after [27]).*

Apart from similar success obtained by the preceding models, the model proposed by Koon can explain the exchange bias observed in compensated interface while the others can only explain that in uncompensated interface. This model is very consistent with experimental results from Nogués et al. [28].

Schulthess and Butler [29] combined Malozemoff's random interface field model, where surface defects are introduced assuming a interfacial unit cell with on interfacial FM site occupied by an AFM moment, with Koon's orthogonal magnetic arrangement model. According to this authors Koon's model fails to yield exchange bias H_E=0, but leads to coercivity. In the case of flat interfaces the FM/AFM coupling that results does not yield unidirectional anisotropy which is the source of bias but irreversible magnetization curves with finite coercivity is obtained.

1.4.4.2. Kiwi's model

Kiwi et *al.* [30, 31] proposed an extension of Koon's model to give an explanation for the dependence of the sign of the exchange bias on the cooling field magnitude.

This model is based on an incomplete domain wall in the FM and it assumes that the AFM interface monolayer reconstructs, close to Néel temperature, into an almost rigid canted magnetic structure. Moreover, it remains frozen, in a metastable state, during the cycling of the external magnetic field, when perform for $H<H_{FC}$. The model is specified analytically by the following Hamiltonian:

$$\mathcal{H} = \mathcal{H}_{AFM} + \mathcal{H}_{FM/AFM} + \mathcal{H}_{FM} \tag{1.11}$$

where: $\mathcal{H}_{AFM}$, $\mathcal{H}_{FM/AFM}$ and $\mathcal{H}_{FM}$ describe the AFM substrate, interface coupling and the FM slab, respectively.

The interface spin configuration of the bilayer after field cooling through T_N is illustrated in Figure 1.17. The left panel of Figure 1.17 corresponds to cooling under low H_{FC} field such that the interfacial exchange energy is larger than the Zeeman energy; on the contrary.

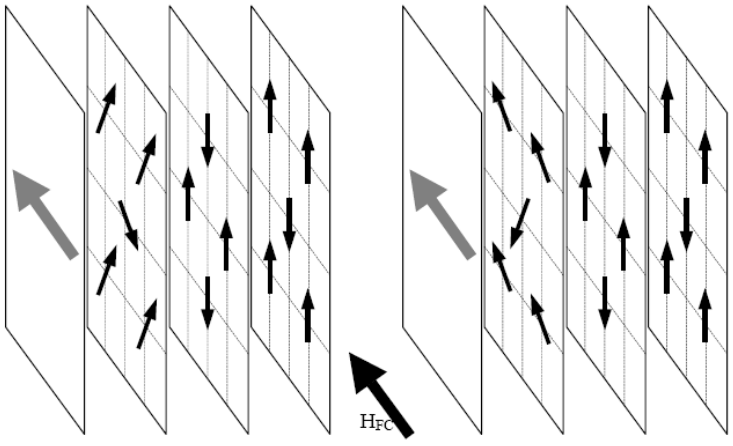

Figure 1.17. *Spin configuration of the AFM interface monolayer and both the FM and the two AFM monolayers closest to the interface, after it is field-cooled through T_N. The left panel is in case of low cooling field and the corresponded canting angle is larger than 90°. The right panel is for high cooling field and the canting angle is smaller than 90° (after Kiwi et al. [30]).*

By contrast, the right result panel corresponds to cooling under high magnetic field. In both cases the FM slab magnetization is fully saturated and the AFM spins are fixed, except those at the interface monolayer. Therefore, the only energy difference is due to changes of interface configuration. From the above equation, it is obtained:

$$E = 2\left|J_{AFM}\right|\left[\cos(2\theta)+\cos(\theta+\frac{\pi}{2})\right]-K_{AFM}\cos^2(\theta-\frac{\pi}{2})+(2\left|J_{FM/AFM}\right|-\mu_B g\ H_{FC})\cos\theta \quad (1.12)$$

where E is the energy per spin (the constant terms have been neglected), J_{AFM} and K_{AFM} the exchange and anisotropy parameters for the antiferromagnetic layer, μ_B the Bohr magneton, g the gyromagnetic ration and J_{FM}/J_{AFM} the interfacial exchange between the FM layer and the AFM layer.

$$\frac{\partial E}{\partial\theta}=(K_{AFM}-4\left|J_{AFM}\right|\sin 2\theta-2\left|J_{AFM}\right|\cos\theta-(2\left|J_{FM/AFM}\right|-\mu_B g\ H_{FC})\sin\theta=0 \quad (1.13)$$

Solving the above equation with respect to θ, the dependence of the sign of exchange bias (positive or negative) on the cooling field magnitude can be explained qualitatively. For low cooling fields ($H_{FC}<2|J_{FM/AFM}|/\mu_B g$), the energy is minimum for $\theta=\theta_c>\pi/2$, where θ_c is the canting angle of the AFM interface monolayer measured relative to H_{FC} (see the left panel of Figure 1.17.). Taking the projection of the AFM spin vectors on the field cooling direction, it can be deduced that the exchange bias is in the reversed direction of the cooling field.

Therefore this configuration accounts for negative exchange bias. Reciprocally, in the case of high cooling field ($H_{FC}>2|J_{FM/AFM}|/\mu_B g$), the minimum of E shifts to $\theta=\theta_c<\pi/2$, thus leading to positive exchange bias. If $H_{FC}=2|J_{FM/AFM}|/\mu_B g$ then the energy is minimum for $\theta=\theta_c=\pi/2$, and the exchange bias vanishes.

1.4.5. Compensated versus non compensated interfaces

1.4.5.1. Stamps approach

The approach developed by Stamps and co-workers [32, 33, 34] follows from the work of Néel and Mauri et *al.* [22, 23] extending the model of planar domain wall to the formation of partial domain wall in the AFM layer. Biquadratic (spin-flop) and bilinear coupling energies are considered. The model applies to compensated, partially compensated, and uncompensated interfaces.

In this model defects are simulated by mixing both ferromagnetic and antiferromagnetic spins at the interface. This is shown in the cross-sectional diagram of Figure 1.18. A single site defect in Figure s 1.18 (a) and 1.18 (b) is referred to as a line defect. Results for a step defect where two or more defects are introduced are shown in Figure s. 1.18 (c) and 1.18(d).

Introducing a line defect in a compensated surface this creates an asymmetry between the number of ‘‘up’’ and ‘‘down’’ spins at the interface. The impact of this asymmetry was studied by plotting the ‘‘natural’’ angle of the ferromagnet θ_{nat} measured relative to the antiferromagnet anisotropy axis, for different sizes of the unit cell in the [001] direction .This size is denoted by Λ. The angle θ_{nat} was determined by calculating the equilibrium orientation of the ferromagnet spins from an initial randomized state, in the absence of an applied field. Large exchange energy in the ferromagnetic layer is present so that all ferromagnet spins are aligned parallel.

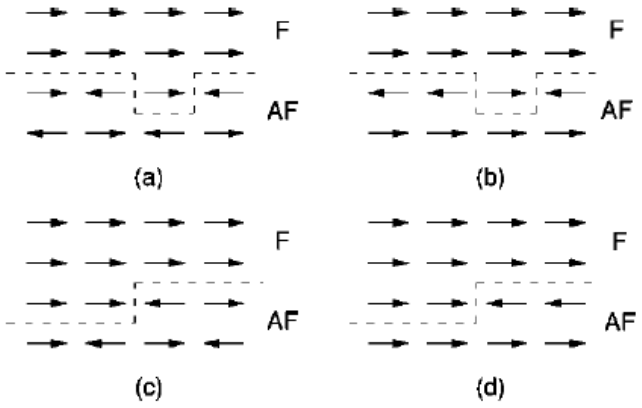

Figure 1.18. *Schematic diagram showing line defects [(a) and (b)] and step defects [(c) and (d)] at compensated and uncompensated interfaces [32, 33].*

The largest asymmetry was found for $\Lambda=2$ where only one antiferromagnet sublattice spin is present at the interface. This is uncompensated like in behaviour and results in $\theta_{nat} = 50°$. In the limit of a perfect interface $\Lambda\rightarrow\infty$, the ratio of the antiferromagnet sublattice interfacial spins become nearly equal and results in the tendency $\theta_{nat}\rightarrow 90°$. For the uncompensated case, an opposite trend is observed with a compensated like interface at $\Lambda= 2$ ($\theta_{nat} = 90°$) and $\theta_{nat} = 0°$ as $\Lambda\rightarrow\infty$.

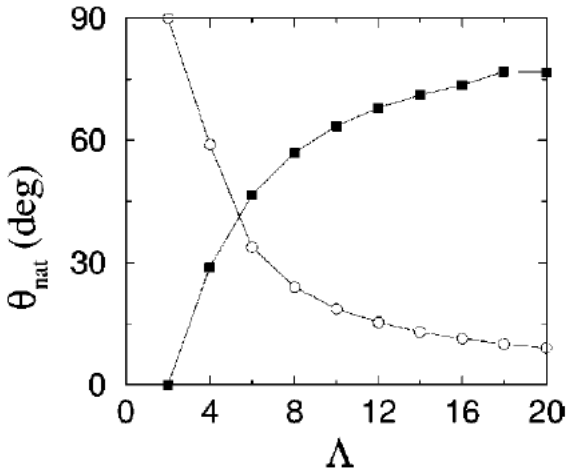

Figure 1.19. *The natural angle θ_{nat} as a function of defect spacing for compensated and uncompensated interfaces [33].*

The natural angle defines an axis along which a magnetization curve measurement attains the largest value of H_E, since this is the equilibrium orientation of the ferromagnetic layer.

The values of these angles for the perfect uncompensated interfaces are 90° and 0°, respectively (at 0° K, θ_{nat} is strongly temperature dependent) (as shown in Figure 1.19).

1.4.6. Final remarks

Although the phenomenon of exchange bias was discovered a long time ago, the physical origin of this effect remains poorly understood. Kiwi [31] has proposed a useful summary of the main features of the various models described in this section. The main conclusion are gathered in the table below:

Model	Main features	Interface magnetic structure	Main results
Meiklejohn's model	Coherent FM and AFM magnetization	Uncompensated AFM interface layer; collinear coupling between FM and AFM	H_E much larger than observed experimentally
Néel-Mauri's model	FM interface coupling; thin FM film	Uncompensated AFM interface layer; collinear coupling between FM and AFM	Reasonable H_E values
Malozemoff's model	Random defects create random fields	Uncompensated AFM interface layer; collinear coupling between FM and AFM	Reasonable H_E values; depend on structure
Koon/Schulthess model	Canting of the AFM interface spins	Compensated AFM interface layer; perpendicular coupling between FM and AFM	Realistic coupling mechanism
Kiwi's model	Spin glass like AFM canted interface layer	Compensated AFM interface layer; perpendicular coupling between FM and AFM	Reasonable H_E as a function of H_{FC}

Table2. *Brief outline of the main characteristics and results of the mentioned above models (adapted from Kiwi [31]).*

References-Chapter 1

[1] W.H.MEIKLEJOHN, C.P.BEAN, *New magnetic anisotropy* Phys. Rev. vol.102, p5, (1956).

[2] J.NOGUES, I.K.SCHULLER, *Exchange bias*, J. Magn. Magn. Mater. vol.192, p 203, (1999).

[3] M.J.CAREY, A.E.BERKOWITZ, *Exchange anisotropy in coupled films of $Ni_{81}Fe_{19}$ with NiO and $Co_xNi_{1-x}O$*, Appl. Phys. Lett. vol.60, p 3060, (1992).

[4] F.B.HAGEDORN, *Exchange anisotropy in oxidized permalloy thin films at low temperature,* J. Appl .Phys. vol.38, p 3641, (167).

[5] M.TSUNADO, Y.TSUCHIYA, M.KONOTO, M.TAKAHASHI, *Microstructure of antiferromagnetic layer affecting on magnetic exchange coupling in trilayered Ni-Fe/25 at% Ni-Mn / Ni-Fe films,* J. Magn. Magn. Mater. vol.171, p29, (1997).

[6] T.AMBROSE, C.L.CHIEN, *Dependence of exchange coupling on antifferomagnetic layer thickness in NiFe/Co bilayers* ,J. Appl. Phys. vol.83, p6822, (1998).

[7] P.MILTENYI, M.GIERLINGS, *Tuning exchange bias ,* Appl. Phys. Lett. vol 75, p15, (1999).

[8] R.JUNGBLUT, R.COEHOORN, *Orientational dependence of exchange biasing in molecular beam epitaxy grown $Ni_{80}Fe_{20}/Fe_{20}Mn_{50}$ bilayers,* J. Appl. Phys. vol.75, p6659 (1994).

[9] T.J.MORAN, J.M.GALLEGO, I.K.SCULLER, *Increased exchange anisotropy due to disorder at permalloy/CoO interfaces* ,J. Appl. Phys. vol.78, p1887 (1995).

[10] D.LEDERMAN, C.A.RAMOS, *Finite size scaling in FeF_2/ZnF_2 superlattices,* Phys. Rev. B. vol.48, p.11 (1993).

References-Chapter 1.

[11] J.NOGUES, D.LEDERMAN, I.K.SCHULLER, *Positive exchange bias in FeF_2-Fe bilayers*, Phys. Rev. Lett. vol.76, p4624 (1996).

[12] T.AMBROSE, C.L. CHIEN, *Dependence of exchange field and coercivity on cooling field in NiFe/CoO bilayers*, J. Appl. Phys. vol.83, p7222 (1998).

[13] M.KIWI, J.MEJIA-LOPEZ, R.D.PORTUGAL, R.RAMIREZ, *Positive exchange bias model: Fe/FeF_2 and Fe/MnF_2 bilayers,* Solid State Comm.vol.116, p315 (2000).

[14] M.R.FITZSIMMONS, P.YASHER, C.LEIGHTON, I.K.SCHULLER, *Asymmetric Magnetization Reversal in Exchange-Biased Hysteresis Loops,* Phys. Rev. Lett .vol.84, p3986 (2000).

[15] K.LIU, S.M.BAKER, M.TUOMINEM, *Tailoring exchange bias with magnetic nanostructures,* Phys. Rev.B,vol.63, p060403 (2001).

[16] I.N.KRIVOROTOV, C.LEIGHTON, J.NOGUES, I.K.SCHULLER, *Relation between exchange anisotropy and magnetization reversal asymmetry in Fe/MnF_2 bilayers,* Phys. Rev. B, vol.65, p100402 (2003).

[17] C.TSANG, K.LEE, *Temperature dependence of unidirectional anisotropy effects in the permalloy-FeMn systems,* J. Appl. Phys. vol.53, p2605 (1982).

[18] B.N.MILLER, E.D.DAHLBERG, *Use of the anisotropic magnetoresistance to measure exchange anisotropy in Co/CoO bilayers,* Appl. Phys. Lett. vol.69, p3932 (1996).

[19] B.N.MILLER, E.D.DAHLBERG, *Measurement of the exchange anisotropy in Co/CoO bilayers using the anisotropic magnetoresistance,* J.Appl.Phys. vol.81, p5002 (1997).

[20] C.SCHLENKER, D.PACCARD, *Couplage ferromagnétique antiferromagnétique: études des contractions de cycles d'hystérésis a l'aide d'un traceur de cycle très basses fréquences,* J.de Phys, vol.28, p611 (1967).

References-Chapter 1.

[21] C. SCHLENKER, *Couplage ferro- antiferromagnétique et traînage magnétique dans des couches minces multiple Co/CoO et Ni/NiO,* Phys. Stat. Sol.vol.28, p507 (1968).

[22] L.NEEL, *Etude théorique du couplage ferro- antiferromagnétique dans les couches minces,* Ann. Phys. Paris, vol.2, p61 (1967).

[23] D.MAURI, H.C.SIEGMANN, P.S.BAGUS, E.KAY, *Simple model for thin ferromagnetic films exchange coupled to an antiferromagnetic substrate,* J. Appl. Phys. vol.62, p3047 (1987).

[24] A.P.MALOZEMOFF, *Mechanisms of exchange anisotropy,* J.Appl.Phys, vol.63, p3874 (1988).

[25] A.P.MALOZEMOFF, *Heisenberg to Ising crossover in a random field model with uniaxial anisotropy,* Phys. Rev. B. vol.37, p7673 (1988).

[26] R.JUNGBLUT, R.COEHOORN, M.T.JOHNSON, CH.SAUER, *Exchange biasing in MBE-grown $Ni_{80}Fe_{20}/Fe_{50}Mn_{50}$ bilayers*, J. Magn, Magn. Mater. vol.148, p300 (1995).

[27] N.C.KOON, *Calculations of Exchange Bias in Thin Films with Ferromagnetic/ Antiferromagnetic Interfaces* , Phys. Rev. Lett. vol.78, p4865 (1997).

[28] J.NOGUES, T.J.MORAN, D.LEDERMAN, I.K.SCHULLER, K.V.RAO, *Role of interfacial structure on exchange biased FeF_2-Fe,* Phys. Rev. B, vol.59, p6984 (1999).

[29] T.C.SCHULTHESS, W.H.BUTLER, *Consequences of Spin-Flop Coupling in Exchange Biased Films,* Phys.Rev. Lett. vol.81, p4516 (1998).

[30] M.KIWI, J.MEJIA LOPEZ, R.D.PORTUGAL, R.RAMIREZ, *Exchange-bias systems with compensated interfaces*, Appl. Phys. Lett. vol.75, p3995 (1999).

[31] M.KIWI, Exchange *bias theory,* J. Magn. Magn. Mater. vol.234, p584 (2001).

References-Chapter 1.

[32] J.V.KIM, R.L.STAMPS, *Hysteresis from antiferromagnet domain wall processes in exchanged biased systems .Magnetic defects and thermal effects,* Phys. Rev. B, vol.71, p094405 (2005).

[33] R.L.STAMPS, *Mechanisms of exchange bias: partial wall pinning, and fluctuations,* J. Magn. Magn. Mater vol.139, p242 (2002).

[34] R.L.STAMPS, *Mechanism for exchange bias,* J. Phys D, vol.33, p247 (2000).

Chapter 2

Introduction to magnetization reversal processes and magnetic after effect

An important parameter to characterize hard magnetic systems is coercivity [1].Let us assume that a magnetic field is applied along the direction denoted (-). Coercivity appears when low field domain wall motion does not take place, either the magnetization being already saturated in zero field along the (+) direction, or domain walls being pinned at structural heterogeneities. Under such circumstances, the magnetic configuration of the system is an energy minimum in the field. This energy minimum vanishes at $H=H_C$, the coercive field. Then magnetization reversal takes place and the system reaches the lowest energy state.

The existence of coercivity is linked to that of magnetic anisotropy. This can be illustrated in a simple model due to Stoner and Wohlfarth [2], where magnetization is assumed to be uniform and magnetization reversal can only occur by coherent rotation. The Stoner-Wohlfarth model is briefly described in the first part of this Chapter. In real systems, the coercive field is much weaker then the anisotropy field. At most H_C reaches approximately $0.1H_A$. Actually coercivity is determined by structural defects. Various models to describe the link existing between coercivity and anisotropy have been proposed, which are explained in the second part of this Chapter

2.1. Coercivity

2.1.1. The classical Stoner-Wohlfarth model

In the Stoner-Wohlfarth [2] model coherent rotation of the magnetization is assumed and uniform magnetization is preserved during magnetization reversal. In uniaxial system, the energy in an applied magnetic field H can be written as:

$$E(\theta) = -\mu_0 M_S H \cos(\pi - \theta_H - \theta) + K_1 \sin^2 \theta + E_D \qquad (2.1)$$

In relation (2.1) the first term represents the Zeeman energy, the second term represents the magnetocrystalline anisotropy and the third one $E_{D,}$ represents the dipolar energy. M_S is the spontaneous magnetization, θ the angle between M_S and the easy axis c, θ_H the angle between H and the easy axis c and K_1 the second order anisotropy constant (see Figure 2.1.).

If the sample is an ellipsoid of revolution whose major axis coincides with the c-axis, E_D can be written as:

$$E_D = \mu_0 / 2\left[N_{//} M_S^2 + (N_\perp - N_{//}) M_S^2 \sin^2\theta\right] \tag{2.2}$$

where $N_{//}$ and $N_\perp$ are the demagnetizing factors along c and perpendicular to c.

The equilibrium solutions for θ are deduced from:

$$\partial E / \partial\theta = -\mu_0 M_S H \sin(\pi - \theta_H - \theta) + K_1^{'} \sin 2\theta = 0 \tag{2.3}$$

and
$$\partial^2 E / \partial\theta^2 = \mu_0 M_S Hs \cos(\pi - \theta_H - \theta) + 2K_1^{'} \cos 2\theta \geq 0 \tag{2.4}$$

where
$$K_1^{'} = K_1 + \mu_0\left[(N_\perp - N_{//}) M_S^2\right] \tag{2.5}$$

is an effective anisotropy constant including shape and magneto-crystalline anisotropies. If the applied magnetic field is initially antiparallel to the magnetization, the absolute minimum of energy, which corresponds to a parallel coupling between the moments and the field, is obtained for θ=π:

$$E(\pi) = -\mu_0 M_S H + (\mu_0 / 2) N_{//} M_S^2 \tag{2.6}$$

As long as $H < 2K_1^{'}/\mu_0 M_S$, a second minimum exists corresponding to antiparallel alignment of the magnetization and the field:

$$E(0) = \mu_0 M_S H + (\mu_0 / 2) N_{//} M_S^2 \tag{2.7}$$

The two minimum energy states are separated by an energy maximum (see Figure 2.1.):

$$E(0) = K_1^{'} + (\mu_0 M_S H)^2 / 4K_1^{'} + (\mu_0 / 2) N_{//} M_S^2 \tag{2.8}$$

where $\theta = \arccos(\mu_0 M_S H / 2K_1^{'})$

As H reaches the value of the effective anisotropy field:

$$H = H_A^{'} = 2K_1^{'} / \mu_0 M_S = 2\left[K_1 + \mu_0 (N_\perp - N_{//}) M_S^2\right] / \mu_0 M_S \tag{2.9}$$

the energy barrier is reduced to zero. If the magnetization was initially antiparallel to the field, it then rotates abruptly into the field direction: the coercive field H_C is calculated to be equal to the effective anisotropy field $H_A^{'}$.

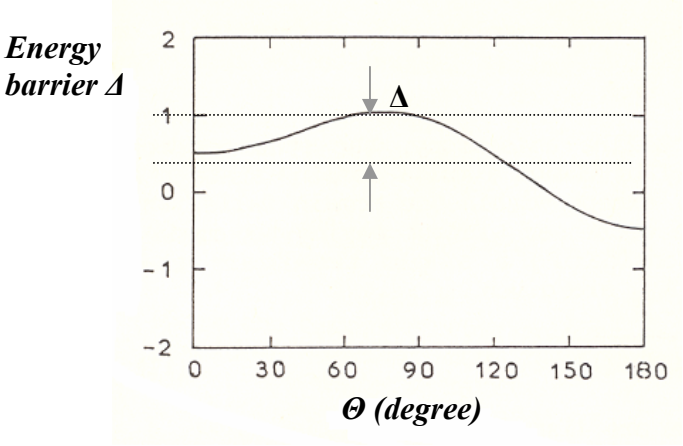

Figure 2.1. *Energy barrier at the origin of coercivity in the Stoner-Wohlfarth model (after [1]).*

In real systems the coercive field is much weaker than $H_A^{'}$. This may be attributed to the influence of structural defects. At defect position, a small volume of inverted magnetization may nucleate and magnetization reversal may develop from there. A description for the associated phenomenon will be presented in the next section.

2.1.2. Magnetic reversal in real systems

In this section and the following we will consider high anisotropy systems in which the magnetocrystalline anisotropy largely dominates shape anisotropy, which may be neglected.

The first deviation from saturation, true nucleation, occurs at a local (surface) defect when the reversal field, H_R, reaches the value of the nucleation field, H_n (H_R being the sum of the applied magnetic field H, and of the dipolar field within matter, H_{dip}) .According to SW, H_R is necessarily higher than the local defect anisotropy field, H_{defect}.

A nucleus is then formed in which the magnetization is not fully aligned along the initial easy direction. The moment configuration within the nucleus has necessarily similarities with a magnetic wall since a wall constitutes the non-uniform moment configuration of the lowest energy.

Following nucleation, the nucleus grows and enters into the main phase: the wall energy, γ, (passage mechanism) and its surface area (expansion mechanism) vary. The associated characteristic critical fields are H_{pass} and H_{expans}, respectively. Finally, possible domain wall pinning – depinning may occur when the magnetic properties vary locally within the main phase and the corresponding critical field is H_{depin}. The effective reversal field H_R is the largest of this series of critical fields, and it defines the determinant coercivity process.

These processes occur within a local critical volume under an effective critical field. This provides the physical definition of the activation volume v**.**

2.1.2.1. Nucleation and expansion

In regions where coercivity is reduced, a zone with inverse magnetization is created. It is exchange coupled to the rest of the material which is considered to have ideal properties. This regions with reversed magnetization may be assumed to be separated from the bulk by a domain wall of energy γ. Let's assume now that an additional volume v of reversed magnetization is created (see scheme in Figure 2.2.).

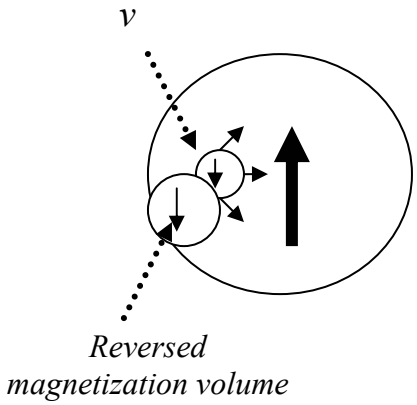

Figure 2.2. *Schema of the nucleation and expansion process.*

We ask ourselves whether this volume will collapse or expend to infinity and thus lead to full magnetization reversal. The energy variation $\delta E(v)$ associated to the creation of v is:

$$\delta E(v) = \gamma s - 2\mu_0 H M_S v \tag{2.10}$$

where s is the additional surface area resulting from the creation of v.

The volume will expend in the case when δE is negative, thus:

$$\frac{v}{s} \rangle \frac{\gamma}{2\mu_0 M_S H} \tag{2.11}$$

Expression (2.11) describes the fundamental nucleation mechanism. Solving it explicitly is difficult since neither γ nor v/s are known.

2.1.2.2. Domain wall pinning

In this section, we assume that nucleation-expansion takes place in low fields. Then in a homogenous material, domain wall motion can take place even under vanishingly small internal magnetic field. No coercivity is associated to this phenomenon. This occurs for instance in a single crystal, or in a perfect thin film [3].

In heterogeneous systems however, the energy of the domain walls varies with their position, thus providing another possible source of coercivity:

$$E(x) = -2\mu_0 M_S H dx + \frac{\delta\gamma}{dx} dx \tag{2.12}$$

where the first term represents the variation in Zeeman energy associated to a domain wall displacement dx and the second term represents the associated variation in the domain wall energy.

Due to irregularities in the dγ/dx profile, various energy minima and maxima exist for the domain wall energy γ, and they will set up energy barriers to domain wall motion (see Figure 2.3.).

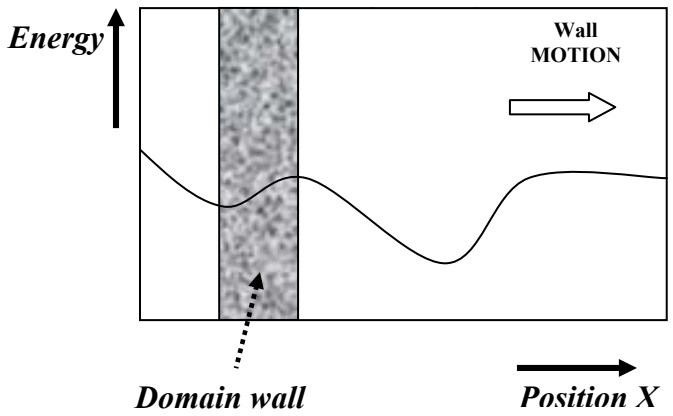

Figure 2.3. *Schematic view of the energy barriers overcome by the domain wall (in grey).*

The $\left(\frac{d\gamma}{dx}\right)$ value determining coercivity corresponds to the maximum, $\left(\frac{d\gamma}{dx}\right)_{\max}$ [4]. To this the maximum pinning force can be related. The coercive field H_C is deduced to be:

$$\mu_0 H_C = \frac{1}{2M_S}\left(\frac{d\gamma}{dx}\right)_{\max} \tag{2.13}$$

2.2. Thermal activation in coercive systems

Whatever the exact coercivity mechanism is, thermal activation adds to the energy of physical systems a factor fluctuating in course of time. If the considered system is in a stable state, the thermal activation cannot affect it irreversibly, and thus the physical parameters which characterise this state remain invariable during the measurement. By contrast, the system state may evolve with time when (i) it corresponds to a metastable state and (ii) the energy barrier to be overcome and reach the minimum energy is of the same order of magnitude as thermal activation energy.

The above concept applies to hard magnetic materials. When a field is applied antiparallel to the magnetization the system tends to reach the state of minimum energy in which the magnetization is parallel to the field. The magnetization variation with time becomes important

when the applied magnetic field approaches the coercive field and the energy barrier Δ to be overcome is reduced (see Figure 2.4).

The average time τ necessary to overcome the energy barrier Δ, is given by the Arrhenius law (see Figure 2.4):

$$\tau = \tau_0 \exp\left(\frac{\Delta}{kT}\right) \tag{2.14}$$

where τ_0 is the minimum relaxation time, of the order 10^{-9} s to 10^{-10} s .

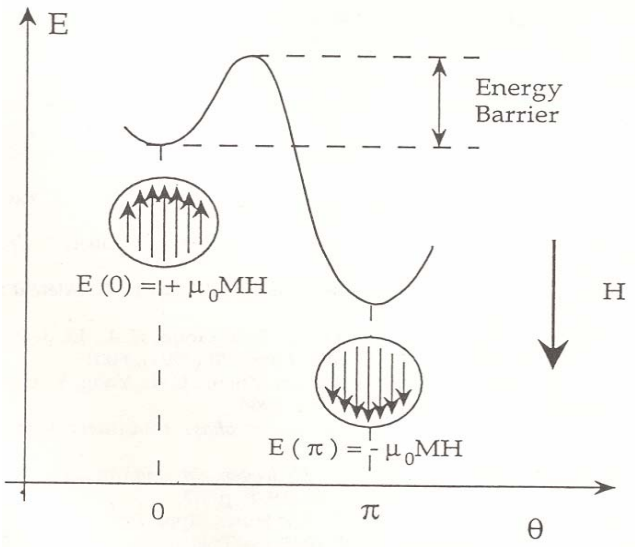

Figure 2.4. *Schematic view of the energy states.*

The phenomenon of overcoming the barrier under the effect of thermal activation is referred to as "nucleation". Here nucleation refers to the thermally activated nucleus which forms whatever the physical mechanism determining coercivity is (nucleation, expansion or propagation). It is unfortunate that the same term is used to describe two different effects. In the rest of this manuscript, the term nucleation mostly refer to the thermal activation on the energy barrier, without specifying which is the actual physical phenomenon involved.

For an ergodic system, the probability for nucleation during time t is :

$$dp = \frac{dt}{\tau} \tag{2.15}$$

where τ is the characteristic time necessary to overcome the barrier (in the following we will sometimes use the parameter R representing the nucleation rate, R=1/τ).

The total number of activated reversed nucleus N(t) at time t is derived to be:

$$N(t) = N_0(1 - e^{-t/\tau}) \tag{2.16.a}$$

where N_0 is the total number of nucleation sites per unit area.

Assuming that to each nucleation event, the same variation of magnetization 2M is associated, one derives directly from (2.16.a) the time variation of the magnetization:

$$M(t) = M_0(1 - e^{-t/\tau}) \tag{2.16.b}$$

$$M_0 = N_0 m \tag{2.17}$$

where M_0 is the magnetization in the saturated state.

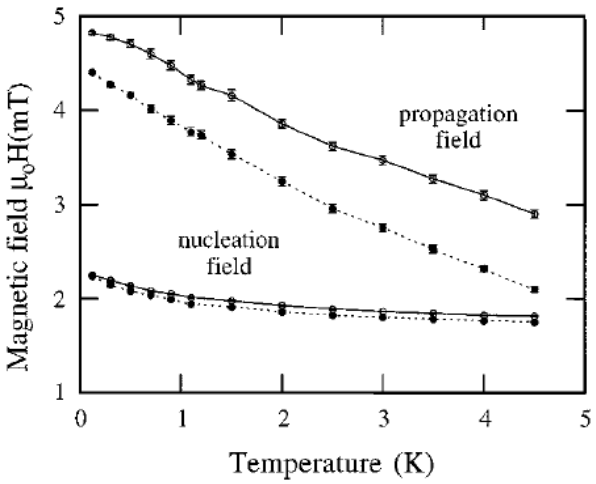

Figure 2.5. *Temperature dependence of the mean nucleation (Hn1) and propagation fields (Hp) for a GdFe(1000 Å)/TbFe(2 Å)/GdFe(500 Å)(after[5]).*

2.2.1. Fatuzzo-Labrune's model

E. Fatuzzo, in 1962, proposed a model for describing the reversal of the polarization under the effect of thermal activation in ferroelectric crystals [6].This model was later adapted for magnetic materials by Labrune et *al.* [7] in 1989, and used to study magnetic after effect in hard films [8] and in exchange bias systems with perpendicular anisotropy [9].

The model assumes that domain nucleation takes place randomly on the surface of the sample according to a statistical process. The domains formed expand sideways with a constant velocity *v*. During this expansion, a second domain, may be formed from a new nucleus (of the same type as the first one), which will start to grow as well (see Figure 2.6); then a third domain is formed and so on. After a certain time, these domains are large enough to join each other, or to "coalesce" until, through successive steps of nucleation, sideway growth and "coalescence", magnetization is completely reversed in the whole sample.

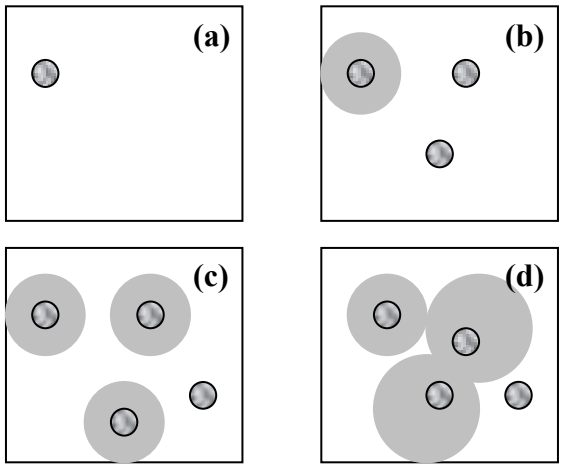

Figure 2.6. *Scheme of Magnetization reversal by nucleation (a), propagation (b, c) and coalescence (d).*

Neglecting coalescence, the area covered by the switched domains can be expressed as:

$$A(t) = \int_0^t \left(\frac{dN}{dt} \right)_s (v^2 t^2 - \pi r_0^{\,2})_{t-s}\, ds \tag{2.18}$$

where r_0 is the nucleus radius and *v* is the expansion velocity.

The value of A tends to infinity when t→∞ which is physically impossible. The reason for this is precisely the fact that the coalescence of domains and the possibility that nucleation sites are located in already reversed regions have not been considered. The actual area B(t) obtained when this is taken into account can be calculated from the area A , using a theorem due to Avrami [10]:

$$B(t) = \exp(-A(t)) \tag{2.19}$$

This theorem, however neglects the area covered by the nucleus at its birth. Taking this into account, it is found that (see Eq.30 in the Appendix in [6]):

$$B(t) = \exp\left(- A(t) + \frac{\pi r_0^2 N_0 R t}{S} - \frac{\pi r_0^2}{S} N(t) \right) \tag{2.20}$$

where S is the sample total area.

From this, one derives the fractional area B (t) not yet reversed at time t:

$$B(t) = \exp\left[- 2k^2 \left(1 - (Rt + k^{-1}) + \frac{1}{2}(Rt + k^{-1})^2 - \exp(-Rt)(1 - k^{-1}) - \frac{1}{2} k^{-2} (1 - Rt) \right) \right] \tag{2.21}$$

where $k = v/Rr_0$.

Figure 2.7 (a) shows the variation of magnetization M or $B(t)=(M(t)+M_S)/2M_S$, versus time for different applied field values. It was found that all the curves B(t) can be merged into a unique curve, magnetization versus reduced time t_R, where $t_R=t/t_{50}(H)$, $t_{50}(H)$ being the time needed under an applied field H to reverse the magnetization in half the volume of the sample (see Figure 2.7.(b)).

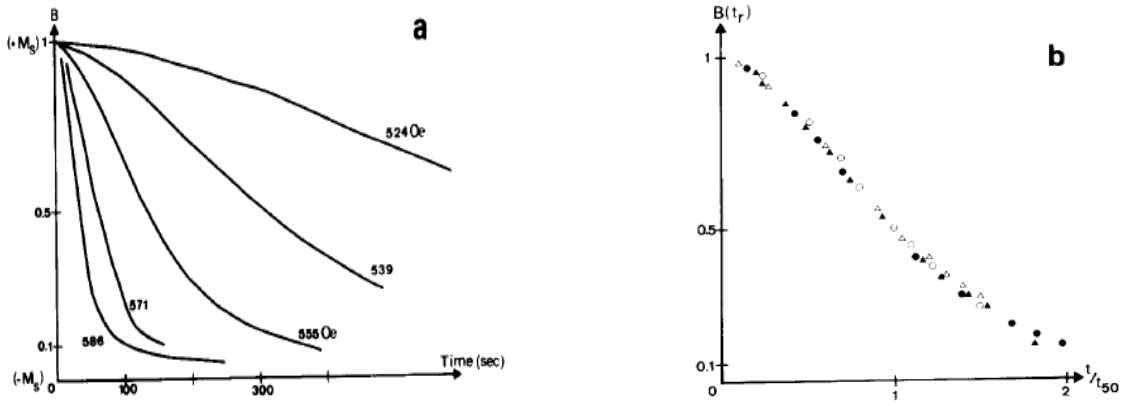

Figure 2.7. *(a) Magnetization change versus time for different applied field; (b) same curves expressed in reduced time t_R (after [7]).*

According to equation (2.21) magnetization reversal versus reduced time curves are plotted in Figure 2.8. for different values of the parameter k. Nucleation governs the reversal process for low value of k. Conversely, for large values of k, domain propagation will be dominant.

The shape of the reversal curves in Figure 2.8. depend on the "ratio" between nucleation and propagation:

-in the case of dominant nucleation (k<<1) we get from equation (2.21):

$$B(t)= \exp(-Rt)\approx \exp t/\tau \qquad \text{and} \qquad t_{50}=(1/R)\ln 2$$

where R is the probability for nucleation. The magnetization varies exponentially with time (see Figure 2.8.).

-in the case of domain wall motion only (k>>1) equation (2.21) is reduced to:

$$B(t)=\exp(-k^2R^3t^3/3) \qquad \text{which gives} \qquad t_{50}=(3\ln 2)^{1/2}/Rk^{2/3}$$

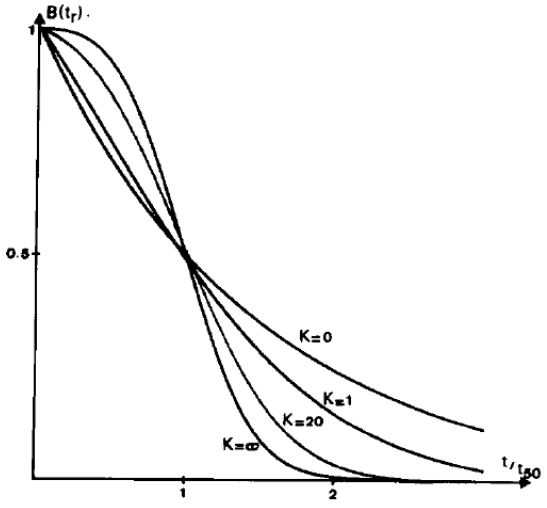

Figre.2.8.*Calculated magnetization reversal curves for different values of the parameter k (after [7]).*

For high k values the relaxation curve has an S shape as shown in Figure 2.8.

2.2.2. Large distribution of energy barriers

Hard magnetic systems, objects of our interest, are not homogenous in general. This aspect was not considered in the previous section where only one energy barrier was assumed to govern magnetization reversal. Actually, when a large distribution of barriers is present, thermal activation is profoundly modified. To discuss this, we consider that, in an inverse applied magnetic field $\mu_0 H$, each element of matter of volume v, is in a metastable state separated from the stable state by an energy barrier Δ, variable from one element to another. If we indicate by $n(\Delta)$ the number of such elements (of average volume v) for which the energy barrier is between Δ and $\Delta+d\Delta$, the irreversible variation of the system magnetic moment ,$d\mu_{irr}$, resulting from the magnetization reversal of the $n(\Delta)d\Delta$ elements will be:

$$d\mu_{irr} = 2M_S v n(\Delta) d\Delta \tag{2.22}$$

which corresponds to an irreversible magnetization variation of the system $dM_{irr} = d\mu_{irr}/V_S$ (V_S= total volume of the considered system) given by:

$$dM_{irr} = 2M_S \, {v}/{V_S} \, n(\Delta) d\Delta \tag{2.23}$$

(note that $\int_0^\infty v n(\Delta) d\Delta = V_S$). Posing $f(\Delta) = \frac{v}{V_S} n(\Delta)$ (the distribution function of the volume elements associated to one energy barrier Δ):

$$dM_{irr} = 2M_S f(\Delta) d\Delta \tag{2.24}$$

Let us discuss thermal activation effects under such conditions. The probability to overcome a given barrier Δ between time 0 and time t can be written as (see equation 2.17.(a)):

$$P(t) = \left(1 - \exp\left(\frac{-t}{\tau}\right)\right) \tag{2.25}$$

where τ is the characteristic relaxation time of the considered barrier, given by relation (2.14). Considering the properties of the exponential function :

$$P(t) \approx 0 \quad \text{for } t \le \tau \qquad \text{and} \qquad P(t) \approx 1 \quad \text{for } t \ge \tau$$

Thus, for a barrier of given high, Δ, the real time t may be identified with the characteristic time τ:

$$t = \tau_0 \exp \frac{\Delta}{kT}$$

From this, it results that the barrier Δ may be considered to be overcome at time t, such that:

$$\Delta = kT \ln \frac{t}{\tau_0} \tag{2.26}$$

Differentiating (2.24) and taking into account (2.26) the irreversible variation of magnetization with time is derived as:

$$S = \frac{dM_{irr}}{d \ln t} = 2M_S kTf(\Delta) \tag{2.27}$$

with S representing the magnetic viscosity parameter.

In the case where f(Δ) is a constant, the magnetization varies linearly with the logarithm of time. Such a liner variation is often observed experimentally. This observation implies that during time dt a small area dΔ of the energy function f(Δ) is explored (see Figure 2.9.).

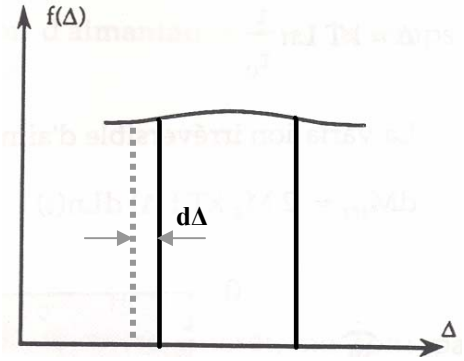

Figure 2.9.*Energy function associated to the energy barrier (the variation of f(Δ) with dΔ is sufficiently small so that f(Δ)≈ cte).*

When this applies to the entire domain of time explored, the variation of magnetization with the logarithm of time (T and $\mu_0 H$ fixed) is linear.

Another parameter that can be deduced from magnetic after effect measurements is the magnetic susceptibility χ which represents the magnetization variation under the effect of H. Two types of variations can take place under the effect of this field: a reversible variation essentially due to the exerted torque on the moments which are not collinear with the field direction (χ_{rev}) and the irreversible variation due to the magnetization reversal over energy barriers (χ_{irr}).The total susceptibility χ_{tot} can be written as:

$$\chi_{tot} = \chi_{rev} + \chi_{irr}$$

From relation (2.24), the irreversible susceptibility $\chi_{irr} = \partial M_{irr} / \partial H$ can be expressed:

$$\chi_{irr} = 2M_S f(\Delta)\left(\frac{\partial \Delta}{\partial H}\right)_T \tag{2.28}$$

From (2.27) and (2.28) we can define the magnetic viscosity coefficient S_v as:

$$S_v = \frac{S}{\chi_{irr}} = \frac{kT}{(\partial \Delta / \partial H)_T} \tag{2.29}$$

S_v and thus $(\partial \Delta / \partial H)_T$ are the essential parameter that can be deduced from magnetic after effect measurements. Wohlfarth [2] introduced the concept of the activation volume,v_a, by writing the dimensional equation:

$$\left(\frac{\partial \Delta}{\partial H}\right)_T = \mu_0 M_S v_a = \frac{kT}{\mu_0 M_S S_V} \tag{2.30}$$

v_a is the activation volume which can be identified with the volume v introduced in relation (2.10). Relation (2.30) is very generally used to derive v_a from experimental data.

2.2.3. Coercive field model

We have already explained that in real systems, the coercive field is most generally much weaker than the anisotropy field. Magnetization reversal is actually governed by sample defects. Because the defect properties are unknown, a qualitative analysis of coercivity is very difficult.

In the experimental analysis of coercivity it is common to express the reversal field as a function of the main phase anisotropy field H_A [12, 13]:

$$\mu_0 H_R = \alpha \mu_0 H_A \tag{2.32}$$

where $$\mu_0 H_R = \mu_0 H_C + \mu_0 H_{dip} \tag{2.33}$$

and α represents the detrimental effect of defects on coercivity (H_c is the experimental coercive field and $\mu_0 H_{dip}$ represents the dipolar interactions which are present in heterogeneous magnetic systems).

An alternative expression for $\mu_0 H_R$ is obtained in the global model [10]:

$$\mu_0 H_R = \alpha \frac{\gamma}{v_a^{1/3} M_S} \tag{2.34}$$

where γ is the main phase domain wall energy and v the activation volume.

Both expressions (2.32) and (2.34) are based on a questionable hypothesis: the coercive field H_c is assumed to be proportional to some intrinsic parameters of the hard magnetic phase H_A in (2.32), γ in (2.34). Actually, there is no a priori reason for the intrinsic magnetic parameters in defect regions to be proportional to the intrinsic parameters of the main phase.

Givord *et al*. [13] proposed a model which does not rest on such assumptions. Under the condition that second order anisotropy only is involved during reversal, the value of the reversal field was derived to be:

$$\mu_0 H_R = \alpha \frac{A(T)}{v_a^{2/3} M_S(T)} \tag{2.35}$$

Expression (2.35) relates the critical field to the activation volume. The main phase parameters introduced are the exchange constant A (T), and the magnetization M_S(T). Assuming that the exchange constant and the spontaneous magnetization are proportional to the same parameters in the main phase is a much less drastic assumption than assuming proportionality between critical volume and main phase anisotropies. This model was tested successfully on several hard magnetic materials [13].

References-Chapter 2

[1] D.GIVORD, Q.LU, M.F.ROUSSIGNOLL, *Coercivity in hard magnetic materials*, Science and technology of Nanostructured Magnetic Materials, Serie B, Phys. vol.259, p635 (1990).

[2] E.C.STONER, E. P.WOHLFARTH, *A mechanism of magnetic hysteresis in heterogeneous alloys,* Phil. Trans. Roy. Soc, vol. A240, p599 (1948).

[3] O.FRUCHART, J.P.NOZIERES, D.GIVORD, *Growth and interface magnetic anisotropy of epitaxial Mo/Fe/Mo(110) and W/Fe/W(110) ultrathin films,* J. Magn. Magn. Mater. vol.207, p159(1999).

[4] G.C.HADJIPANAYIS, A.KIM, *Domain wall pinning versus nucleation of reversed domains in R-Fe-B magnets,* J. Appl. Phys. vol. 63 p3310 (1988).

[5] S.MANGIN, G.MARCHAL, W.WERNSDORFER, *Dynamical measurement of nucleation and propagation in a domain wall junction at low temperature,* Europhys.Lett.vol.39, p675 (1997).

[6] E.FATUZZO, *Theoretical considerations of the switching transient in ferroelectrics,* Phys. Rev. vol.127, p1999 (1962).

[7] M.LABRUNE, S.ANDRIEU, F.RIO, *Time dependence of magnetization process of RE-TM alloys,* J. Magn. Magn. Mater. vol.80, p211 (1989).

[8] J.FERRE, *Dynamics of magnetization reversal: from continuous to patterned ferromagnetic films,* Topics in Applied Physics, vol.83, Springer

References-Chapter 2.

[9] F.ROMANENS, S.PIZZINI, J.SORT, F.GARCIA, J.CAMARERO, F.YOKAICHIYA, Y.PENNEC, J.VOGEL, B.DIENY, *Magnetic relaxation measurements of exchange biased(Pt/Co) multilayers with perpendicular anisotropy,*Eur.Phys.J.B, vol.45,P185 (2005).

[10] M.AVRAMI, *Kinetics of phase change I general theory, J.* Chem. Phys. vol.7, p1103 (1939).

[11] F.KOOLS, *Factors governing the coercivity of sintered anisotropic M type ferrite,* J.Phys. pC6-349,(1985).

[12] M.SAGAWA, S.HIROSAWA, *Coercivity and microstructure of R-Fe-B sintered permanent magnets,* J.Phys.pC8-617, Paris,(1988).

[13] D.GIVORD, M.ROSSIGNOL, V.M.T.S.BARTHEM, *The physiscs of coercivity,* J. Magn. Magn. Mater. vol.1-5, p258 (2003).

References-Chapter 2.

Chapter 3

Experimental techniques

3.1 Sample preparation

3.1.1. Sputtering deposition

We have used the sputtering method to prepare the films examined in this work. This technique was chosen due to its simplicity and possibility to prepare alloy films of any chosen composition. The RF sputtering is commonly used due to the ability to work with both conducting and insulating materials [1].

For the sample preparation, a RF sputtering system model Alcatel SCM-400 was used. This set-up was refurbished in Laboratory Louis Néel in 2002, and it is now installed in ITIMS (Hanoi, Vietnam). A schema of this set-up is shown in Figure 3.1. In addition the deposition of a coating layer to prevent sample oxidation, was realised in Néel Institute (Laboratory Louis Néel) using a face to face target arrangement.

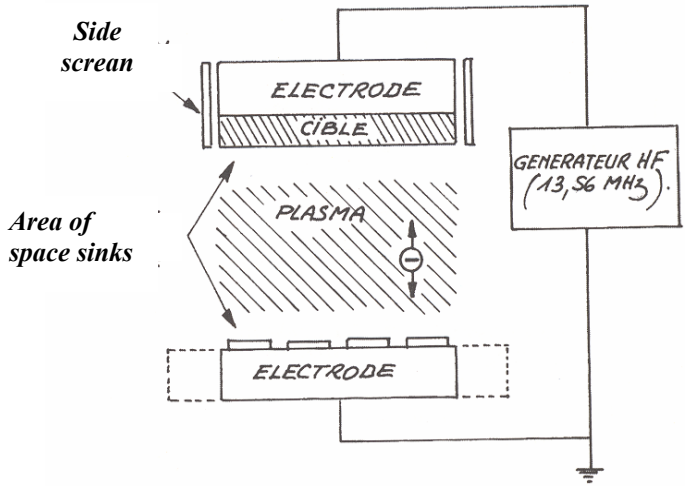

Figure 3.1. *RF sputtering principle.*

The various samples prepared were Co/MnPd bilayers deposited on a Si substrate. Samples with structure Si (100)/ MnPd/ Co were grown at room temperature by RF sputtering technique (collaboration with Prof. N.P.Thuy and co-workers at the Hanoi University of Technology) under base pressure of 10^{-6}mbar and Ar pressure of 10^{-3} mbar. During the growth, an in plane biasing field of 300 Oe was applied.

Two targets were used for sample preparation: a Co target and a MnPd target. The Co target was a simple Co disk, 5 cm in diameter and 5 mm thick. The MnPd target was a composite target made of a Pd disk at the surface of which Mn chips were bonded (see Figure 3.2.). Before preparing the MnPd/Co exchange-bias samples simple MnPd films were prepared. As expected, the composition of these films was found to be linked to the fraction of the target area covered by Mn chips. This fraction was adjusted in order to obtain the desired composition [2].

The deposition rate obtained for Co and MnPd was then determined by depositing films of about 1 μm thickness, as deduced from DEKTAK measurements. For both Co and MnPd targets, the deposition rate was of the order of 0.1nm /s.

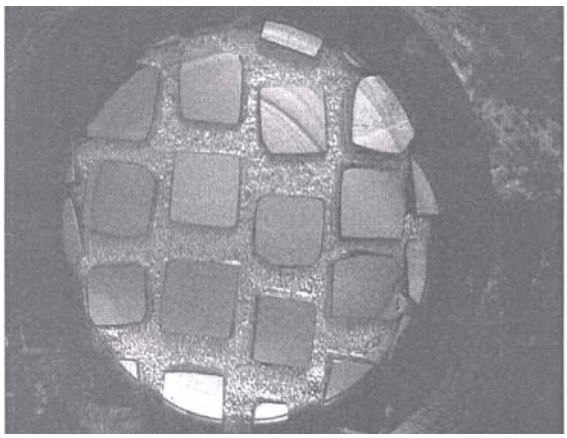

Figure 3.2. *Pd target with square Mn chips bonded to it (Top view).*

3.1.2. Film protection

In Institut Néel (Laboratoire Louis Néel), the 10nm W coating layer was deposited on already prepared samples to avoid the natural oxidation of the Co top layer. More specifically, we concentrated on three samples: S_1 (MnPd 12nm/Co 18nm), S_2 (MnPd 6nm/Co 18nm), S_3 (MnPd 3nm/Co18 nm) and S_4 (MnPd 180nm).

The sputtering system used involves a facing target configuration which is schematically shown in Figure 3.3. (a).Two disks-shape targets are arranged parallel, face to face, and the plasma established in this space. A magnetic field of a proper intensity is established perpendicular to the target surface in order to confine the high energy electrons and focus the plasma in the space between the target planes. Since the confinement of electrons can promote the ionization of the gas in the space between the targets and increase the number of sputtering ions, it raises the sputtering speed and results in high rate deposition.

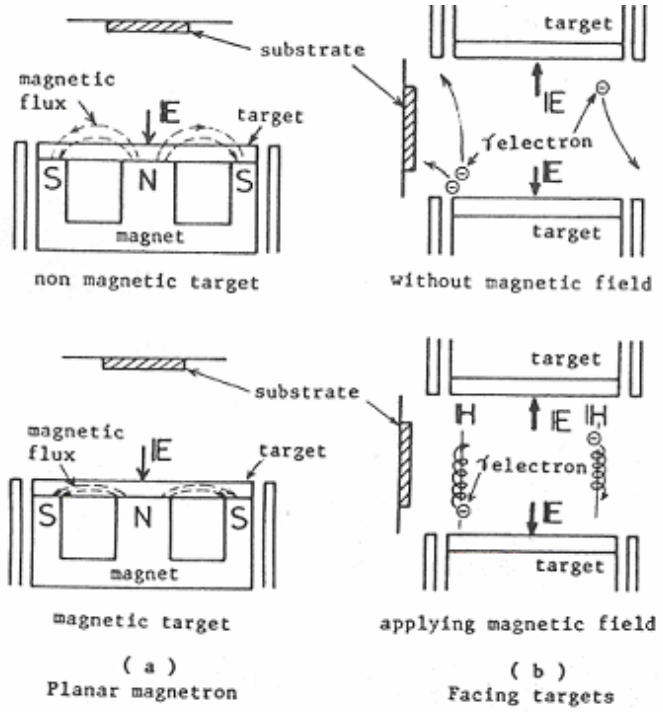

Figure 3.3. *The target configuration of sputtering machine: (a) Magnetron type; (b) Facing targets type. H and E represent the directions of magnetic field and electric field (after [3]).*

The targets are fixed on stainless steel supports, which are vertical at a distance of 3 cm the one from the other. On each target support a rectangular piece is attached, which can receive a particular target. The substrate support is a circular disk of 2 cm diameter on which 4 substrates can be placed.

During deposition the ions required for bombardment were created from argon introduced in the chamber for keeping the pressure value between 10^{-3} and 10^{-1} Torr. Before sputtering the target and the substrate were introduced in the chamber, which was evacuated down to 5.10^{-8} Torr.

3.2. Structural characterisation

3.2.1. X-ray diffraction (XRD)

In order to determine the structural properties of the thin films, it is common to use X-ray diffraction (XRD). We used θ-2θ measurements. A narrow and parallel X-ray beam, generated by an X-ray tube is incident on the sample at an angle θ with respect to the film normal (see Figure 3.4.). The beam direction is fixed while the sample and the detector are rotated so that the configuration θ-2θ is preserved during the measurements. 2θ is typically chosen to be in the range from 20° to 100°, depending on the sample. The signal recorded from the detector is plotted versus 2θ. X-ray diffraction was observed using $K\alpha_{Cu}$ radiation on a Seifert 3003 XRD TT system (λ=1.5418Å) in collaboration with XENOCS - Grenoble. The typical time to record a diagram is 10 seconds for one point using a step of 0.01°.

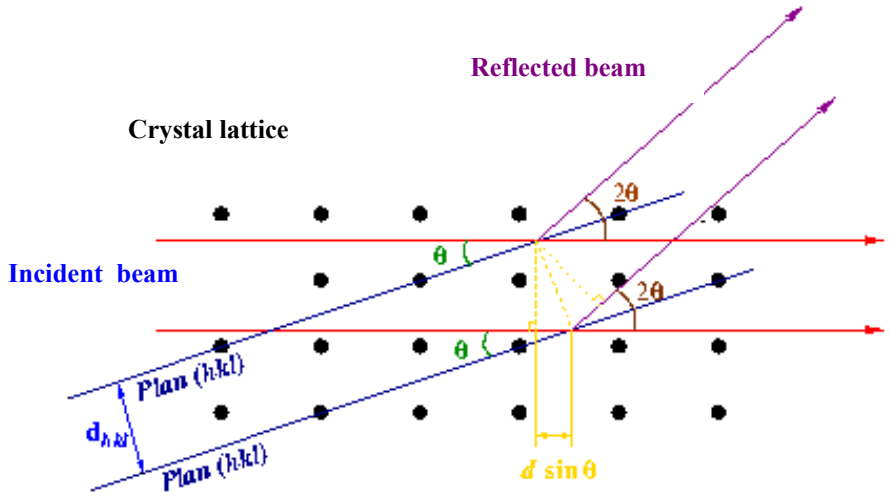

Figure 3.4. *Schematic view of XRD measurements in the θ-2θ mode.*

3.2.2. Scanning electronic microscope (SEM)

A Scanning electronic microscope (JEOL JSM-840 A) was used to investigate the structure of the samples. SEM uses a filament of tungsten, to produce electrons through thermo ionic emission and it functions as a cathode. A voltage is applied to the loop, causing it to heat up. The anode, which is positive with respect to the filament, forms powerful attractive forces for electrons. This causes electrons to accelerate toward the anode (see Figure 3.5.). The acceleration voltage is between 2.5-50 kV. The electrons are directed toward one point, by a system of lenses to produce an electronic ray spreading all over the sample. The incident electronic ray reacts with the sample, generating several types of signals. The signals are then collected in detectors, and their output is multiplied to adjust intensity on CRT[2] screen. Scanning electronic ray is synchronized with the output on CRT screen. The noticeable variations in light intensity are generated as a consequence of signal variations from point to point of the sample surface.

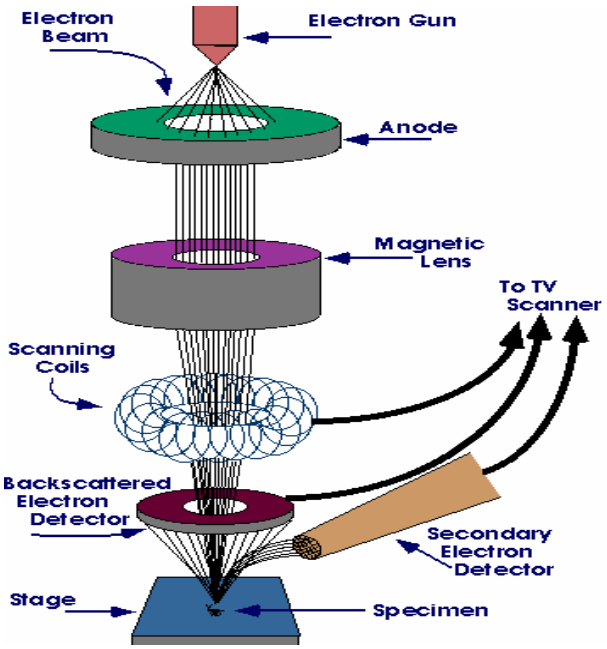

Figure 3.5. *Schematic drawing of the electron source.*

[2] CRT (cathode ray tube) works by moving an electron beam back and forth across the back of the screen. Each time the beam makes a pass across the screen, it lights up phosphor dots on the inside of the glass tube, thereby illuminating the active portions of the screen. By drawing many such lines from the top to the bottom of the screen, it creates an entire screenful of images.

The sample to be studied is placed on an aluminium support, with a glue or double-sided adhesive tape. A conductive layer must be spread on the sample's surface, to prevent electronic charge formation, with a possible reaction with incident electronic beam. In our case the protective layer was a 10nm thick W (tungsten) layer . The sample and the sample holder were placed on a stand, permitting full control of the sample positioning. On the surface and below it, certain phenomena take place when a high-energetic electron beam hits the sample. Two kinds of secondary electron signals, and background scattering electrons are generated. The secondary electrons are detected by a scintillation material that produces photons created by the electrons. This are detected and amplified by a photomultiplier tube. Due to their low energy they originate from the upper nanometers of the surface and hence, give a picture of the object's topography.

The back scattered electrons are high energy electrons. The intensity of the signal is dependent from the average atomic number. This mode gives us information about the compositional characteristics of the sample.

3.2.3 Energy Dispersive X-ray (EDX) analysis

Energy Dispersive X-ray analysis or EDAX analysis was used to determine the composition of the sample both in thin film and in bulk material. The EDX analysis system used in this thesis is the system manufactured by JEOL JSM-840 A .

During EDX Analysis, the specimen is bombarded with an electron beam inside the scanning electron microscope. The bombarding electrons collide with the specimen atoms' own electrons, knocking some of them off in the process. A position vacated by an ejected inner shell electron is eventually occupied by a higher-energy electron from an outer shell. To be able to do so the transferring outer electron must give up some of its energy by emitting an X-ray.

The amount of energy released by the transferring electron depends on which shell it is transferring from, as well as which shell it is transferring to. The atom of every element releases X-rays with unique amounts of energy during the transferring process. Thus, by measuring the amounts of energy present in the X-rays being released by a specimen during electron beam bombardment, the identity of the atom from which the X-ray was emitted can be established.

EDX spectrum (see Figure 3.6.) is just a plot of how frequently an X-ray is received for each energy level. Each of these peaks is unique to an atom, and therefore corresponds to a single element. The higher a peak in a spectrum, the more concentrated the element is in the specimen.

An EDX spectrum plot not only identifies the element corresponding to each of its peaks, but the type of X-ray to which it corresponds as well. For example, a peak corresponding to the amount of energy possessed by X-rays emitted by an electron in the L-shell going down to the K-shell is identified as a K-α peak.

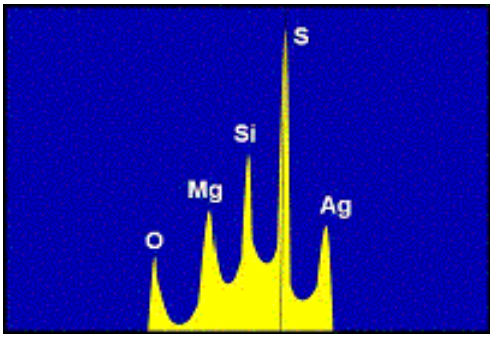

Figure 3.6*. Example of an EXD spectrum.*

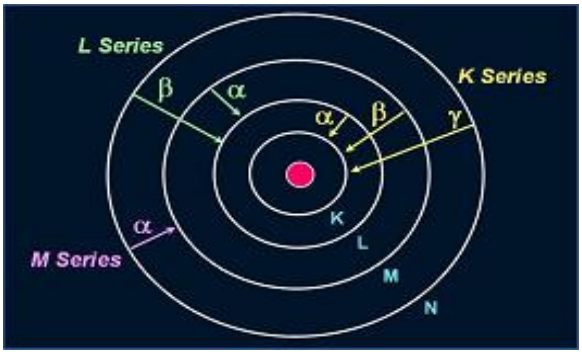

Figure 3.7. *Schematic view of the energy shells.*

The peak corresponding to X-rays emitted by M-shell electrons going to the K-shell is identified as K-Beta peaks see Figure 3.7.

3.2.4. X-ray-reflectometry (XRR)

3.2.4.1. The Principle

XRR is a non-destructive and non-contact technique for thickness determination between 2-200 nm with a precision of about 0.1-0.3 nm. In addition to thickness determination, this technique also brings information about film density and roughness. In stacks of layers, the property of each individual layer can be obtained.

The XRR method involves monitoring the intensity of the x-ray beam reflected by a sample at grazing angles. A monochromatic x-ray beam of wavelength λ irradiates a sample at a grazing angle ω and the reflected intensity at an angle 2θ is recorded by a detector (see Figure 3.8).

The reflection at the surface and interfaces is due to the different electron densities in the different layers (films), which correspond to different reflective indexes in the classical optics. For incident angles θ below a critical angle θ_c, total external reflection occurs. The critical angle for most materials is less than 0.3°. The density of the material is determined from the critical angle. Above q_c the reflections from the different interfaces interfere and give rise to interference fringes called Kiessig fringes [4].

The period of the interference fringes and the fall in the intensity are related to the thickness and the roughness of the layers. The reflection can be analyzed using the classical theory (Fresnel equation). The typical range for these measurements is between 0° and 5° in θ. For these experiments we have used an experimental set-up of the type Seifert 3003 XRD TT installed at XENOCS-Grenoble.

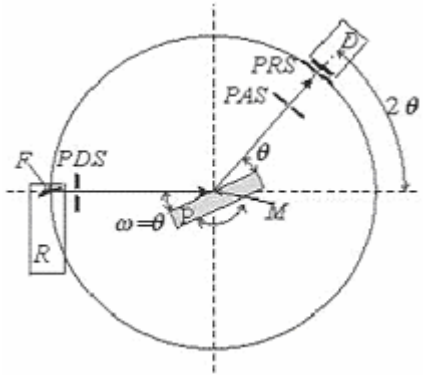

Figure 3.8. *θ/2θ -Scan: The condition of incident angle ω = (2θ)/2 = θ - outgoing angle is satisfied. The detector D rotates at twice the speed of the sample P. This arrangement is sensitive only to the planes parallel to the surface of the sample. The beam makes an incident angle ω with the surface of the sample P. The reflected intensity at angle of 2θ is measured.*

Both the rotation of the sample ω and the detector (2θ) are about the same axis MP (perpendicular to the drawing). The sample is adjusted so that the rotation axis lies on the sample surface. The Detector circle is fixed through the (programmable) detector slit. The anode focus, F of the tube lies on the detector circle.

3.2.4.2. Film density

The final experimental information given by XRR is the film density. The complex refractive index in the x-ray region is slightly less than 1 and is given by

$$\tilde{n} = 1 - \delta + i\beta \tag{3.1}$$

where δ and β represent the dispersion and absorption, respectively. For frequencies far greater than the resonance frequencies, υ_0, of the atom δ can be given by the expression:

$$\delta = \frac{e^2 n_e}{2\varepsilon_0 m(2\pi c)^2}\lambda^2 = \frac{r_0\lambda^2}{2\pi} \times n_e \tag{3.2}$$

where r_0 is the Bohr atomic radius and n_e is the electron density. The electron density is given by $n_e = Z \cdot n_{Atom}$ where Z is the number of electrons per atom. For a more precise expression of δ, Z is usually replaced with the a complex atom form factor $f = f_0 + f' + if'' = Z + f' + if''$. The term $f' + if''$ is due to dispersion and absorption and describes the x-ray absorption edge. It follows that

$$\delta = \frac{r_0\lambda^2}{2\pi} \times (Z + f') \times n_{Atom} \tag{3.3}$$

and $$\beta = \frac{r_0\lambda^2}{2\pi} \times f'' \times n_{Atom} \tag{3.4}$$

The magnitudes of δ and β are of the order of 10^{-5} and 10^{-6}, respectively. Since the atomic concentration is given as:

$$n_{Atom} = \frac{N_A}{A} \times \rho$$

it is apparent that, the density of the material can be determined from the values of δ and β. Here N_A is the Avogadro's number and A the atomic weight. The density of a compound material of known stoichiometry can also be determined from d and b with slight modifications in the formula.

For qualitative discussion, it is adequate to consider an absorption free film i.e β = 0 but it should be noted that β cannot be ignored in the simulation of XRR measurements. We consider reflection at an interface between air, $n_{air} = 1$ and another material, n1 = 1 - δ. For incident angles below a critical angle, θc, (θ < θc), total reflection occurs. By applying Snell's law and small angle approximations, the critical angle, θc can be expressed as:

$$1-\delta = \cos\theta_C \approx 1-\frac{\theta_C^2}{2}$$

$$\theta_C \approx \sqrt{2\delta} = \sqrt{\frac{r_0\lambda^2}{\pi}}\sqrt{N_A}\sqrt{\frac{(Z+f')}{A}}\sqrt{\rho}$$

3.2.4.3. Film thickness

For incident angles greater than θ_c, ($\theta > \theta_c$) the x-ray beam penetrates inside the film. Reflection therefore occurs at the top and the bottom surfaces of the film. The interference between the rays reflected from the top and the bottom of the film surfaces results in interference fringes which does not depend on the frequency like in the case of optical spectroscopy but are angle dependent. Due to the low amplitude reflection coefficient ($\rho_{v,h} \sim 1/\sin^2\theta$; $R_{v,h} = |r_{v,h|} \sim 1/\sin^4\theta \approx 1/\theta^4$) of interface between adjacent layers, contributions of multiply reflected beams can be neglected. The m-th interference maximum for a path difference $\Delta = m\lambda$, is located at:

$$m\lambda=\Delta=2d\tilde{N}_{X,1}(\theta_m) \tag{3.5}$$

$$\approx 2d\sqrt{\theta_m^{\,2}-2\delta} \tag{3.6}$$

$$\theta_m^2 \approx m^2\frac{\lambda^2}{4d^2}+2\delta = m^2\frac{\lambda^2}{4d^2}+\theta_C^2 \tag{3.7}$$

If the substrate is optically denser than the film, a phase difference of π occurs at the reflection film / substrate interface and m is replaced by m+1/2.

Employing equation (3.7) and the difference between two neighbouring maxima and minima, the thickness can be determined and is given by:

$$d \approx \frac{\lambda}{2}\frac{1}{\sqrt{\theta_{m+1}^2-\theta_C^2}-\sqrt{\theta_m^2-\theta_C^2}} \approx \frac{\lambda}{2}\frac{1}{\theta_{m+1}-\theta_m} \quad \text{for } \theta_m >> \theta_C \tag{3.8}$$

The thickness is often determined with a precision better than 0.1 nm for measurements exhibiting interference fringes in a large angular range.

3.2.4.4. Surface Roughness

Another important quantity determined from XRR measurements is the surface-and interface-roughness. Roughness gives rise to diffuse scattering, resulting to less intensity in the specularly reflected beam. General scattering formalism has been developed that calculate the scattered fields for both specular and non-specular scattering. In one of the formalism, Névot and Croce [3] considered roughness by assuming non-homogeneous thickness. They assumed that the thickness has a Gaussian distribution with a mean value d and a standard deviations σ. With this assumption ,they corrected the Fresnel coefficients of reflection $\rho_{v,h}$ as:

$$\rho_{v,h} \times \exp\left(-\frac{d}{2\sigma^2}\right)$$

3.3. Magnetization measurements

3.3.1. VSM magnetometer

Measurement principle using a VSM

A Vibrating Sample Magnetometer (VSM) was used for magnetization measurements. It is a commercial system developed by Oxford Instruments. This magnetometer uses a technique which consists in measuring the variation of the magnetic induction produced by the movement of the sample through the detecting coils. The sample is placed at the end of a stick, which is introduced into a cylindrical cryostat, surrounded by the coils. At the other end, the stick is attached to a Mössbauer type vibrator which vibrates at a frequency of 55Hz. The magnetic field is applied along the sample moving direction.

If a sample of any material is placed in the uniform magnetic field, created between the poles of the cryomagnet, a dipole moment will be induced. The oscillatory movement of the sample induces a flux variation $\Delta\Phi$ in the detection coils: $\Delta\Phi=\alpha M$. This implies the appearance in the coils of an electromotive force given by:

$$e = \frac{d\phi}{dt} = z_0 \omega \frac{m}{I} \frac{\partial B}{\partial z} \sin \omega t = e_0 \sin \omega t$$

The signal has the same frequency of vibration and its amplitude is proportional to the magnetic moment, amplitude, and relative position with respect to the pick-up coils system.

In addition to the main signal generated by the sample, parasitic signals are detected by the coils, due to the combination of coil vibration and non-uniformity of the DC field. To minimize this effect, the coil assembly is made by four coils, assembled in such a way that the signal due to field heterogeneities almost cancels out, but the sample signal does not (see Figure 3.9) [5].

3.3.1.1. Oxford VSM system

The magnetic field is generated by an NbTi superconducting coil. The maximum field that can be applied on the sample is ±8T. The field bore is at room temperature.

The detecting coils are placed within the main coil cryostat. They consist of 2 parts, located at a distance of 1 cm the one from the other, each being made of 140 000 turns. The sample temperature may be varied between 10K and room temperature by circulating cold helium inside the sample cryostat at a pressure of 10^{-1}mbar. The voltmeter sensitivity is approximately $5.10^{-9}Am^2$ (5.10^{-6}uem)

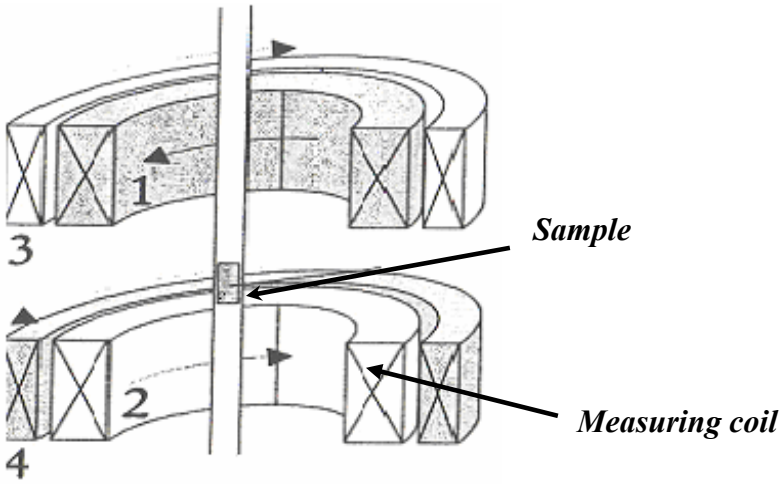

Figure 3.9. *Measuring coil of an VSM.*

3.3.2. SQUID magnetometer

Measurement principle using a SQUID

A superconducting quantum interference device (SQUID) is a system used to measure extremely weak signals specialised in the characterisation of magnetic materials that need a high sensitivity under a large temperature range. The principle of measurement is based on the vertical displacement of the sample inside coils(c), themselves placed inside the coil generating the magnetic field.

The signal detected by the coils is measured using a superconducting niobium ring, closed by a Josephson junction, named SQUID (Superconducting Quantum Interference Device).

In the laboratory system of radio frequency type, the SQUID is coupled by mutual inductance, on the one part with the couple of coils (c) assembled in opposition and on the other part to a resonant high frequency circuit (see Figure 3.10). The displacement of the sample of magnetization M induces a flow variation in the measuring coils:

$$\Delta\Phi = \alpha M \tag{3.9}$$

The current which circulate in the coils is given by:

$$I = \Delta\Phi / (2L_1 + L_2) \tag{3.10}$$

In turn, the current induces a flux variation in the superconducting ring via the coefficient of mutual inductance M_1 (see Figure 3.10.):

$$\Delta\Phi J = M_1 i \tag{3.11}$$

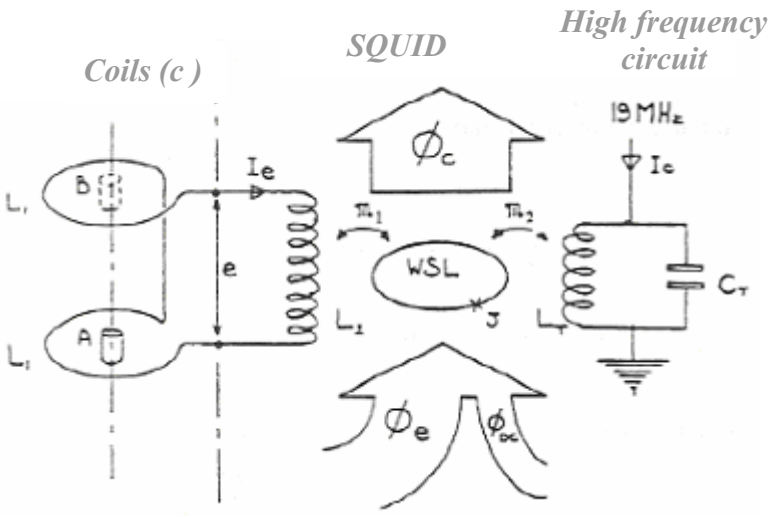

Figure 3.10. *Schematic view of the operating principle of the SQUID.*

By the action of the mutual inductance M_2 the voltage change ΔV_T measured at the out-put of the oscillating circuit:

$$\Delta V_T = Z_T i = L_T \omega \Delta\Phi J / M_2 \tag{3.12}$$

Finally according to the principle of" flow controlled mode" a system of negative feedback using the same oscillating circuit, reinjects a current i_{cr} to maintain V_T constant and to create an opposite flux variation $\Delta\Phi J$ in the Josephson loop. The flow which the ring sees is constant:

$$\Delta\Phi J = M_1 i + M_2 i_{cr} = M_1 \Delta\Phi (2L_1 + L_2) + M_2 i_{cr} \qquad (3.13)$$

The negative feedback current is directly proportional to the flow sent by the sample, thus in this case proportional to the magnetic moment. It results that the measurement of the flux variation of the negative feedback current necessary to maintain constant the flux in the superconducting ring is directly proportional to the sample magnetic moment.

3.3.2.1. Quantum design system

The SQUID used in this thesis is a commercial instrument manufactured by Quantum Design model MPMS-XL (see Figure 3.11.)[6].

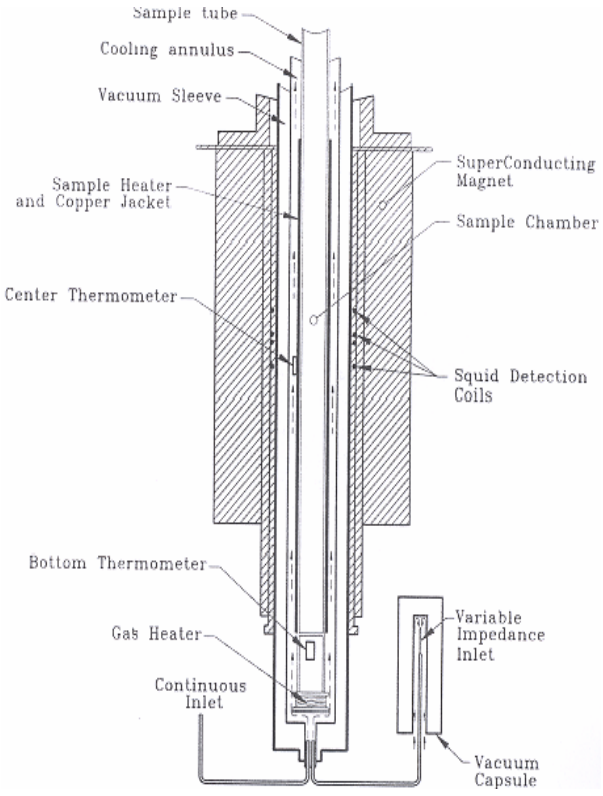

Figure 3.11. *Cross Section of the SQUID.*

The main elements of the magnetometer are:

- a superconducting magnet to produce the high magnetic fields
- two detection rings and two compensation rings
- a SQUID connected by superconducting wires to the detection coils
- surrounding shielding of the SQUID

The magnetic field is produced by an NbTi superconducting magnet of a 36 cm length with a 5cm diameter. The field can be varied between 10Oe (the remnant field of the magnet) and 50kOe with a homogeneity of 0,1% over a length of 8cm higher than the displacement range of the sample. The magnet is cooled in an helium bath placed in the cryostat.

The sample is introduced into the anti-cryostat with gas helium flow, connected to the helium bath by a capillary exchanger. A primary pumping systems maintains in the enclosure a pressure from 1 to 3 Torr and makes it possible to reach a temperature of 4K. The sample heating is made of two stages. First the gas is heated to the desired temperature; in addition, a homogenisation heater which is laid out near to the sample accelerates the thermalisation of the sample and sample holder.

The sample temperature is given by resistive measurement of a carbon probe for $T < 50K$ and by a platinum probe for $T > 50K$. The sample temperature may be varied between 4K and 400 K. Sensitivity value of the detection system is around $10^{-10}Am^2$ (10^{-7}uem).

For measurements in parallel field on the sample surface we have used as sample holder polypropylene straws and in addition adhesive kapton over the entire length of the straw to fix the sample. The sample was fixed to a sample rod mounted to an electrical part which allows the extraction of the sample.

References- Chapter 3

[1] A. RICHARDT, A-M. DURAND, *Le vide, Les couches minces, Les couches dures,* Ed. In. Fine, Paris (1994).

[2] N.N.PHUOC, N.A.TUAN, N.P.THUY, D.BABONNEAU, J.RABIER, *Anomalous magnetization process in exchange-biased MnPd/Co bilayers*, Phys.B. vol. 327, p385 (2003).

[3] M.NAOE, S.YAMANAHA, Y.HOSCHI, *Facing targets type sputtering method for deposition of magnetic metal films at low temperature and high*, IEEE Trans .Magn.vol.16, p646 (1980).

[4] H. KIESSIG, *Interferenz von Röntgenstrahlen an dünnen Schichten,* Ann. Phys. vol. 7, p51, (1931).

[5] D. DUFEU, P. LETHUILLIER, *High sensitivity 2T vibrating sample magnetometer,* Rev. Sci. Instr. vol.l70, p7,(1999).

[6] M. ELLOUI, *Couches épitaxiales magnétiques à paramètre cristallin ajustable*, Thèse Université Joseph Fourier, Grenoble1 (2004), URL. http://tel.ccsd.cnrs.fr/docs/00/04/80/30 PDF/tel-009222.pdf

References-Chapter 3.

Chapter 4

Preparation and structural characterisation of the samples

The samples studied in this thesis were prepared at Hanoi University of Technology in the framework of a collaboration with Institut Néel (Laboratoire Louis Néel).The sample preparation is described in this Chapter together with the associated structural characterisation.

4.1. MnPd phase diagram

Mn_xPd_{1-x} alloys exist for values of x between 0 and 1. For x < 29%, the alloys crystallise in the fcc structure of Pd. Under thermal treatment, superstructures may appear in the fcc phase which characterise the existence of a certain ordering between Mn and Pd atoms. In quenched alloys at low Mn concentration, the ordering is very limited [1, 2, 3] (see Figure 4.1.).

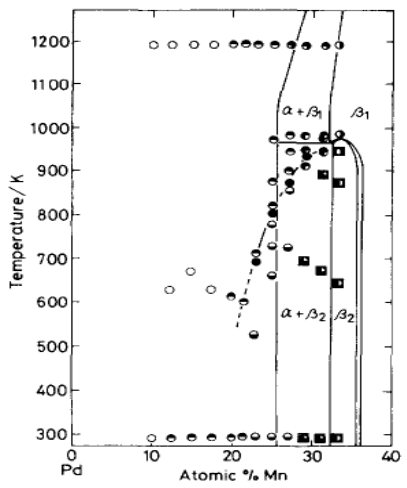

Figure 4.1.*Various Mn-Pd phases appearing in the composition range between Pd-10% Mn and Pd-33,3% Mn (after[1]).*

As shown in Figure 4.2, the *a* parameter of Mn_xPd_{1-X} alloys increases with the increase in Mn content from 0.389 nm at x=0 to 0.391 at x= 33 (see Figure 4.2.).

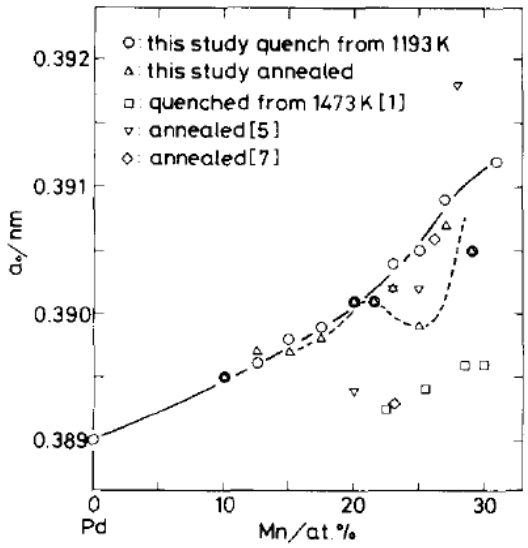

Figure 4.2*.The room temperature lattice parameters of the α phase in Pd-Mn alloys as a function of manganese content, together with previously reported results (after[1]).*

The crystallographic and magnetic structure data collected by neutron diffraction for the Mn-Pd alloys studied in [2] are presented in table 1 (where a, c are the lattice parameters, S is the long range order parameter and φ_c represents the angle between the direction of the magnetic moments and the axis c).

at % Mn	19.5	22.7	25.3	30.4
a(nm)	0.387	0.387	0.387	0.393
c(nm)	-	1.548	1.548	1.505
c/a	1	4	4	3.83
S	-	0.85±0.05	0.9±0.05	1±0.05
$\mu_{Mn}(\mu_B)$	-	4.2±0.3	4.1±0.3	4.1±0.3
$\varphi_C(^\circ)$	-	0±2	8±2	90±2
T_N(°K)	-	205±15	220±10	235±10

Table 1. *Crystal and magnetic structure data for Mn-Pd alloys measured at T=77K [1].*

4.2. Sample preparation

A series Co/MnPd bilayers were prepared in which the Co nominal thickness was 18nm and the MnPd thickness was 12nm (sample S_1), 6nm (sample S_2) and 3nm (sample S_3) respectively (see Table2).

Material *(Name)*	**MnPd thickness** *(nm)*	**Co thickness** *(nm)*
Co/MnPd (S_1)	12	18
Co/MnPd (S_2)	6	18
Co/MnPd (S_3)	3	18
MnPd (S_4)	180	-

Table 2. *Different prepared Co/MnPd samples.*

The samples were grown at room temperature by RF sputtering (see Chapter 3) in the group of Prof. N.P.Thuy at the Hanoi University of Technology. A simple scheme illustrating the layer stacking is presented in Figure 4.3.

A protective 10nm W coating layer was deposited at Institut Néel using the facing targets sputtering (see Chapter 3) on already prepared samples.

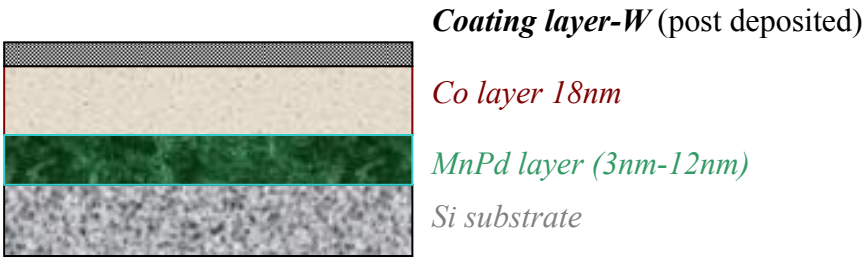

Figure 4.3*. Scheme illustrating the stacking of the layers constituting the various samples.*

4.3. Structural and topological characterisation

4.3.1. X-ray diffraction on the MnPd sample (XRD)

Due to the very small thickness of the various films prepared, the X-ray analysis could not be used for their structural characterisation. However a 180nm thick MnPd film was specifically prepared for characterisation of the antiferromagnetic MnPd layers, using the same fabrication technique.

The associated X-ray diagram is shown in Figure 4.4. taken with the $K\alpha_{Cu}$ (λ=1.5418 Å), radiation on a Seifert 3003 XRD TT spectrometer.

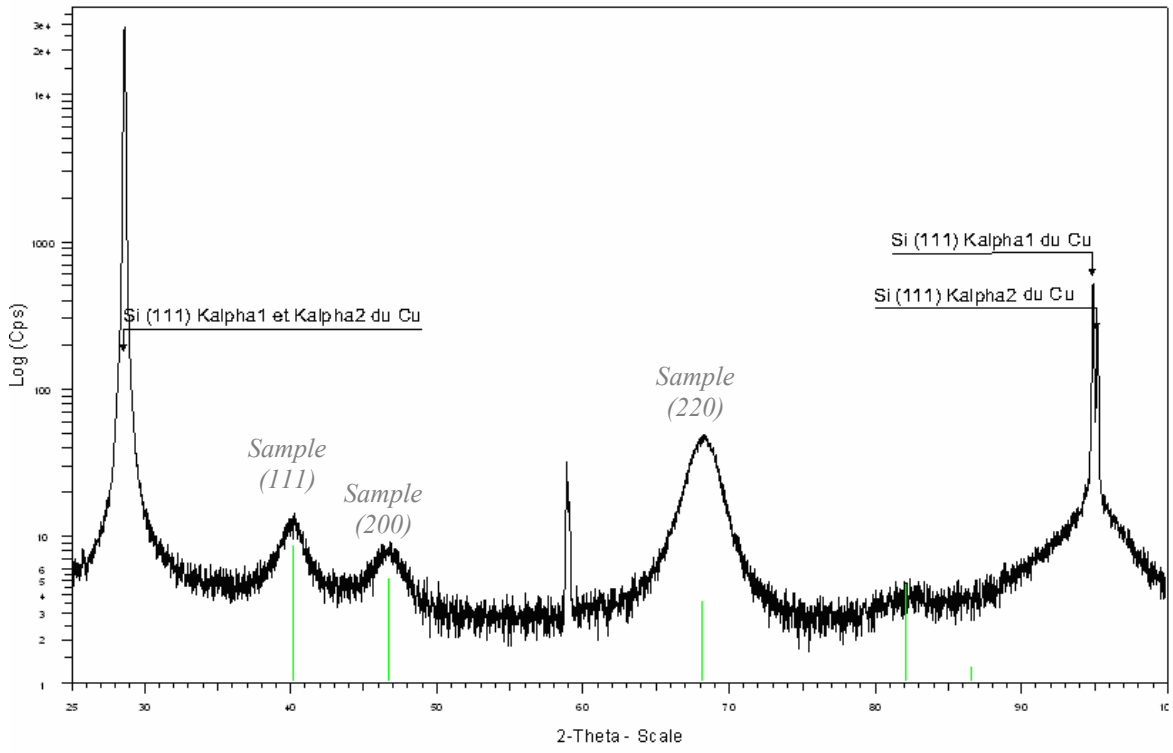

Figure 4.4. *X-ray diffraction measurement for the 180nm MnPd film.*

The intense peaks at 2θ = 28.5°, 2θ = 58,9° and 2θ = 94,9° are parasitic signals due to the substrate and /or sample holder as was shown by measuring the diagram of a virgin substrate. The three broader peaks at 2θ = 40°, 2θ = 46.6° and 2θ = 68° may be indexed as (111), (200) and (220) fcc-disordered α-phase reflections of MnPd, with *a*~0,3896nm (see Table 3).The associated chemical composition is $Mn_{16}Pd_{84}$ as derived from [1].

2θ	**θ**	**sinθ**	$\frac{\lambda\sqrt{h^2+k^2+l^2}}{2\sin\theta}=$ **a(nm)**
40	20	0.342	0.3897
46.6	23.3	0.395	0.3894
68	34	0.559	0.3896

Table 3. *Values of the crystallographic a parameter for the (111), (200) and (220) reflections deduced from the analysis of the180nm MnPd film.*

EDX analysis was performed on the same sample, Mn_xPd_{1-x} alloys. The x value derived from this analysis is around 0,16 (see table attached to Figure 4.5) in agreement with the value derived from X-Ray measurement and a little less then the desired value x ≈ 0.2.

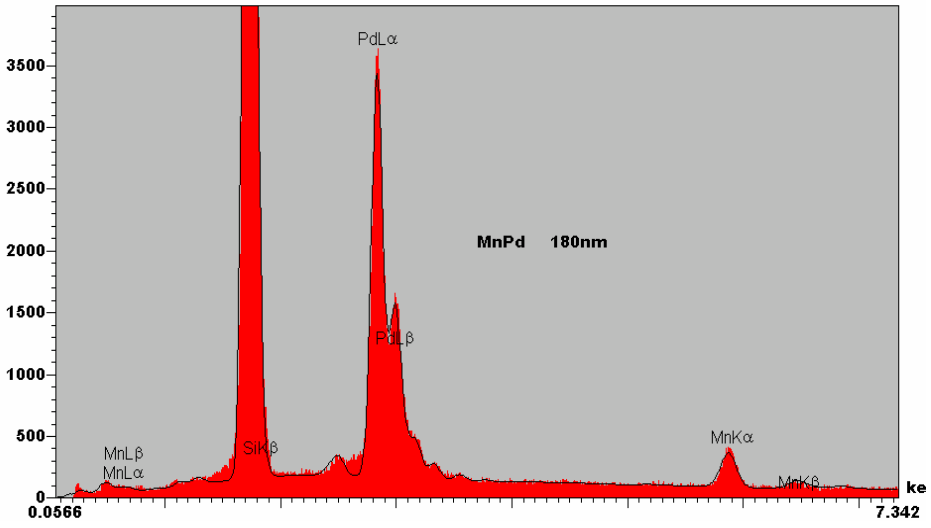

Results				*Chemical analysis*		
Elt	**Line**	**Int**	**Err**	**W%**	**A%**	**ZAF**
Si	K	555	1	0,00	0,00	1
Mn	K	14	0,2	8,9	15,9	1
Pd	L	141	0,7	91,1	84,1	0,8
Total				100	100	

Figure 4.5. *EDX spectrum for the MnPd sample with t=180nm.*

In our analysis it will be implicitly assumed that the thin films which are part of the Co/ MnPd bilayers have the same characteristic structure as the above MnPd film.

4.3.2. Scanning electronic microscope analysis (SEM)

The sample topology was characterised using Scanning electronic microscope (JEOL JSM-840 A) by collecting the secondary electrons. In most cases the images were acquired using an acceleration voltage of 20kV, leading to a spatial resolution around 2μm. As shown in Figure 4.6 all the samples were found to be continuous. For the 3nm and 6 nm Co/MnPd films the images reveal features with typical size around 20nm which we think represents the sample grain size. In the case of the 12nm film the typical size is around 50nm.

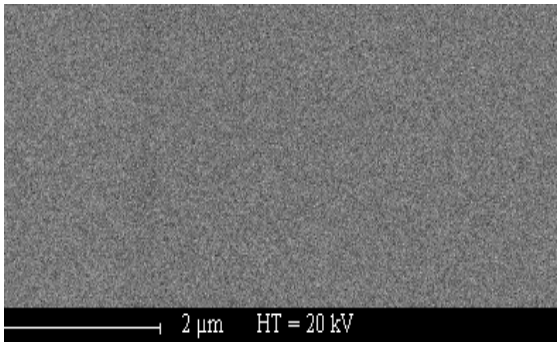

MnPd thickness 3nm

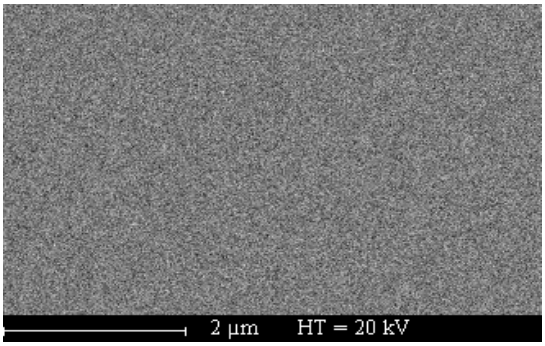

MnPd thickness 6nm

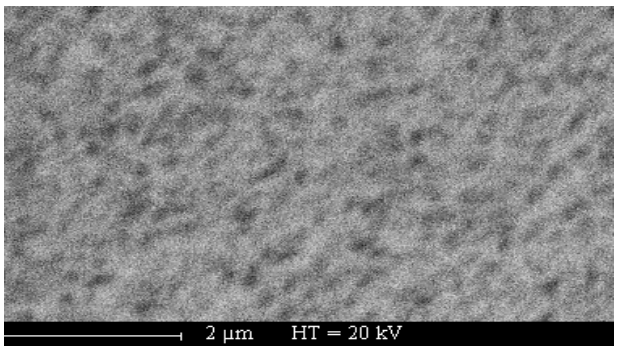

MnPd thickness 12nm

Figure 4.6*. SEM observation on the Co/ MnPd films.*

4.3.3. Energy Dispersive X-ray (EDX) analysis

EDX spectra of three different samples are presented in Figure 4.7. (a) corresponding to sample S_1, (b) corresponding to sample S_2 and, (c) corresponding to sample S_3. In addition to the large silicon signal, which comes from the substrate, we may distinguish several peaks corresponding to: Mn, Co and Pd. The evolution of the CoK_α, MnK_α and PdL_α peaks intensity gives information about the thickness variation from one sample to another.

The normalised intensities of the CoK_α peaks have always the same value testifying for a constant Co thickness in the three analysed samples. Comparing now the normalised intensities of the PdL_α peaks in the different samples the ratio between sample S_1 (Figure 4.7. (a)) and sample S_3 (Figure 4.7. (c)) is 1/4 corresponding to the value of the ratio of the MnPd layer thickness (12nm in S_1 and 3nm in S_3).

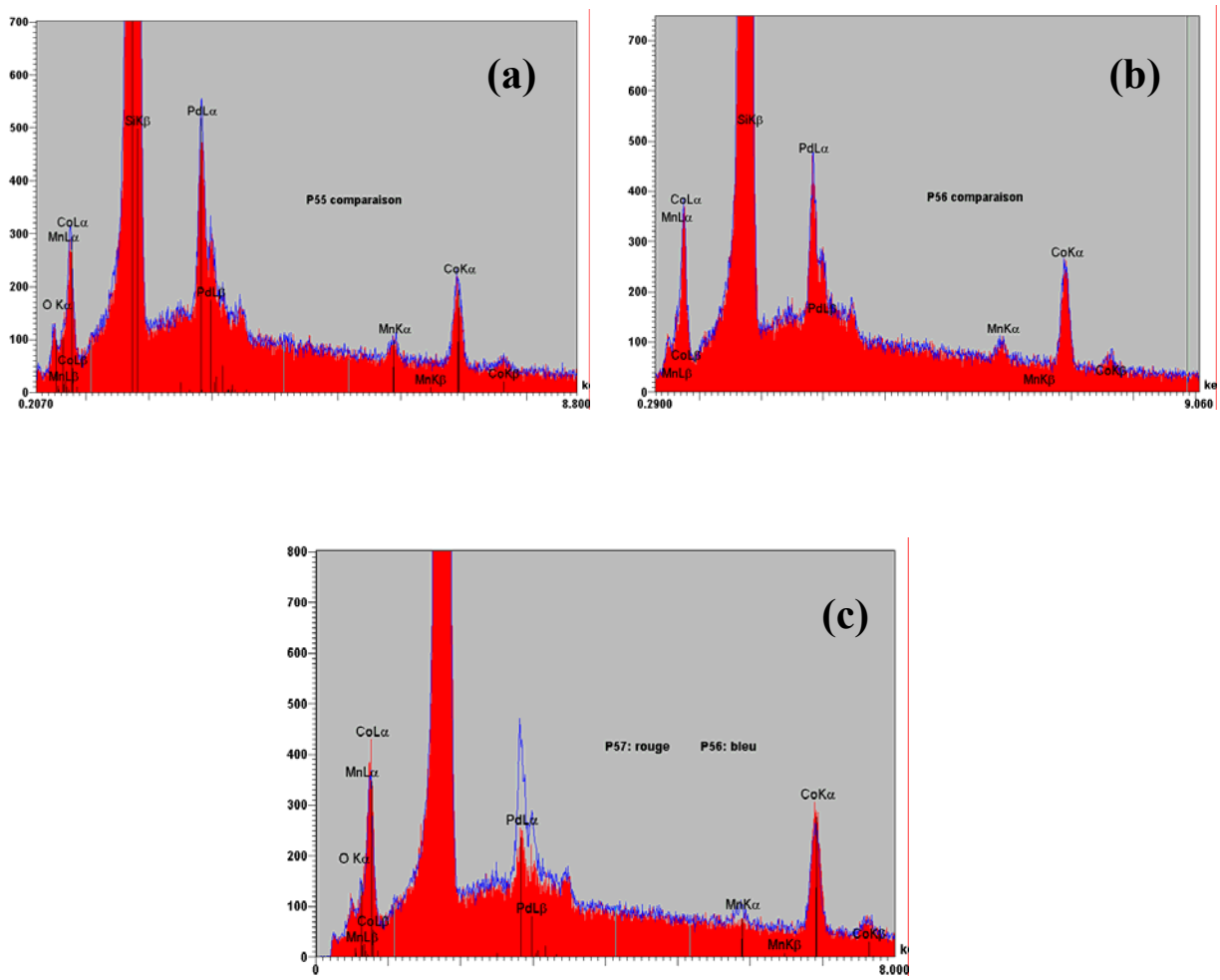

***Figure 4.7** EDX spectrums for the sample S_1, S_2 and S_3.*

Finally in Figure 4.7 (c), the relative intensities of the MnK_α peak is again smaller than in Figure 4.7. (a) and Figure 4.7 (b). This agrees with the fact that the MnPd thickness in sample S_3 is reduced to 3nm.

As shown in Table 4.(a) for sample S_1, the intensity ratio MnK_α,/ PdL_α is approximately 0.1, indicating that the chemical composition of the MnPd thin films in the bilayer systems is of the same order as in the 180nm thick layer (see Table 4. (b)), of the order of Mn_{16} Pd_{81}.

Results				***Chemical analysis***		
Elt	**Line**	**Int**	**Err**	**W%**	**A%**	**ZAF**
Si	K	868	1,7	0,00	0,00	1
Mn	K	2	0,08	7	14	1
Co	K	8	0,16	0,00	0,00	1
Pd	L	20	0,25	93	86	8
Total				100	100	**(a)**

Results				***Chemical analysis***		
Elt	**Line**	**Int**	**Err**	**W%**	**A%**	**ZAF**
Si	K	555	1	0,00	0,00	1
Mn	K	14	0,2	8,9	15,9	1
Pd	L	141	0,7	91,1	84,1	0,8
Total				100	100	**(b)**

Table 4. (a) *. Chemical composition values in sample S_1* ***(b).*** *Quantitative values of the chemical composition in the 180nm thick MnPd layer.*

4.3.4. X-ray-reflectometry (XRR)

We tempted to use X-ray reflectometry for analysing the layer thicknesses. These measurements where performed at XENOCS with the support of Ing. Dan Cenda. The reflectometer used is of the type Seifert 3003 XRD TT system.

The reflectivity intensities were collected at low angles between 0°-2° using the θ-θ measurement mode. Two samples were analysed: sample S'_1 (Co/MnPd 12nm/18nm) and S'_2 (Co/MnPd 6nm/18nm) from the same family as the samples S_1 and S_2 but without the protective 10nm W coating layer. The choice felt on S'_1 sample and S'_2 due to the reduced dimension of samples S_1 and S_2. The results are presented in Figure 4.8 and Figure 4.9 respectively. Oscillations are clearly seen which are characteristic of such ultra-thin stacks of various layers. The data were analysed using the software IMD.4.1.1. The other free parameters considered in the analysis were:

-the thickness of the Co and MnPd layers, the roughness of the top CoO layer, the roughness of the Co layer, the interfacial roughness between the Co and MnPd and between the MnPd layer and the Si layer, MnPd layer density. Unfortunately it was not possible to obtain a really satisfying fit of these data, so that the conclusions deriving from this analysis remain at a very qualitative level.

The experimental thicknesses derived from XRR analysis is in reasonable agreement with the expected ones (see Table 5). However, due to the poor correspondence between experimental data and calculated ones these results should be treated with a certain care. Note also that it was needed to assume that a 2nm CoO layer is formed at the sample surface.

	Co- Layer thickness(nm)	***MnPd- Layer thickness(nm)***	***MnPd- roughness* σ(Å)**	***Co/MnPd Interfacial roughness* σ(Å)**
Sample S_1	Nominal : **18** From XRR :**14** From mag .meas. :**13**	Nominal :**12** From XRR :**11**	From XRR :**12,8**	From XRR :**8**
Sample S_2	Nominal : **18** From XRR :**12** From mag .meas. :**14**	Nominal :**6** From XRR :**4,5**	From XRR :**12,8**	From XRR :**10**

Table 5. *Layer thickness and interface roughness values (σ (Å)) for samples S_1, S_2 determined from X-ray measurements and magnetic measurements data.*

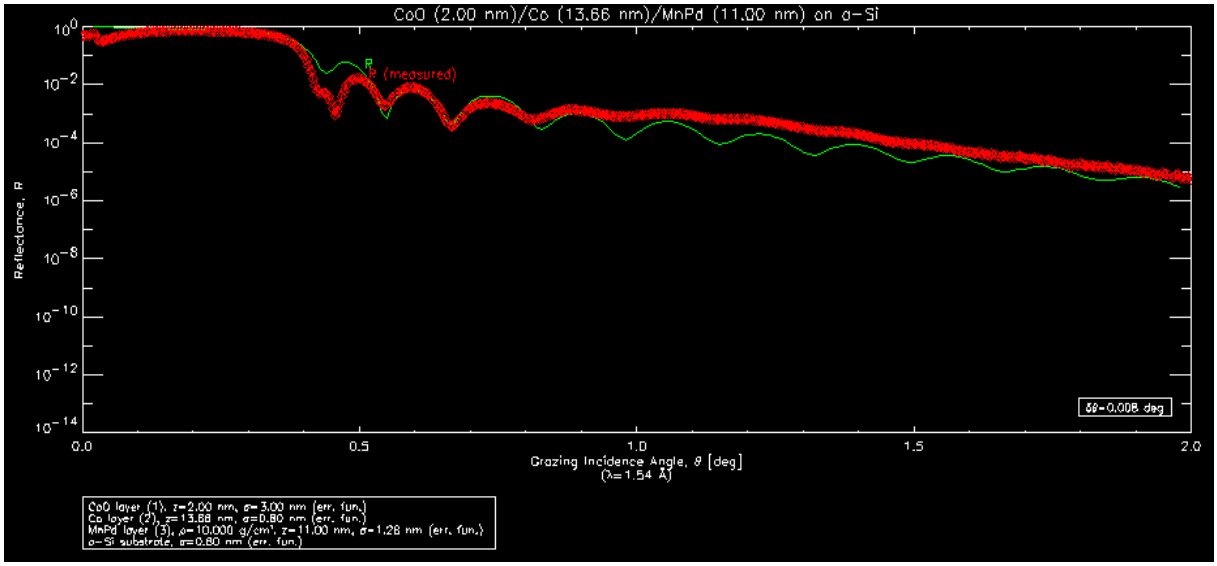

Figure 4.8. *X-ray specular reflectivity and fit for sample S_1.*

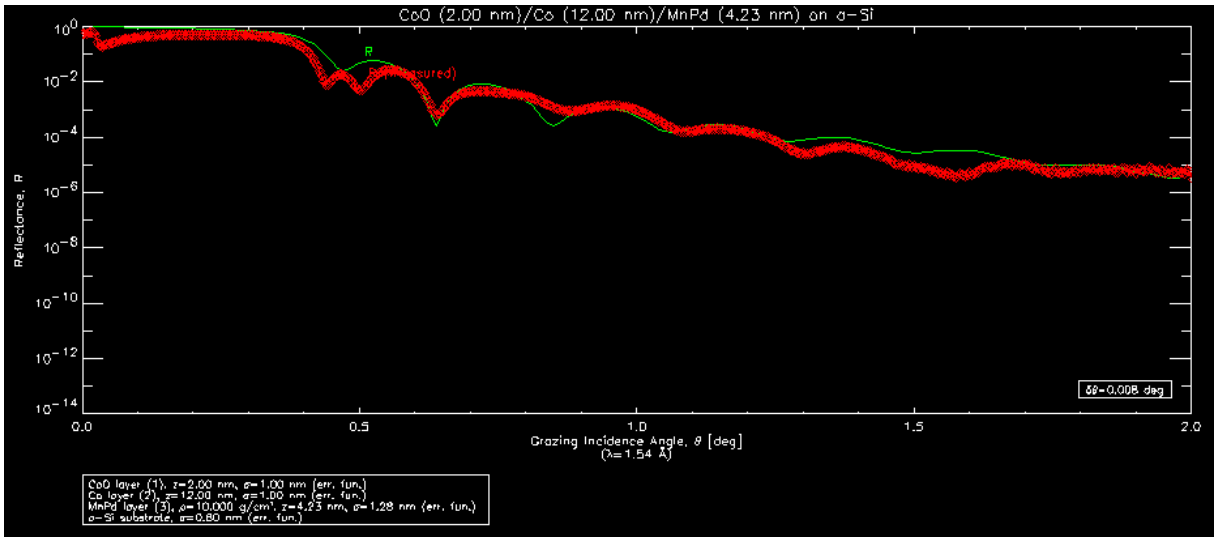

Figure 4.9. *X-ray specular reflectivity and fit for sample* S'_2.

4.3.5. Co thickness derived from magnetization measurements

Magnetization measurements were also used as an alternative method to determine the Co thickness in the various samples. In this analysis, it was assumed that Co atoms only contribute to the saturated magnetization in high fields. Thus the sample moment m_S may be expressed as:

$$m_S = M_{Co} * V_{Co}$$

where M_{Co} is the Co magnetization(M_{Co}=1,37*10^{6}A/m) and V_{co} is the Co volume which may be written as:

$$V_{Co} = A_{Co} * t_{Co}$$

where A_{Co} is the sample area.

Since the deposited layer covers all the silicon substrate, A_{Co} is identical to the silicon substrate area A_{Si}. To determine A_{Si}, we used the fact that the sample thickness (and mass) is much less then that of the Si substrate.

Thus, from the known Si density (ρ_{Si} = 2,33*10^3 kg/m^3) and substrate thickness (t_{Si} = 0,44*10^{-3}m) the sample surface area A_{Co} is derived by weighting and identifying the weighted mass to that of the substrate only:

$$A_{Co} = A_{Si} = \frac{m_{Si}}{\rho_{Si} t_{si}}$$

The thickness of the Co layer is thus calculated using the expression.

$$t_{Co} = \frac{m_S}{M_{Co} A_{Co}}$$

The t_{Co} values obtained by this method are listed in Table 5. They are in good agreement with both the expected values and X-ray reflectometry values.

4.4. Conclusions

The analysed systems in this thesis were fabricated from a Co layer deposited on the top of a MnPd layer and recovered by a 2nm thick CoO layer as it was found by XRR reflectometry, due to the natural oxidation of the Co. This implies that the Co ferromagnetic layer is coupled to an antiferromagnetic layer on both sides: MnPd on one side and CoO on the other. The question thus arises whether exchange bias is dominated by Co-MnPd coupling or by Co-CoO coupling.

Several studies on Co/CoO systems [4, 5, 6], where the CoO layer was obtained by natural oxidation (exposure to atmosphere) having a thickness of 2,5nm and the Co nominal thickness being around 9nm, have found as maximum value for the interface coupling energy $\Delta\sigma = 0.56\times10^{-3} J/m^2$.

For the studied Co/MnPd systems, in this thesis, the values for the interface coupling energy was found to be: $\Delta\sigma = 2{,}46\times10^{-3} J/m^2$,for an exchange bias field $\mu_\circ H_E$=0,055T measured at T=15K knowing that the thickness of the Co layer is t_{Co} =18nm.We are thus lead to conclude that in the present system exchange bias is largely dominated by Co-MnPd coupling.

References-Chapter 4

[1] K.BABA, Y.NIKI, Y.SAKAMATO, *The phase transition in palladium-manganese alloys with up to 33,3at.% Mn*, J. of. Alloys and Compounds vol.179, p321 (1992).

[2] E.KREAN, G.KADAR, *Crystal and magnetic structures in the Mn-Pd system near* $MnPd_3$, Phys. Lett. vol. 29A, p340 (1969).

[3] E.KREAN, G.KADAR, M.MARTON, *Neutron diffraction study of the* $MnPd_3$ *phase,* Sol.Stat.Com. vol.10, p1195 (1972).

[4] V.STROM, E.D.DAHLBERG, *Determination of exchange anisotropy by means of ac susceptometry in Co/CoO bilayers,* J. Appl. Phys. vol.81, p5003 (1997).

[5] F.RADU, M.ETZKORN, T.SCHMITTE, *Interfacial domain formation during magnetization reversal in exhange-biased CoO/Co bilayers,* Phys. Rev. B vol.67, p134409 (2003).

[6] E.D.DAHLBERG, B.MILLER et al., *Measurements of the ferromagnetic/ anti-ferromagnetic interfacial exchange energy in Co/CoO and* Fe/FeF_2 *layers,* J.Appl. Phys. vol.83, p6893, (1998).

Chapter 5

Exchange-biased hysteresis loops

5.1. Observing exchange-bias at 15K

In this Chapter, the magnetic properties of the prepared Co/MnPd bilayers are investigated. In particular we concentrate on measurements of the hysteresis cycles at different temperatures.

Let us consider sample S_2 (Co/MnPd 6nm/18nm) as an arbitrary chosen example. The hysteresis cycle shown in Figure 5.1 was obtained by cooling the sample from room temperature under a field of 4T, down to T=15K. Once at T=15K, decreasing the field values to $\mu_0 H = 0$T the magnetization remains essentially saturated ($m = 0.35 \cdot 10^{-6} Am^2$).

As the field is reversed and its amplitude increased, the magnetization remains almost saturated until the field reaches the value $\mu_0 H = -0{,}22$T. At this value, a sudden reversal of magnetization is observed and the magnetization reversal is almost complete at $\mu_0 H = -0{,}25$T.The field dependence of the magnetic differential susceptibility associated to these measurements, and characterising the 1st branch of the hysteresis cycle, is plotted in Figure 5.2. The susceptibility peak ($\chi = 0{,}034 * 10^{-3}$ Am^2/T) is observed for $\mu_0 H_1 = -0{,}23$T which defines the critical field value.

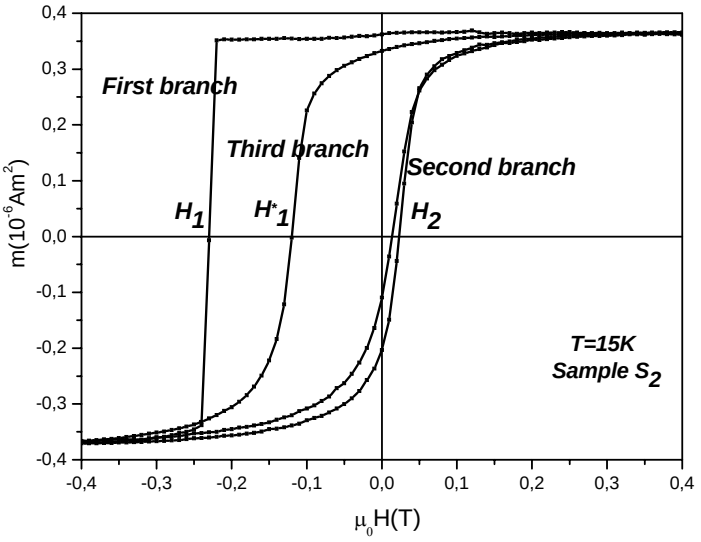

Figure 5.1. *Hysteresis cycle measured at T=15K (sample S_2).*

After reversal, the magnetization progressively approaches full saturation. As the field is reduced back the magnetization starts to decrease from μ_0H = -0.2T to μ_0H=0T (Figure 5.1). In weak positive field the magnetization varies rapidly. At μ_0H = 0.08T, the magnetization has approximately the same value it had at μ_0H = -0,25T during first reversal. The susceptibility as a function of the applied magnetic field along this second branch of the cycle provides the value of the field H_2= 0,027T as shown in Figure 5.2. Note that the associated susceptibility χ_2=0,012*$10^{-3}$$Am^2$/T is three times smaller than the one at H_1 illustrating that this latter process is more progressive that the former one.

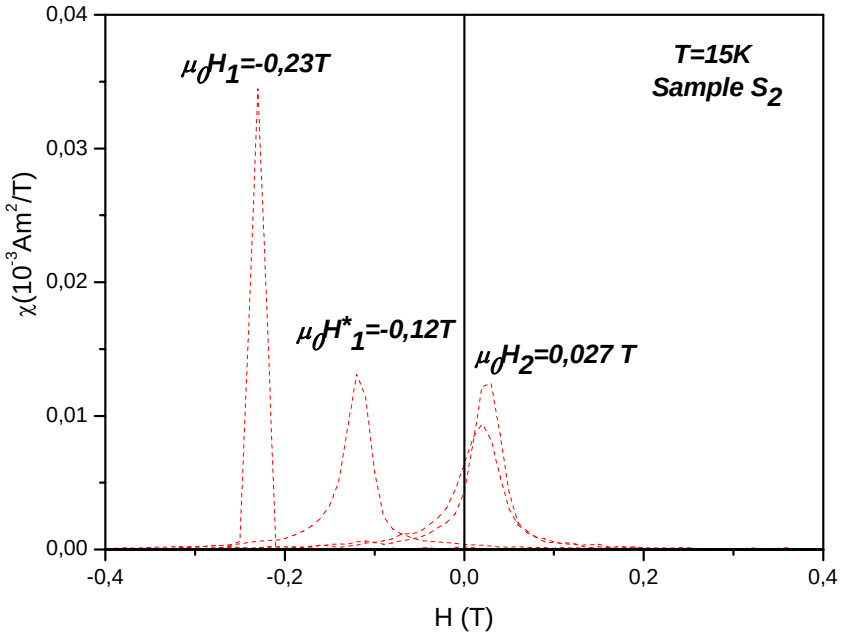

Figure 5.2. *Irreversible susceptibility versus applied magnetic field for sample S_2 at T=15K.*

Measuring again the hysteresis cycle for a second time (and further times) it appears that reversal in negative applied field differs strongly from first reversal. The switching field value H_1^* along the associated third branch is $\mu_0H^*_1$= -0,13T instead of μ_0H_1= -0,23T. The hysteresis cycle is almost stabilised during further measurements. The progressive change in the hysteresis cycle found as the field swept several times from positive values to negative ones and reciprocally is a property of many exchange bias systems, called *training effect* [1, 2, 3].

At T=15K, the second and third branches of the hysteresis cycle are simply shifted the one with respect to the other by a constant value (equal to $\mu_0H^*_1$+ μ_0H_2). As a result the magnetization dependence of the irreversible susceptibility along these two branches are almost exactly superimposed (see Figure 5.3. (a)). As temperature is progressively increased, reversal along the second and third branches becomes more abrupt and the magnetization dependence of the irreversible susceptibility along these two branches is different (see Figure 5.3.(b)).

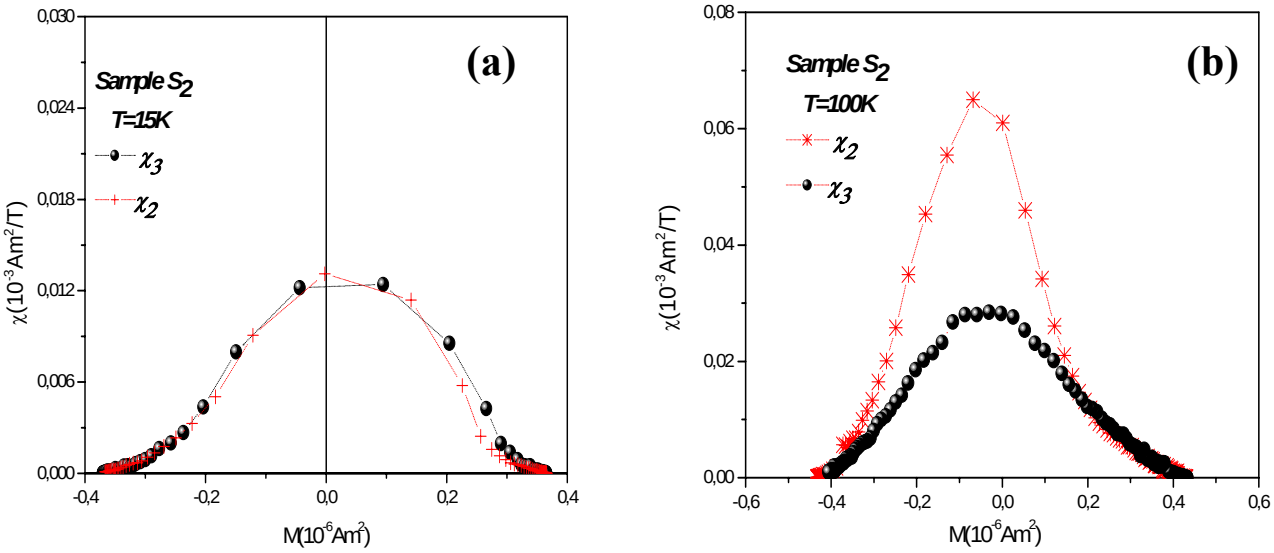

Figure 5.3. (a). *Irreversible susceptibility values versus magnetization for sample S_2 at T=15K.*
(b). *Irreversible susceptibility values versus magnetization for sample S_2 at T=100K.*

In the forthcoming discussion, we will concentrate mostly on the stabilised hysteresis cycles, and thus we will define the exchange bias field H_E and the coercive field H_C as:

$$H_E = \frac{\left|H_1^* + H_2\right|}{2}; \qquad H_C = \frac{\left|H_1^* - H_2\right|}{2}$$

At 15K it is found that $\mu_0 H_E = 0.05T$ and $\mu_0 H_C = 0.070T$.

5.2. Exchange bias field and coercive field as a function of temperature

Following the procedure described in 5.1, the hysteresis cycles were measured on the different samples at different temperatures from 15K to 300K (see Figure 5.4 for sample S_2).

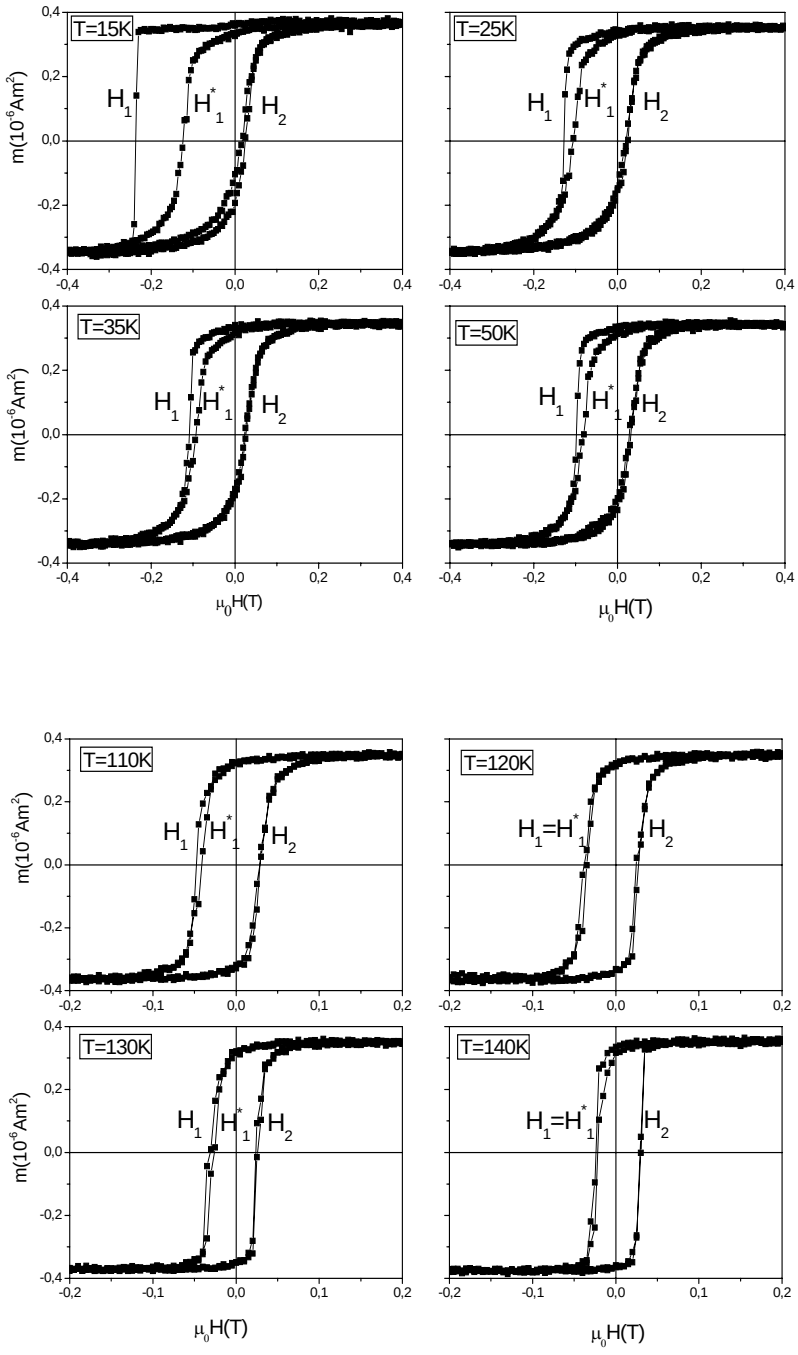

Figure 5.4*. Hysteresis cycles measured at different temperatures on sample S_2.*
(Note that due to the measuring procedures used, the 1st branch of the cycle is not properly measured).

The used measuring sequence was the following: the samples were cooled down from room temperature under an applied field $\mu_0 H$= 4T to the first measurement temperature, T=15K. At this temperature, the hysteresis cycles were measured between $\mu_0 H$= 0.4T and $\mu_0 H$= -0.4T. The following cycles at different temperature values from T= 15K to T= 140K were measured then without another cooling process from room temperature. The temperature dependence of H_1^* and H_2 thus deduced for the three different samples are shown in Figure 5.5. (a), Figure 5.6. (a) and Figure 5.7.(a).By applying this process, the 1st branch of the hysteresis cycle is not really measured. This explains that the temperature dependence of H_1 is not plotted here.

The derived temperature dependence of H_C and H_E are shown in Figure 5.5.(b) for sample S_1, Figure 5.6.(b) for sample S_2 and Figure 5.7.(b) for sample S_3.

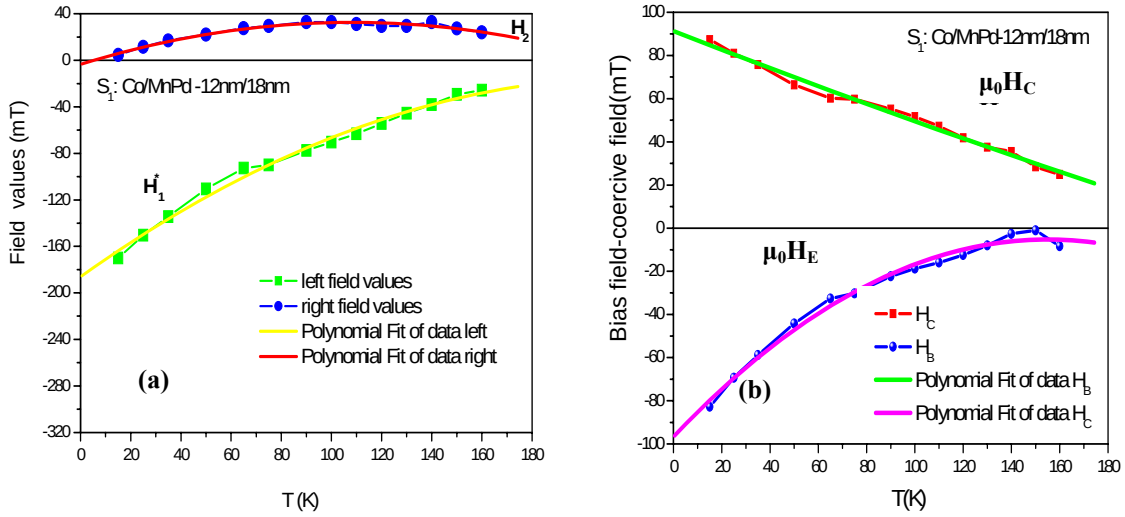

Figure 5.5. (a) *Field values versus temperature for samples S_1.* ***(b)*** *Bias field and coercive field versus temperature for samples S_1.*

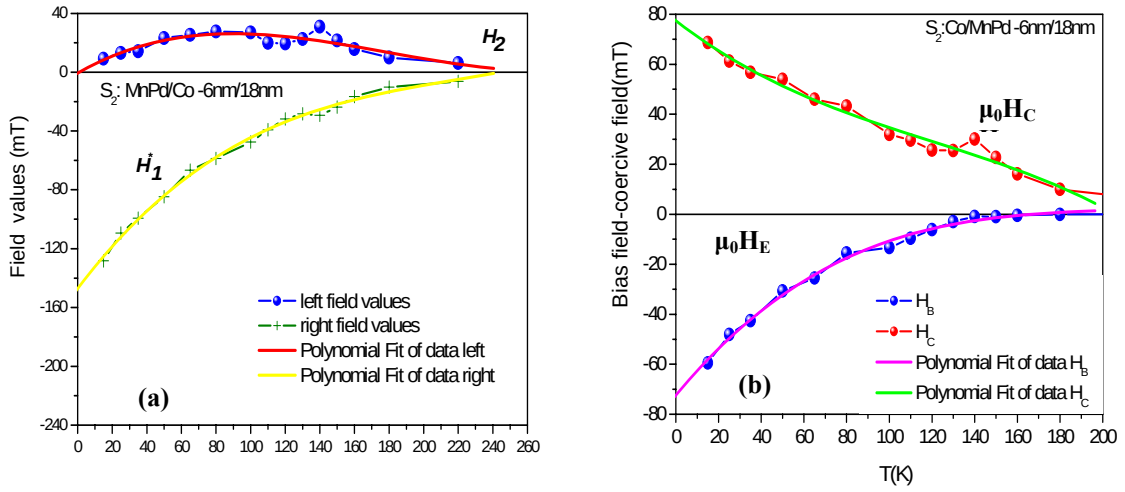

Figure 5.6. (a) *Field values versus temperature for samples S_2.* ***(b)*** *Bias field and coercive field versus temperature for samples S_2.*

Both the exchange bias field and coercive field decrease monotonously as temperature is increased. The exchange bias field H_E vanishes at T≈140K whereas H_C keeps a significant value up to T=240K.

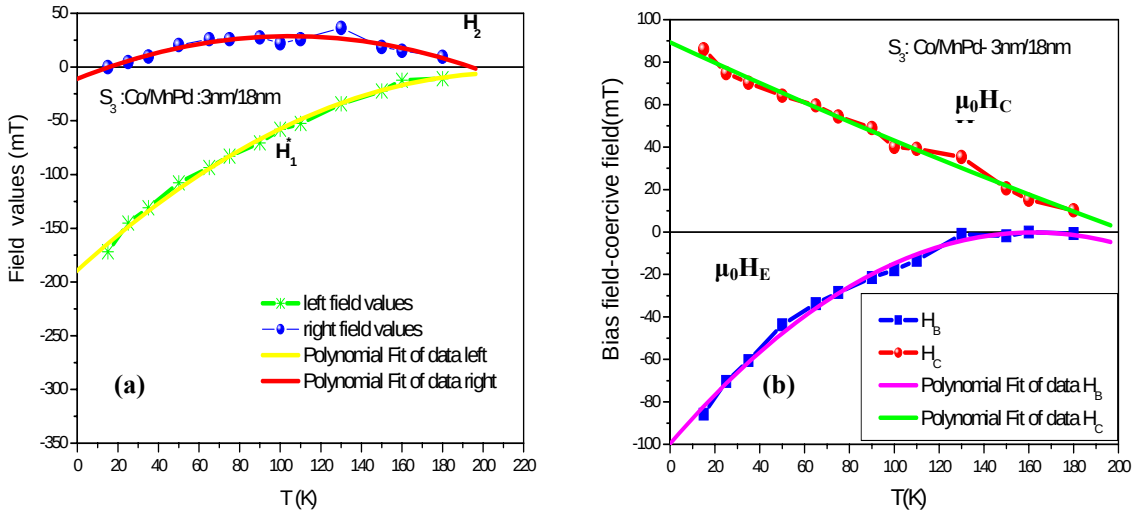

Figure 5.7. (a) *Field values versus temperature for samples S_3.* ***(b)****Bias field and coercive field versus temperature for samples S_3.*

For all studied samples S_1, S_2 and S_3 the value of χ_{max} at H^*_1 and H_2 for T=15K is the same. Both χ'_{1max} and χ'_{2max} increases with temperature. This effect may be related to the decrease in H_C, and thus decrease in ΔH_C, the width of the coercive field distribution, as temperature increases. Further, χ'_{1max} and χ'_{2max} which have equal values at low temperatures tend to differ slightly at higher T ($\chi'_{2max} > \chi'_{1max}$).

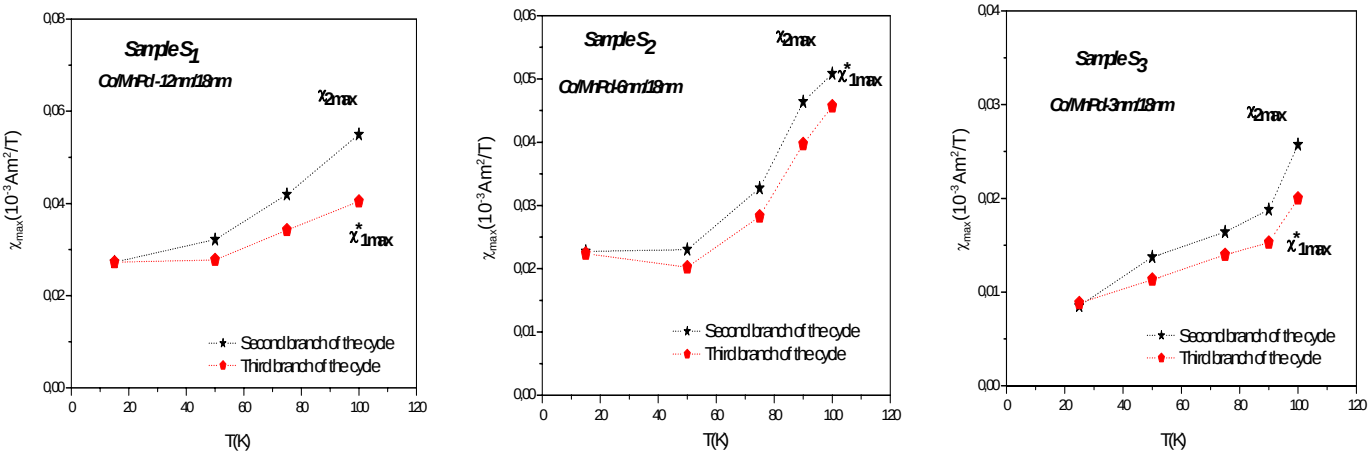

Figure 5.8*. Irreversible susceptibility values versus temperature for sample S_1, S_2 and S_3 along different branches of the hysteresis cycle.*

The coercive field H_C and exchange bias field H_E in the various samples at T=15K are compared in Figure 5.9.These fields have similar values in the different samples. This indicates that, for the thickness range considered, the thickness of the AFM layer has almost no impact on the magnetization behaviour.

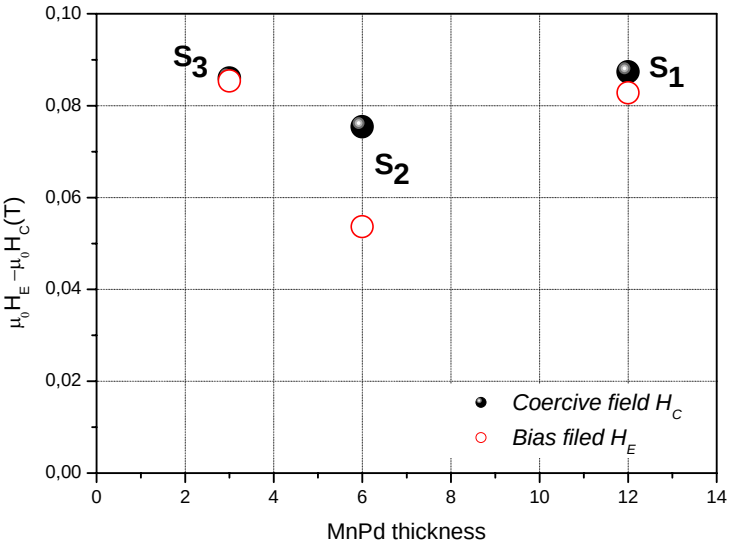

Figure 5.9. *The coercivity and exchange bias field of the three Co/MnPd samples as a function of the MnPd thickness measured at 15 K.*

5.3. Additional measurements of the hysteresis loops in sample S_1 and S_2

The results of the magnetic measurements on the three considered samples are similar. In order to analyse further the observed hysteresis cycles, additional measurements were realised on samples S_1 and S_2.

5.3.1. Hysteresis cycle as a function of the cooling temperature under $\mu_0 H$= 0.4T (sample S_1)

The hysteresis cycles of sample S_1 presented in Figure 5.10 were measured according to the following procedure: the sample was cooled from T=300K to the temperature T_{cool} under $\mu_0 H$= 0T. At T_{cool} the field $\mu_0 H_{cool}$= 0.4T was applied and the sample was further cooled down to T=15K. The hysteresis cycles then measured at T=15K are shown in Figure 5.10.

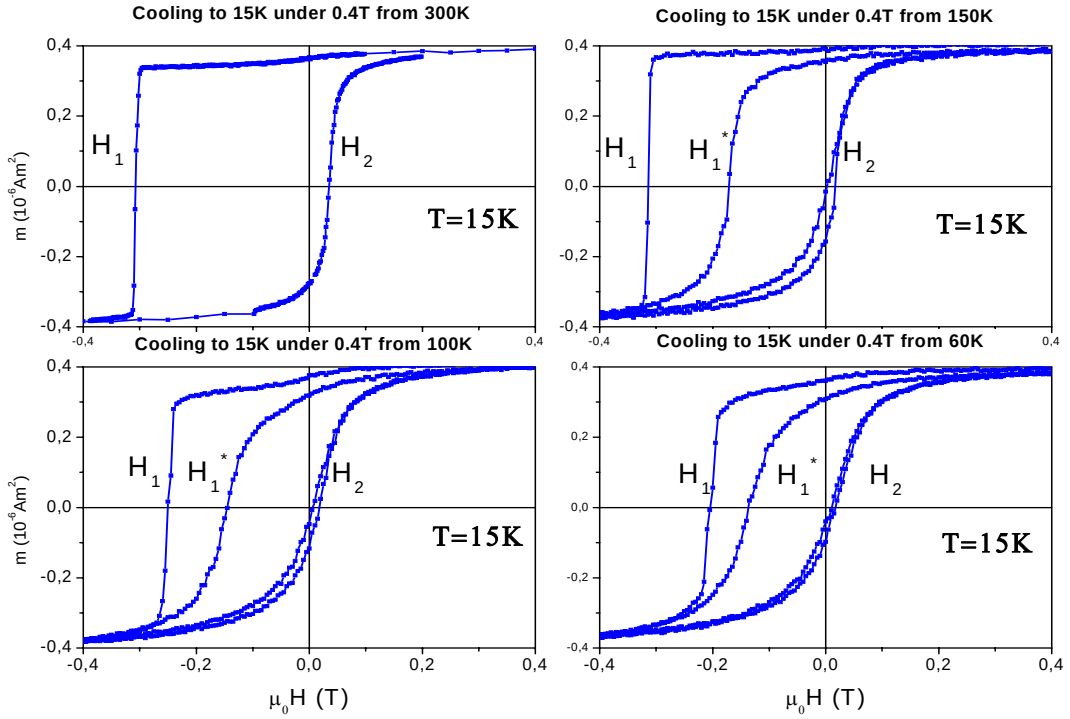

Figure 5.10. *Hysteresis loops of sample S_1 as a function of the cooling temperature.*

The first branch of the hysteresis cycle is significantly dependent on the value of T_{cool}, as illustrated by the T_{cool} dependence of $\mu_0 H_1$ shown in Figure 5.11. By contrast the other branches are little dependent on T_{cool}. Qualitatively this behaviour suggests that the magnetization processes along the first branch depends whether the magnetization of the FM layer is fully saturated or not. By contrast along the other branches such condition is not required (see Figure 5.11).

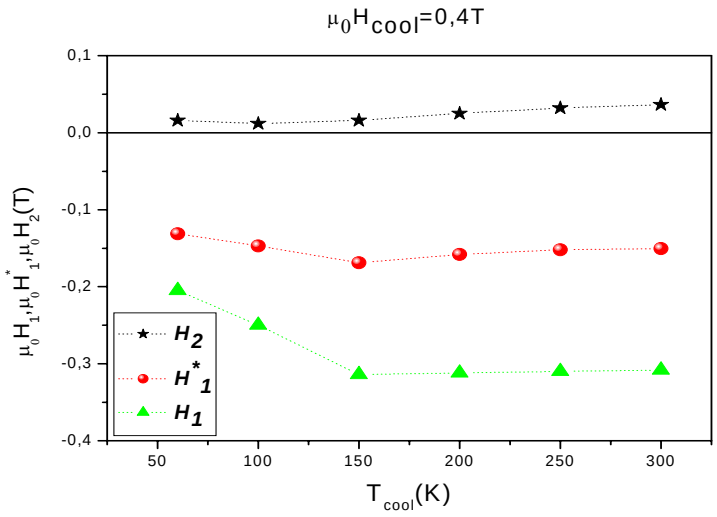

Figure 5.11. *Values of the reversal field as a function of the cooling temperature, under a field of 0.4T.*

5.3.2. Applied field effects

The hysteresis cycle measured in sample S_2 after cooling under $\mu_0 H$ = +5T from T = 300K to T = 120K is plotted in Figure 5.12 as black dots. An original behaviour was found after applying $\mu_0 H$ =-5T. Reversal around H_2 was shifted to higher magnetic fields by approximately $\mu_0 \delta H$ =10mT, whereas the reversal around H^*_1 was not modified. At T=130K the same effect was found but the shift reduced to $\mu_0 \delta H$ =8mT. By contrast, below T=100K no shift of the hysteresis cycle could be detected.

At each temperature, it was found that this field-induced shift disappeared during further measurements of the cycle and normal exchange-bias at this temperature recovered. In other words, first magnetization reversal only is affected by the applied field.

It is expected that the saturation of the FM layer is obtained in relatively low field and thus under $\mu_0 H$ = +5T it is the whole AFM layer magnetization which must be affected primely. It tends to rotate according to the usual spin – flop process. When this happens the exchange coupling between the first AFM layer and the next one is reduced .The magnetization configuration of the first AFM layer (together with that of the FM layer) are stabilised at the expense of the anisotropy energy lost within the AFM layer. This explains qualitatively the observed increase in H_2.

However, the modification of the AFM magnetic configuration induces by the field is highly metastable. It is lost at first reversal of the FM layer and thus the initial cycle is recovered.

In agreement with the present analysis field enhanced coercivity (and bias) was found in Co/NiO by Camarero et al. [4].These authors attributed this phenomenon to the action of the applied field on the whole AFM layer.

However, in their analysis they focused on the uncompensated AFM moment which may exist in a highly disordered antiferromagnet. If this would happen in the present case the bias field measured in low field after applying $\mu_0 H$ =-5T would remain during further measurements.

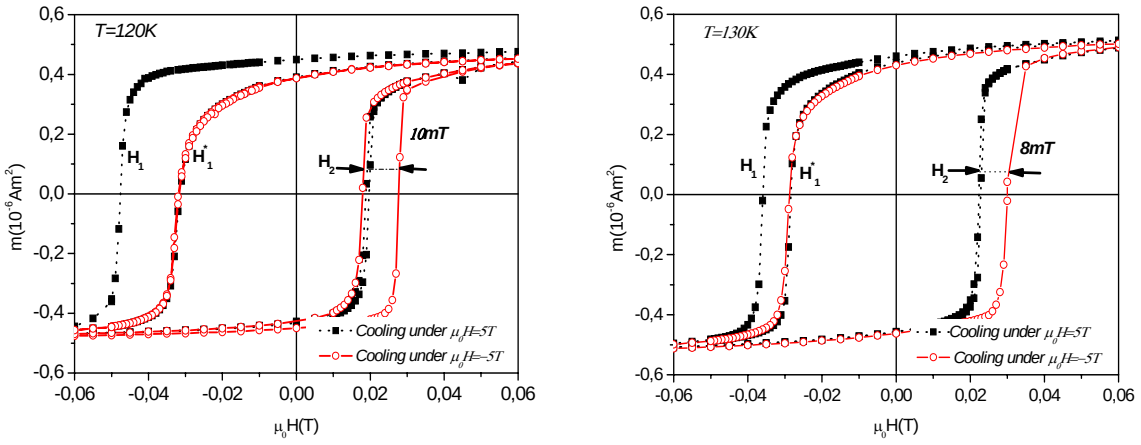

Figure 5.12. *Hysteresis cycles measured at T=120K and T=130K for sample S_2.*

Cooling from T=300K to T=140K, a further striking effect appears during magnetization measurements at T=140K, leading to reduction in the value of H_E. The hysteresis cycle is now shifted along the direction of the applied magnetic field (see Figure 5.13). from $\mu_0 H_E$= -7(1) mT to $\mu_0 H_E$= + 1(1) mT at T=130K. The same behaviour is observed at T=150K, the exchange bias initially equal to $\mu_0 H_E$= -2 (1) mT vanishes after the applying of $\mu_0 H$ =-5T to $\mu_0 H_E$=0mT.

In the spirit of Malozemoff model the exchange bias is due to uncompensated AFM moments which are induced by the applied magnetic field. Close to T_N, the applied field is able to reverse partially these uncompensated moments, thus leading to the observed reduction in H_E.

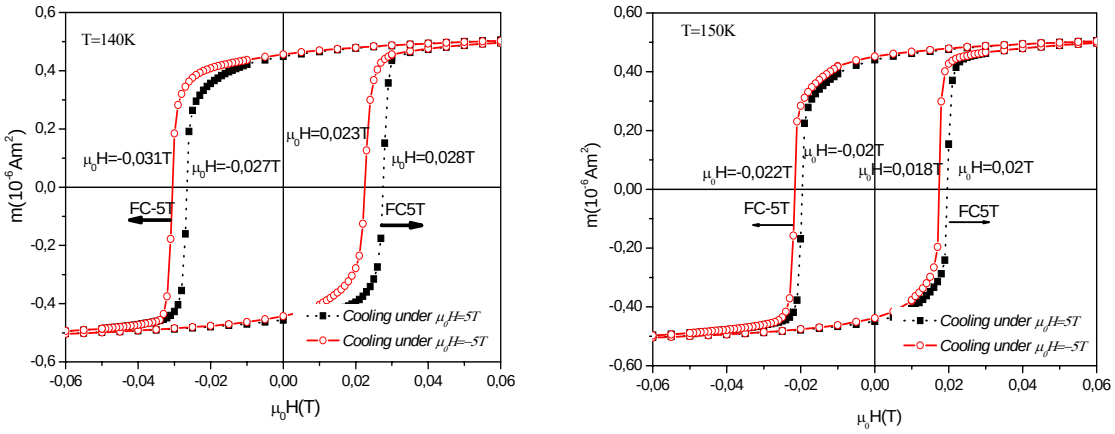

Figure 5.13. *Hysteresis cycles measured at T=130K and T=140K for sample S_2.*
(The superconducting coil remanent field, of the order of 1mT, was subtracted from the data.)

❖ *Note on the Squid magnetometer remanent field value*

The exchange bias field values given in the present section are very small and they may be affected by the remanent field generated by the superconducting coil. In order to establish unambiguously the validity of the measurements, the remanent field value of the coil was measured accurately.

For these measurements, a paramagnetic compound, gadolinium sulphate octahydrate, $Gd_2(SO_4)_3$ *8 H_2O was given to us by G. Fillion (see Figure 5.14).

At the temperature of the measurements the susceptibility is field independent in the considered field range. The field variation of the magnetization was measured at the three temperatures of interest, namely 120K, 130K and 140K. The following field sweeping sequence was used: a field of +5T was initially applied and the magnetization measured from +0.5T to -0.5T and back to +0.5T.

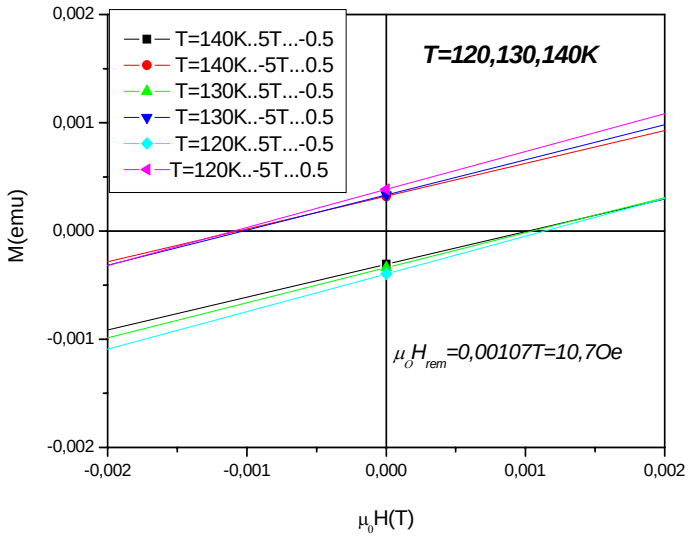

Figure 5.14. *Magnetic moment versus applied field for $Gd_2(SO_4)_3$ *8 H_2O at a given temperature.*

The associated M(H) obtained is shown in Figure 5.14. The coil remanent field for the sequence +5T ,-0.5T and +0.5T was found constant and equal to $\mu_0 H_{rem}$= +0.0011T. For the negative field sequence -5T, +0,5T, -0.5T the same constant value was found $\mu_0 H_{rem}$= -0.0011T. These values were used in order to correct the Squid data discussed in the section above.

5.4. Discussion

5.4.1. Experimental exchange-bias compared to usual models

The exchange bias field and the coercive field found in the Co/MnPd alloys studied in this thesis are larger than most values found in systems which exhibit exchange bias phenomenon (see Table1 Chapter1). The interfacial exchange bias coupling energy $\Delta\sigma = 2\mu_0 M_F t_F H_E$ reaches a value of $\Delta\sigma = 2{,}46\times10^{-3} J/m^2$ at T=15K. In particular, this value is five times higher then typically reported in polycrystalline Co/CoO exchange bias systems. This shows that the thin CoO layer formed at the surface of the samples doesn't significantly affect the bias effect arising from the Co/MnPd interface.

When discussing the exchange bias strength in a given system, it is usual to compare the experimental exchange bias field to the bias field predicted by the Meiklejohn and Bean model. The MB expression for exchange bias, already given in Chapter 1 (relation1.3), may be re-

expressed in terms of the molecular field coefficient $W_{A\text{-}F}$ representing the interfacial coupling

between the ferromagnet FM and the antiferromagnet AFM, as well as of the magnetization M_{FM} of the FM layer and of the magnetization M_{AFM} of each AFM sublattice.

It reads:

$$\mu_{\circ} H_E = \frac{J_{INT}}{t_{FM} M_{FM}} = \frac{\mu_0 W_{A-F} M_{FM} M_{AFM} a_{AFM}}{t_{FM} M_{FM}}$$

where, in the classical molecular field model, $\mu_0 W_{A-F} M_{FM}$, is the molecular field created by the ferromagnetic moments on the antiferromagnetic ones.

For the present numerical calculation, M_{FM} was taken as the Co magnetization: $M_{FM} = 1{,}37\times10^6 A/m$. M_{AFM} was obtained by assuming that the Mn magnetic moment has the same value as in MnPd bulk alloys of similar compositions ($\mu_{Mn} = 4.2\mu_B$) (see [5] and table 1 in Chapter 4) and that the alloy contained 16% of Mn atoms as derived from EDX analysis (see Table 4 in Chapter 4). The Pd magnetic moment was assumed to be zero in agreement with the neutron diffraction study of Kren and Kadar [5]. The AFM sublattice magnetization thus deduced is $M_{AFM} = 0.2\times10^6 A/m$.

The molecular field coefficient $W_{A\text{-}F}$ was derived from the following assumption:

$$W_{A-F} M_{AFM} M_{FM} = \frac{1}{2}\sqrt{W_{A-A'} {M_{AFM}}^2 \times W_{F-F} {M_{FM}}^2}$$ or equivalently :

$$W_{A-F} = \frac{1}{2}\sqrt{W_{A-A'} \times W_{F-F}}$$

$W_{F\text{-}F}$ =2100 was derived from the Curie-Weiss expression: $W_{F-F} = 3N_{Co}k_B T_C / \mu_0 M^2{}_{FF}$ ($N_{Co} = 87 \times 10^{27}\, at/m^3$ - number of the Co atoms per unit volume and the Curie temperature T_C= 1394 K) assuming that the Co moments are classical moments which follow the Langevin function. In the above expression, the coefficient 1/2 expresses the fact that the interfacial FM-AFM involves atoms in a strongly intermixed plane which contains as many atoms of each kind.

The $W_{A\text{-}A'}$ and $W_{A\text{-}A}$ molecular field coefficients were assumed to be equal and applying the molecular field model given by: $W_{A-A'} = \frac{3N_{Mn-Pd}k_B T_N}{2\mu_0 M^2{}_{AFM}}$. $W_{A-A'} = -W_{A-A} = 2345$ ($N_{Mn-Pd} = 69 \times 10^{27}\, at/m^3$-number of "Mn-Pd" atoms of a given sublattice per unit volume) was obtained. $W_{A\text{-}F}$ = 1100 is thus derived.

The calculated bias field reaches:

$$\mu_0 H_E = \frac{4 \times \pi \times 10^{-7} \times 1100 \times 1{,}37 \times 10^6 \times 0{,}2 \times 10^6 \times 0{,}2 \times 10^{-9}}{1{,}37 \times 10^6 \times 18 \times 10^{-9}} = 3T$$

This field is approximately 100 times higher then the experimental bias field ($\mu_0 H_E = 0{,}05T$ (0.11T on the first part of the hysteresis cycle) at T=15K). Such a discrepancy is systematically found in EB systems. It results from the fact that the fully AFM uncompensated interface assumed in the MB model is very unreal to occur in reality. Further, in case it would occur other interfacial magnetic configurations are energetically much more favourable than the antiparallel coupling between interfacial moments.

Beyond the Meiklejohn-Bean model, the interfacial magnetic domain wall assumed in the Mauri's model [6] is the most natural magnetic configuration one may think of for an uncompensated antiferromagnetic layer. Considering that a domain wall constitutes the configuration which permits magnetization reversal at the least energy cost, it provides actually the lowest bias-field for a perfectly coupled, fully uncompensated interface. In this model, the interfacial energy, σ, is equal to the interfacial domain wall energy. Assuming that the wall is confined in the antiferromagnetic layer, $\sigma = \gamma_{AFM} = 4\sqrt{A_{AFM} K_{AFM}}$. The value of the exchange stiffness, $A_{AFM} = 3{,}2 \times 10^{-12}\, J/m$, was derived from the MnPd Néel temperature. In the absence of existing experimental data, the value of the anisotropy coefficient K_{AFM} was taken arbitrarily equal to $5 \times 10^6\, J/m^3$, a relatively large value as it is expected for Pd alloys.

The value of γ derived is: $\gamma_{AFM} = 16 \times 10^{-3}\, J/m^2$. The exchange bias field reaches: $\mu_0 H_E = \frac{\gamma_{AFM}}{2M_{FM} t_{FM}} = 0.32T$ which is already much closer to the experimental bias field, but still significantly too high.

Considering the approximation made in this bias field evaluation, one could argue that the Mauri's model provides a reasonable value to the experimental results. However, it is much more likely that the present model which assumes fully uncompensated interface cannot describe the real process observed. This led us to develop a simple phenomenological model of EB and apply it to the present system.

5.4.2. Phenomenological description of exchange-bias

Of the various models proposed to describe exchange bias, the random field description proposed by Malozemoff [7] permits an uncompensated antiferromagnetic moment to appear in a very natural way on an essentially compensated interface, as a result of the disordered nature of the interface. Unfortunately, Malozemoff assumed a priori that the ferromagnetic magnetization aligned along the uncompensated antiferromagnetic magnetization. As realised by Koon [8], and, after him, by Schulthess and Butler [9], it is most likely that perpendicular coupling should exist between the FM and AFM magnetizations.

Model:

Our own approach to this problem assumes a compensated or weakly uncompensated antiferromagnetic interface, in agreement with the above description. This corresponds to the most general magnetic configuration expected for an antiferromagnetic interface. Only in the case where the interfacial plane is perpendicular to the propagation vector of the antiferromagnetic structure may a large non compensated moment arrangement be expected. Further, for an interface which is uncompensated in principle, many authors have discussed the fact that defects will ultimately lead to the formation of an essentially compensated interface.

We describe the ferromagnetic-antiferromagnetic coupling within classical molecular field formalism. Four terms enter into the expression for the magnetic energy :

$$E_{F-AFM1} = -W_{A-F}\,\mu_0 M_{AFM1} M_{FM} \cos(\theta_{FM} - \theta_{AFM1}) \times a_{AFM} \tag{1}$$

$$E_{F-AFM2} = -W_{A-F}\,\mu_0 M_{AFM2} M_{FM} \cos(\theta_{FM} - \theta_{AFM2}) \times a_{AFM} \tag{2}$$

$$E_A^{\text{int}} = -W_{A-A}^{P}\ \ \mu_0 M_{AFM1} M_{AFM2} \cos(\theta_{AFM1} - \theta_{AFM2}) \times a_{AFM} \tag{3}$$

$$\begin{aligned} E_A^{P-P} &= \mu_0 (0.25 W_{A-A}^{P-P'} M^2{}_{AFM1}\ \cos(\varphi - \theta_{AFM1}) - 0{,}25 W_{A-A}^{P-P'} M^2{}_{AFM2}\ \cos(\varphi - \theta_{AFM2}) \\ &- 0{,}25 W_{A-A'}^{P-P'} M_{AFM1} M_{AFM2}\ \cos(\varphi - \theta_{AFM1}) + 0.25 W_{A-A'}^{P-P'} M_{\ AFM1} M_{AFM2}\ \cos(\theta_{AFM2} - \varphi)) a_{AFM} \end{aligned} \tag{4}$$

Expression (1) and (2) represent the coupling between the FM magnetization and the magnetization on each AFM sublattice and expression (3) represents the coupling within the interfacial AFM layer. The last term (4) represents the coupling between the interfacial AFM layer and the second AFM layer resulting from the possible canting of the interfacial AFM layer.

In these expressions, M_{FM} is the ferromagnetic magnetization, M_{AFM1} and M_{AFM2} are the antiferromagnetic magnetizations of the 1st and 2nd sublattice respectively. θ_{FM}, θ_{AFM1} and θ_{AFM2} are the associated angles measured with respect to the reference axis z (see Figure 5.15 below). φ represents the direction of the AFM easy axis. In our calculation, $\varphi = 90°$ was assumed, which does not affect the generality of the analysis.

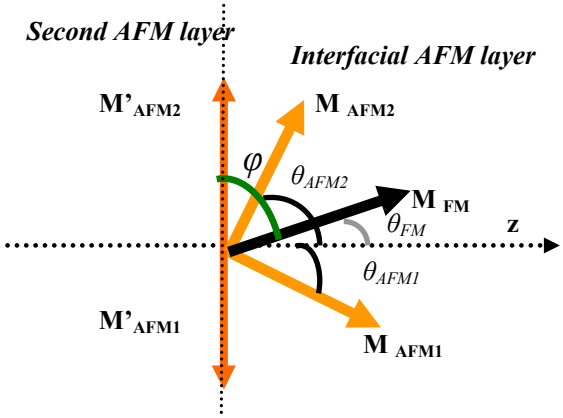

Figure 5.15. *Schematic view of the angle notation used in the model. M_{FM} is the ferromagnetic moment, M_{AFM1} and M_{AFM2} are the AFM moments in the interfacial AFM layer, M'_{AFM1} and M'_{AFM2} are the moments in the next AFM layer.*

The molecular field coefficient $W^{P}_{A-A'}$ represents the in-plane interactions in the AFM plane (see below). For a stacking of fcc plane along the direction (111) there are 6 neighbours in-plane, 3 above and 3 below thus, $W^{P}_{A-A'} = 0.5W_{A-A'}$ was assumed.

In expression (4) the coefficient 0.25 corresponds to the product of two terms, both equal to 0.5. The first of these terms comes from the fact that the energy terms representing the exchange energy within the 1st AFM sublattice and within the second AFM sublattice are separated in (4) whereas they are grouped in expression (3). The second term 0.5 comes from the fact that the molecular field coefficients between antiferromagnetic planes $W^{P-P'}_{A-A}$ and $W^{P-P'}_{A-A'}$ were assumed to amount to half the in-plane molecular field coefficient, W^{P}_{A-A} and W^{P}_{A-A}' (this is based on the same type of hypothesis as used to determine $W_{A\text{-}A}$).

The minimum energy configuration was then obtained for $W_{A\text{-}F}$ varying from zero to the value evaluated above ($W_{A\text{-}F} = 1100$) taken as a maximum.

Evidence for large canted AFM configurations

Let us consider first, the fully compensated case, $M_{AFM1} = M_{AFM2}$. Obviously the AFM moment configuration is canted symmetrically with respect to the FM moment direction (see Figure 5.16 (a)).

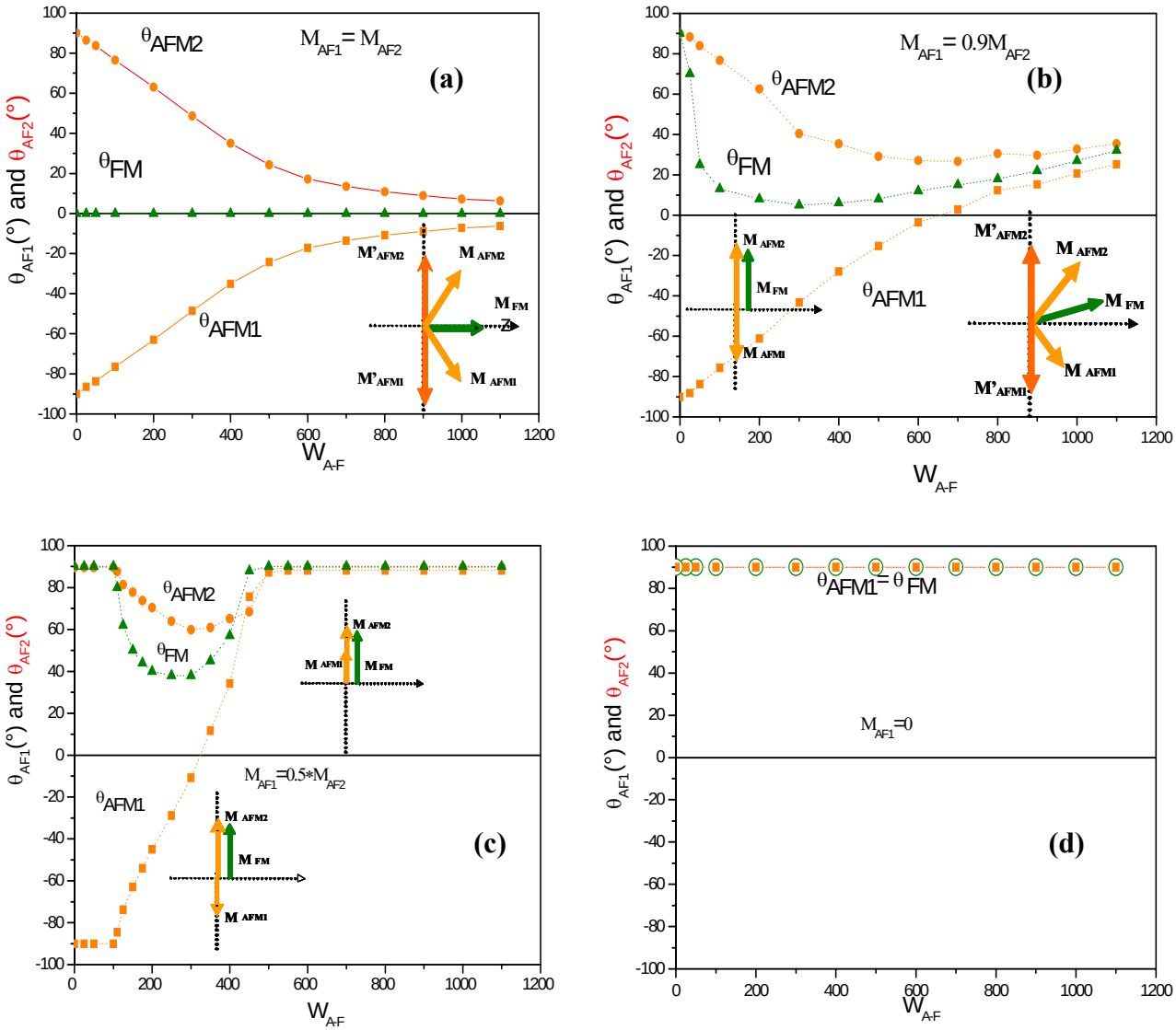

Figure 5.16. *Calculated values for θ_{FM}, θ_{AFM1}, θ_{AFM2} representing the various possible configurations :(a) fully compensated case $M_{AFM1} = M_{AFM2}$ and different uncompensated situations ((b) $M_{AFM1} = 0.9M_{AFM2}$,(c) $M_{AFM1} = 0.5M_{AFM2}$,(d) $M_{AFM1} = 0$)*

As $W_{A\text{-}F}$ increases from 0 to the maximum value, the canting angle closes progressively. It is striking that for $W_{A\text{-}F} \approx 1000$ the canting angle is already below 10°. The interface FM-AFM coupling forces quasi-alignment of the moments in the interfacial AFM layer. This result was unexpected since most calculations in the literature conclude to a weak interfacial canting angle. Yet, in our calculation, the values of the exchange interactions correspond typically to those usually assumed.

In most exchange-bias systems, the interfacial AFM layer is assumed to be at least partially uncompensated and we have thus calculated the minimum energy configuration for various uncompensated situations. The results are shown in Figure 5.16 (b) to 5.16 (d).

Let us consider the case $M_{AFM1} = 0.9 M_{AFM2}$ which corresponds to realistic uncompensation (see chapter 1 section 1.4.3 and the next section in this chapter) (Figure 5.16 (b)). For very small $W_{A\text{-}F}$ values, the ferromagnetic moments are almost aligned along the uncompensated moment, $M_{AFM2} - M_{AFM1}$. This corresponds to the usual exchange bias picture. However, as soon as $W_{A-F} \geq 100$, strong canting is present. Note that due to uncompensation, the angles θ_{AFM1} and θ_{AFM2} are not equal anymore.

For strong uncompensation (Figure 5.16 (c)), the classical exchange bias picture is recovered but as noted already, such uncompensation is very unlikely to appear

Exchange-bias

These observations of strong interface canting may have substantial implication for our understanding of exchange-bias. Indeed, the coupling between the interfacial antiferromagnetic layer and the second layer may be strongly reduced as a result of canting. A convincing way to realise this is to assume full alignment of the interfacial AFM moments along the FM moments. In the case where $W_{A\text{-}A} = -W_{A\text{-}A'}$, relations (1) to (4) above show that the two layers become fully decoupled.

In the general case where the AFM moments are not fully aligned, along the FM ones, and $|W_{A\text{-}A}|$ and $|W_{A\text{-}A'}|$ are not equal, a certain coupling remains between the two AFM layers.

However, it is expected to be much less than between the FM layer and the interfacial AFM layer. Thus exchange bias should be essentially governed by the coupling between the two AFM layers rather than by the coupling between the FM and the AFM interfacial layers.

More generally, Schulthess and Butler [9] already noted that uncompensation is required to give rise to exchange bias. In view of evaluating the strength of the bias field, we need to evaluate realistically the uncompensated AFM moment. Our approach is based on Malozemoff's model [7] that the AFM layer decomposes into domains of which size is of the order of the AFM wall thickness. From the values of A_{AFM} and K_{AFM} assumed above, $\delta = \pi\sqrt{A_{AFM} / K_{AFM}} \approx 3$ nm is obtained. The associated surface area contains around 200 atoms. We consider further that mixing between atoms occurs at the FM-AFM interface. The largest uncompensation is expected in a plane in which half the AFM atoms are replaced by FM ones. From statistics, the unbalance in the occupation of the two AFM sublattices by FM atoms is of the order of $\sqrt{100}$ =10 and the derived uncompensated AFM moments is of the order of 10%.

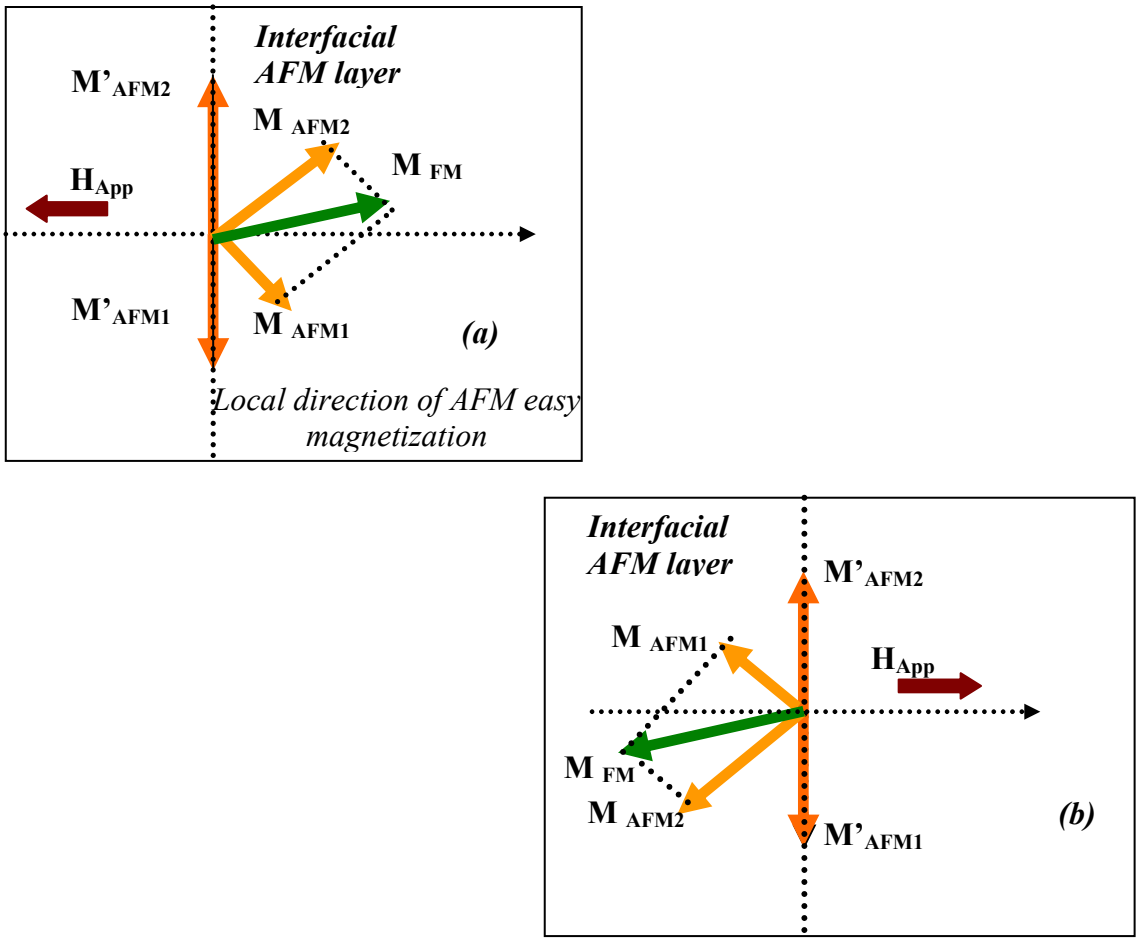

Figure 5.17*. Scheme of the spin configuration in an uncompensated layer in order to obtain bias field (a) favoured orientation; (b) obtained after reversal- unfavoured orientation.* M_{AFM1} *and* M_{AFM2} *refers to the moments in the interface layer whereas* M'_{AFM1} *and* M'_{AFM2} *refers to the moments in the second AFM layer.*

In the spirit of the present model, EB results from the coupling of this uncompensated interfacial AFM moment with the AFM moments in the second layer. For each $W_{A\text{-}F}$ values the exchange bias field value was then calculated by comparing the interfacial coupling energy for two different configurations:

(i) the configuration for minimum energy calculated in the previous section

(ii) the configuration of minimum energy with the constraint that the FM moment is reversed 180° with respect to the configuration (i).

The bias field as a function of $W_{A\text{-}F}$ is plotted in Figure 5.18.

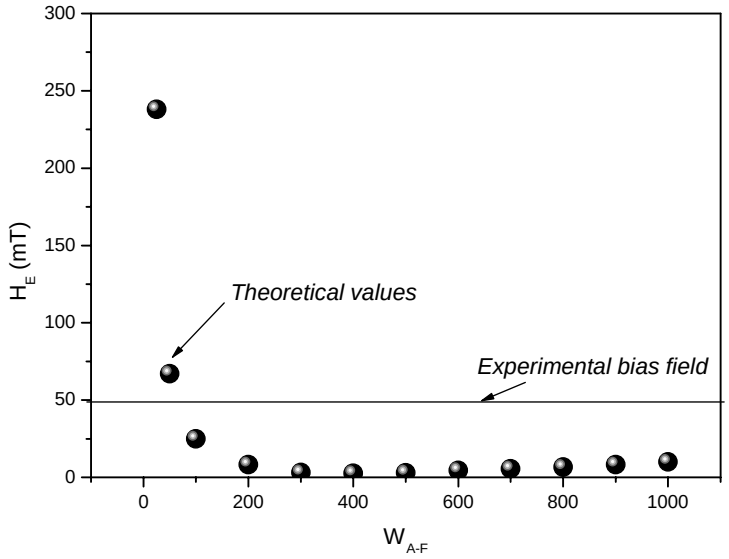

Figure 5.18. *Bias field versus molecular field coefficient* $W_{A\text{-}F}$.

The calculated bias field matches the experimental one for $W_{A\text{-}F} \approx 50$ which corresponds to very weak coupling. At larger $W_{A\text{-}F}$ values the very small value of the bias field is a direct consequence of the decoupling explained above.

Concluding this section, the model provides a simple and realistic picture for exchange-bias coupling, in the present system and possibly more generally. It may permit as well to understand the bias-field reduction found, between 150 K and 170 K, in the vicinity of the blocking temperature. The applied magnetic field tends to force a spin-flop configuration of the antiferromagnet, of which major axis (the angle bisector between the two moment directions) is aligned with its own direction. As we mentioned already, the bias field is zero for such a symmetrical configuration.

Coercivity

In the above analysis, the interfacial antiferromagnetic moments were assumed to follow the ferromagnetic moments during magnetization reversal. As compared to reversal of a simple ferromagnetic layer we may expect some coercivity increase due to the fact that the antiferromagnetic layer has substantial anisotropy. In the previous section, we have arbitrarily assumed that the second order anisotropy constant of MnPd amounts to $K_{AFM} = 5 \times 10^6 J/m^3$. Assuming that the AFM moment rotates trough their difficult magnetization direction, the associated coercive field for coherent rotation amounts to:

$$\mu_0 H_C = \frac{2K_{AFM} \times a_{AFM}}{M_{FM} t_{FM}} \quad (5)$$

This gives $\mu_0 H_C$ = 0.081 T to be compared to the experimental value 0.07 T. This agreement may indicate that magnetization reversal occurs by coherent rotation. Considering the non verified assumptions made in the analysis, it should be considered with great care and be largely fortuitous.

An original phenomenon found in Co/MnPd is the fact that a sufficiently large applied magnetic field may affect the magnetization reversal processes. We have attributed this to an increase in the coercive field of the ferromagnetic layer, which is active on first reversal only. J. Camarero et al. [4] have observed a similar coercive field enhancement in Co/NiO, and showed, by XMCD studies, that it was due to the modification of the NiO uncompensated magnetization. The increased coercive field in Co/MnPd requires the application of a large applied magnetic field, of the order of 5T. For such field strength, the Co ferromagnetic magnetization is expected to be fully saturated. It is thus natural to attribute this to a rearrangement of the interfacial AFM moment configuration, as it is the case in Co/NiO. Note that the subsequent hysteresis cycles are not modified, which implies that the modified interfacial antiferromagnetic rearrangement does not survive on subsequent hysteresis cycles.

References-Chapter 5

[1] M.R.FITZSIMMONS, P.YASHER, C.LEIGHTON, I.K.SCHULLER, *Asymmetric Magnetization Reversal in Exchange-Biased Hysteresis Loops,* Phys. Rev. Lett .vol.84, p3986 (2000).

[2] K.LIU, S.M.BAKER, M.TUOMINEM, *Tailoring exchange bias with magnetic nanostructures,* Phys. Rev.B, vol.63, p060403 (2001).

[3] I.N.KRIVOROTOV, C.LEIGHTON, J.NOGUES, I.K.SCHULLER, *Relation between exchange anisotropy and magnetization reversal asymmetry in Fe/MnF_2 bilayers,* Phys. Rev. B, vol.65, p100402 (2003).

[4] J.CAMARERO, Y.PENNEC, J.VOGEL, S.PIZZINI, *Field dependent exchange coupling in NiO/Co bilayers,* Phys. Rev. B, vol.67, p020413 (2003).

[5] E.KREAN, G.KADAR, *Crystal and magnetic structures in the Mn-Pd system near $MnPd_3$* , Phys. Lett. vol. 29A, p340 (1969).

[6] D.MAURI, H.C.SIEGMANN, P.S.BAGUS, E.KAY, *Simple model for thin ferromagnetic films exchange coupled to an antifferomagnetic substrate,* J. Appl. Phys. vol.62, p3047 (1987).

[7] A.P.MALOZEMOFF, *Mechanisms of exchange anisotropy,* J.Appl.Phys, vol.63, p3874 (1988).

[8] N.C.KOON, *Calculations of Exchange Bias in Thin Films with Ferromagnetic/ Antiferromagnetic Interfaces* , Phys. Rev. Lett. vol.78,p4865 (1997).

[9] T.C.SCHULTHESS, W.H.BUTLER, *Consequences of Spin-Flop Coupling in Exchange Biased Films,* Phys.Rev. Lett. vol.81, p4516 (1998).

Chapter 6

Magnetic after effect measurements

As discussed in Chapter 2, it is well known that in systems where irreversible magnetization processes occur, time dependent effects are found as well. In this Chapter, time dependent measurements realised on the Co/MnPd samples S_1 and S_2 will be presented.

6.1. Time dependent measurements in sample S_1 and S_2

The time dependence of the magnetization on samples S_1 and S_2 was measured at different temperatures between 15K and 120K in all the temperature range where significant exchange bias exists. The measurements were performed on the different branches of the hysteresis cycle. Their aim was to determine whether different reversal mechanisms are involved on different branches of the cycle as it is often suggested for exchange biased systems (see section 5.1).

6.1.1 Time dependent effects on the 1st branch of the hysteresis cycle in sample S_1.

The magnetic after effect measurements were performed by cooling the system from room temperature under an applied field of typically 5T to the desired temperature value and field value. Then the magnetization was measured during a time duration t=1800s. The field values applied during the measurements were just before the knee occurring in the second quadrant of the hysteresis cycle. This is illustrated in Figure 6.1 for sample S_1 at T=50K. The field at which the knee occurs is $\mu_0 H$= -0,21T (measured in the VSM point by point mode at a field variation rate of 0,002T/s), and the field values selected for magnetic after effect measurements were: $\mu_0 H$= -0,19T, $\mu_0 H$= -0,20T and $\mu_0 H$= -0,21T respectively.

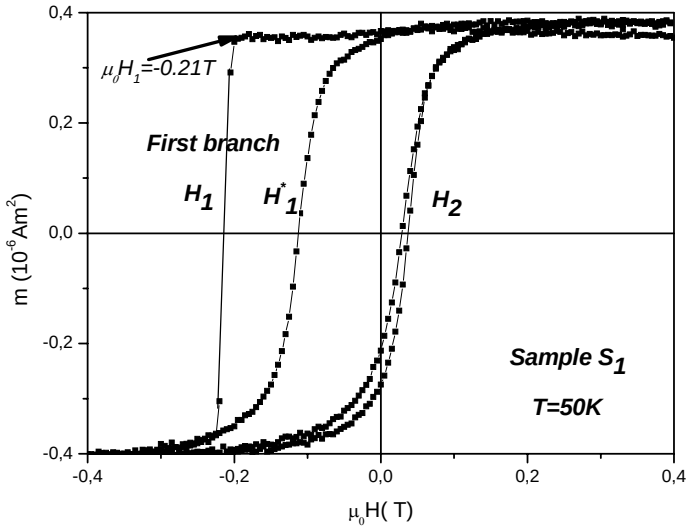

Figure 6.1. *Hysteresis cycle measured at T=50K for sample S_1 showing the knee at $\mu_0 H$=-0,21T on the first branch of the hysteresis cycle .*

The time dependence of the magnetization thus obtained is shown in Figure 6.2, for time t up to 500s corresponding to the time window in which the most significant part of the magnetization variation takes place. Under $\mu_0 H$= -0,19T, the time dependence of the magnetization is very weak. By contrast, under $\mu_0 H$= -0,20T the magnetization evolves from M= 0, $36*10^{-6}$ Am^2 to M= $-0{,}36*10^{-6} Am^2$ after t=1800s. Finally, for $\mu_0 H$= -0,21T, the magnetization evolves from M ≈ 0, $36*10^{-6} Am^2$ at t=0 to M≈ $-0{,}38*10^{-6} Am^2$ already reached at t ≈ 100s.

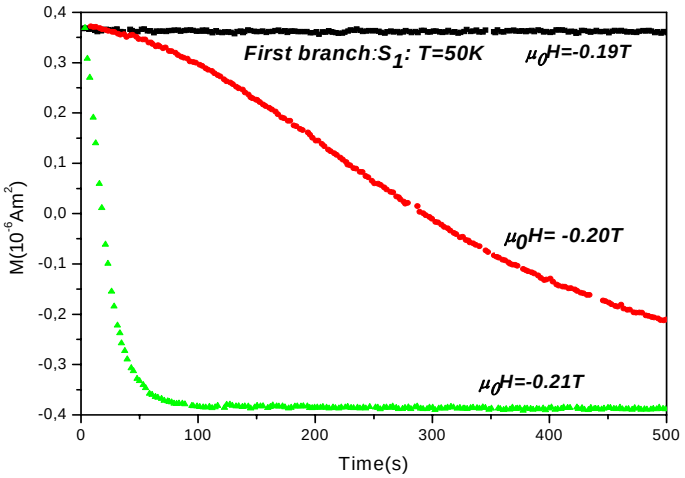

Figure 6.2*.Variation of magnetization versus time at T=50K for sample S_1.*

Following Fatuzzo [1] and Labrune *et al.* [2], the parameter b (t) is introduced such that:

$$b(t) = \frac{M(t) + M_S}{2M_S} \tag{6.1}$$

The various b(t) obtained at a given temperature (Figure 6.3 a for T=50K) were plotted as a function of $t_R=t/t_{50}$ where t_{50} is the time at which M=0. By this process it was found that the various $b(t_R)$ curves at a given temperature merge into a unique curve (Figure 6.3 b for T=50K and Figure 6.4 a, b, c for T=75K,T=100k and T=120K).

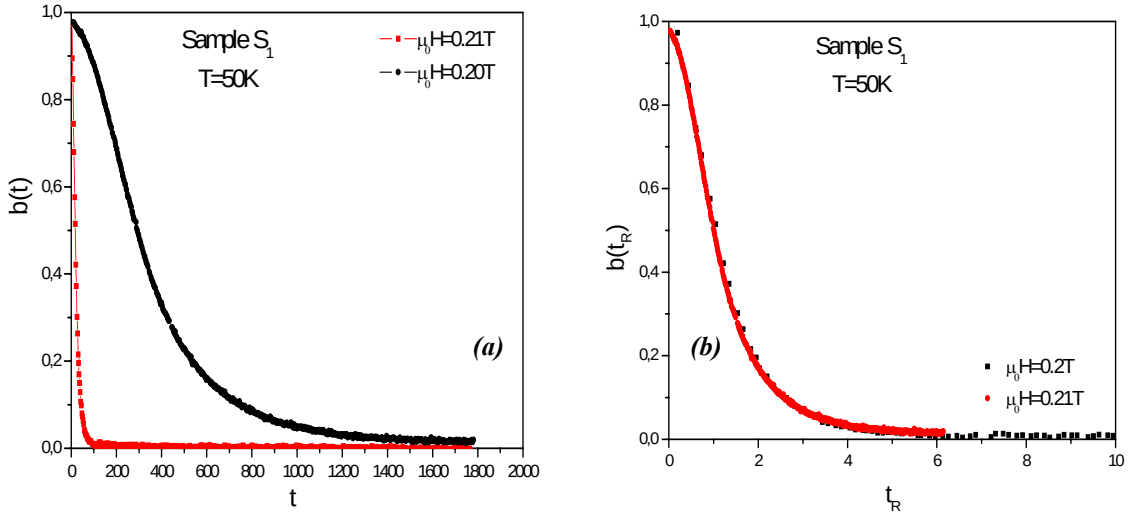

Figure 6.3. *(a) Normalized experimental curves b(t) versus t obtained for different field values. (b) Normalized experimental curves $b(t_R)$ versus t_R obtained for different field values.*

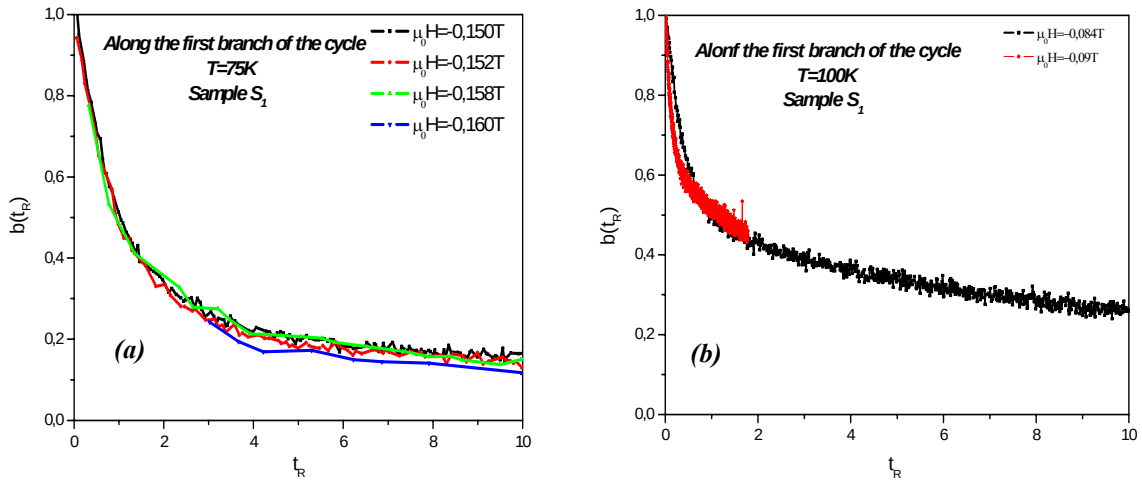

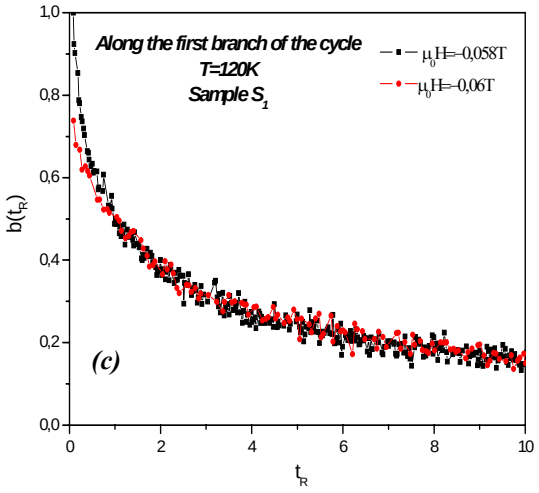

Figure 6.4. *Normalized experimental curves obtained for different field values and temperature values up to T=120K for sample S_1.*

These behaviors are of the features expected within the Fatuzzo-Labrune model [2].

Indeed b (t) is expressed as (see Chapter 2 relation (2.21)):

$$b(t) = \exp(-2k^2(1 - Rt + k^{-1}) + \frac{1}{2}(Rt + k^{-1})^2 - e^{-Rt}(1 - k^{-2}) - \frac{1}{2}k^{-2}(1 - Rt)) \qquad (6.2)$$

(b(t) depends on two free parameters, R(=1/τ) which is the probability rate for nucleation and k=v/Rr$_0$ the parameter related to propagation, with r$_0$ being the nucleus initial radius and v the wall velocity).

Considering that $t = t_R t_{50}$, b(t) may be reexpressed as b(t$_R$):

$$b(t_R) = \exp(-2k^2(1 - Rt_R t_{50} + k^{-1}) + \frac{1}{2}(Rt_R t_{50} + k^{-1})^2 - e^{-Rt_R t_{50}}(1 - k^{-2}) - \frac{1}{2}k^{-2}(1 - Rt_R t_{50})) \qquad (6.3)$$

Since R (=1/τ) and t$_{50}$ is proportional to τ, the factor Rt$_{50}$ is expected to be a constant under the condition that a unique energy barrier is considered. If k is a constant as well which implies that propagation is governed by a unique mechanism, b(t$_R$) at a given temperature appears to be a unique function, as observed experimentally.

Fitting experimental data, we obtained the best agreement in all cases for k ≈ 0, which corresponds to pure nucleation (see Chapter 2, page 37). Accordingly Rt$_{50}$ is in the range 0, 7 to 1 close to the value, Ln2, expected for pure nucleation (see Figure 6.5). As shown in Figure 6.5, the agreement between experimental and calculated time dependence of the magnetization is very satisfactory at all temperatures.

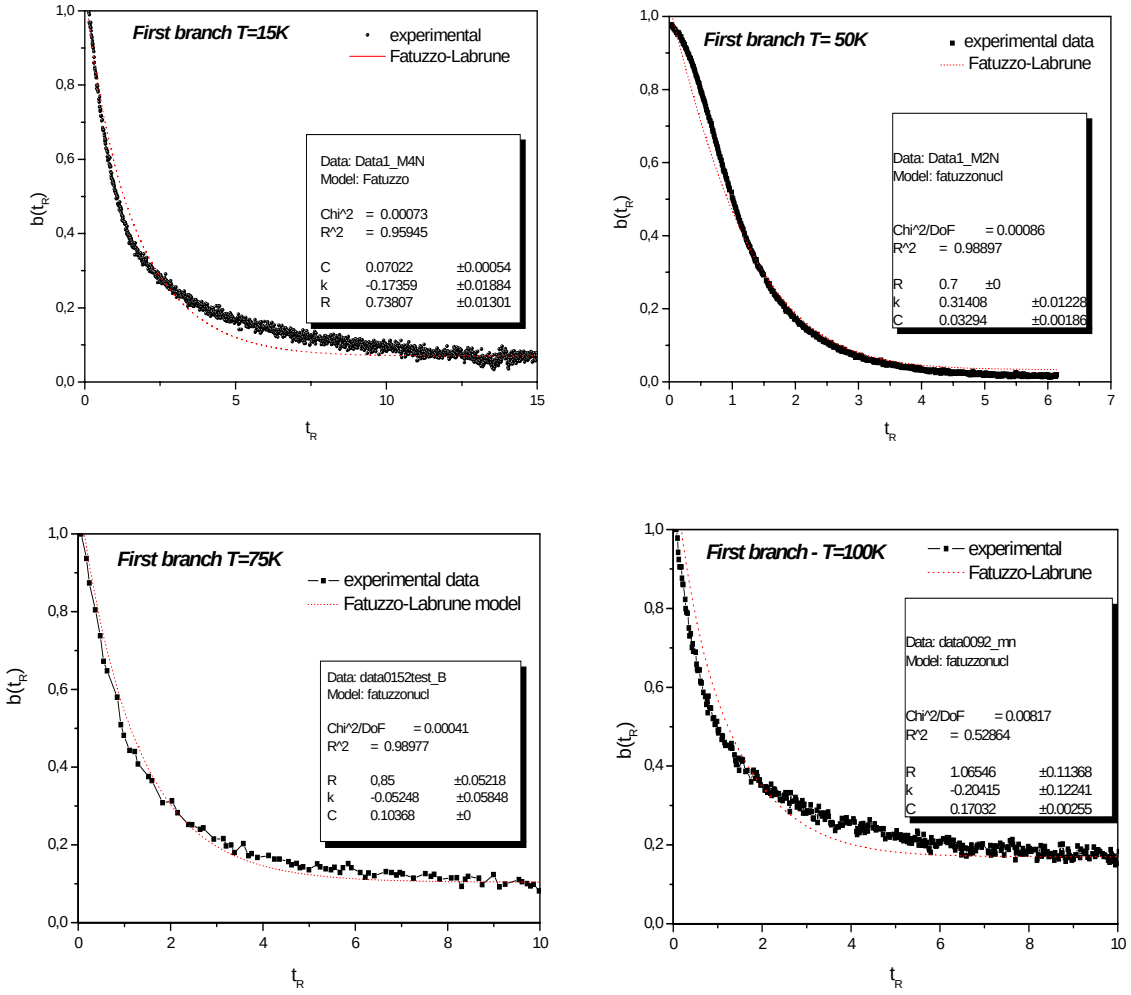

Figure 6.5. *Experimental curve versus calculated curves obtained with the Fatuzzo-Labrune's model for the first branch of the hysteresis cycle in sample* S_1.

6.1.2. Thermal activation on the 2nd and 3rd branches of the hysteresis cycle

To analyze time dependent effects on the second and further branches of the hysteresis cycle the same type of measurements, as on the first branch, were performed. The sample was cooled under $\mu_0 H$= 5T from room temperature to the desired measurement temperature. At this temperature, a hysteresis cycle was measured to determine accurately the measurement field values distributed on both sides of the coercive field (see Figure 6.6).

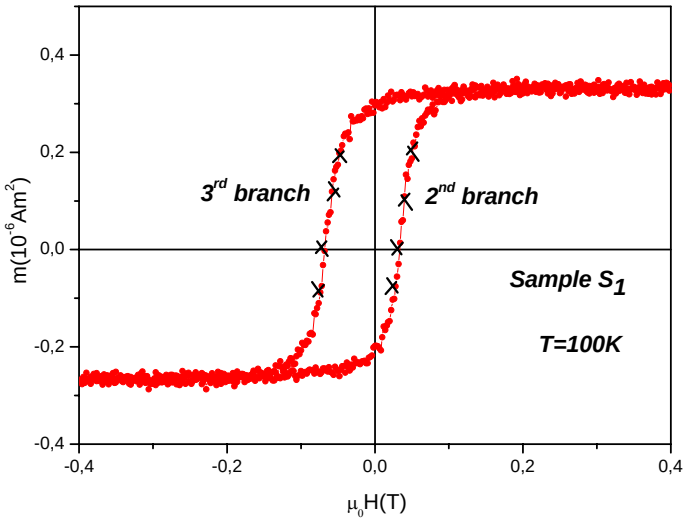

Figure 6.6. *Hysteresis cycle measured at T=100K for sample S_1 (the fields at which magnetic after effect was measured are indicated by crosses).*

At each field value thus determined, the time dependence of the magnetization was measured during t= 6000s (the measurement duration was larger than t=1800s as for the first branch due to the fact that the magnetization relaxation is reduced - see Figure 6.7. for sample S_1 at T=100K).

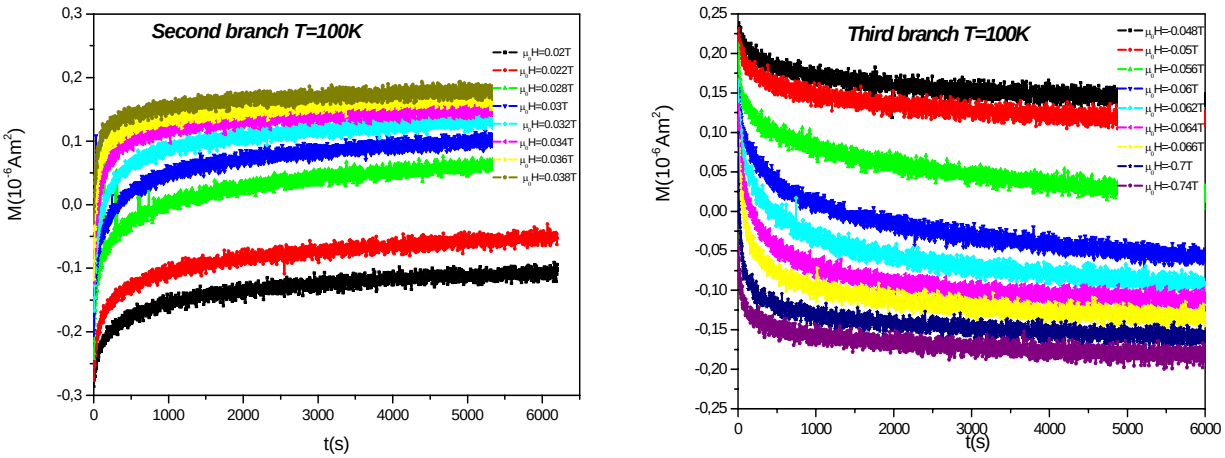

Figure 6.7. *Variation of magnetization function of time in sample S_1 on the second and third branch of the hysteresis cycle at T=100K.*

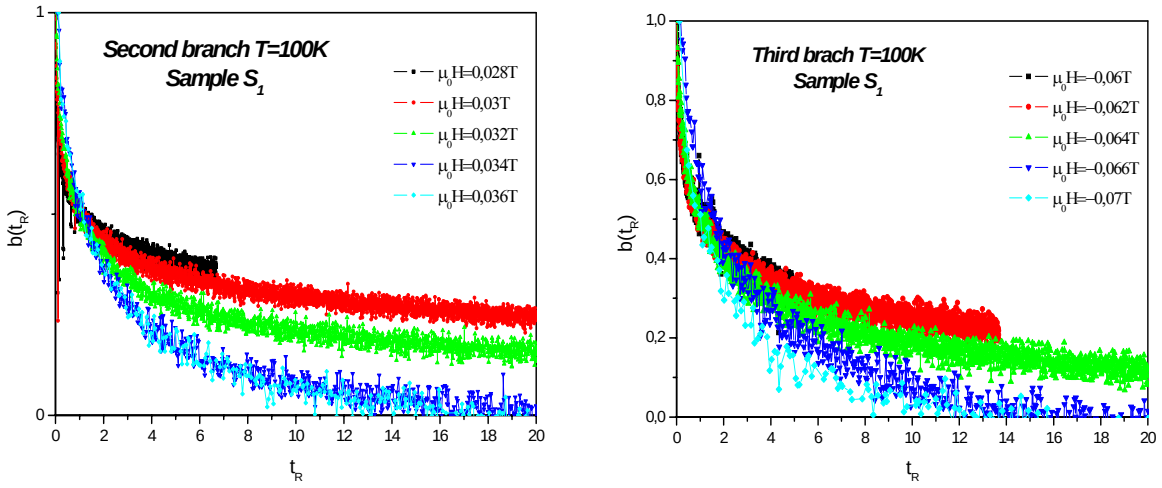

Figure 6.8. *Normalized experimental data for the2nd and 3rd branch of the hysteresis cycle at T=100K in sample S_1.*

From these M(t) curves, $b(t_R)$ curves were deduced following the same procedure as in the above section (see Figure 6.8). In this case, it appeared that neither on the second branch, nor on the third one, do the $b(t_R)$ curves merge into a unique curve. From the discussion presented in the above section, such a result implies that a certain distribution barriers is involved, either in the nucleation process or in the propagation one. Thus, we are led to tempt analyzing the data within the formalism described in section 2.2.2 from Chapter 2, for a distribution of barriers.

Following the usual procedure under such circumstances, the variation of magnetization as a function of *Lnt* is shown in Figure 6.9 for sample S_2 at T=25K and T=100K.

Compared to usual hard magnets, we note that the time dependence of the magnetization is very large and that, the Lnt dependence of magnetization is far from linear in particular at high temperatures. This means that the magnetic viscosity S is not a constant.

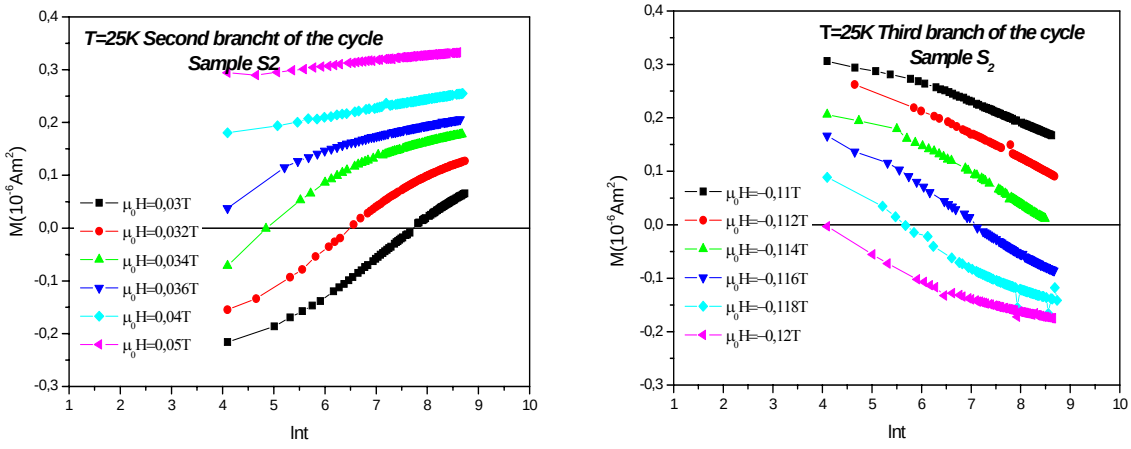

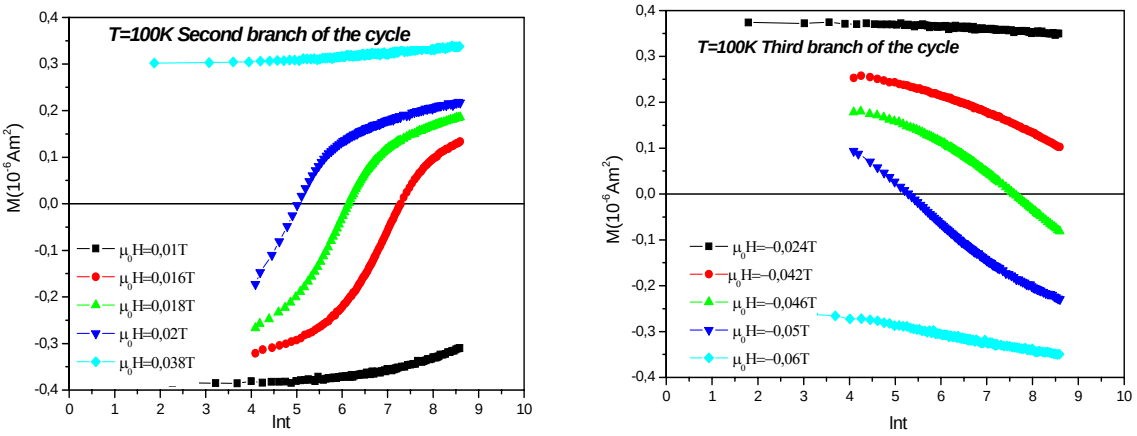

Figure 6.9. *Magnetization dependence versus lnt for sample S_2 at T=25K and T=100K on the 2nd and 3rd branch of the hysteresis cycle.*

From such M(lnt) curves, the magnetic viscosity S was derived at each magnetization values. The curves S(M) thus obtained at T=25K and T=100K are plotted in Figure 6.10 for sample S_2 along the 2nd and 3rd branch of the hysteresis cycle.

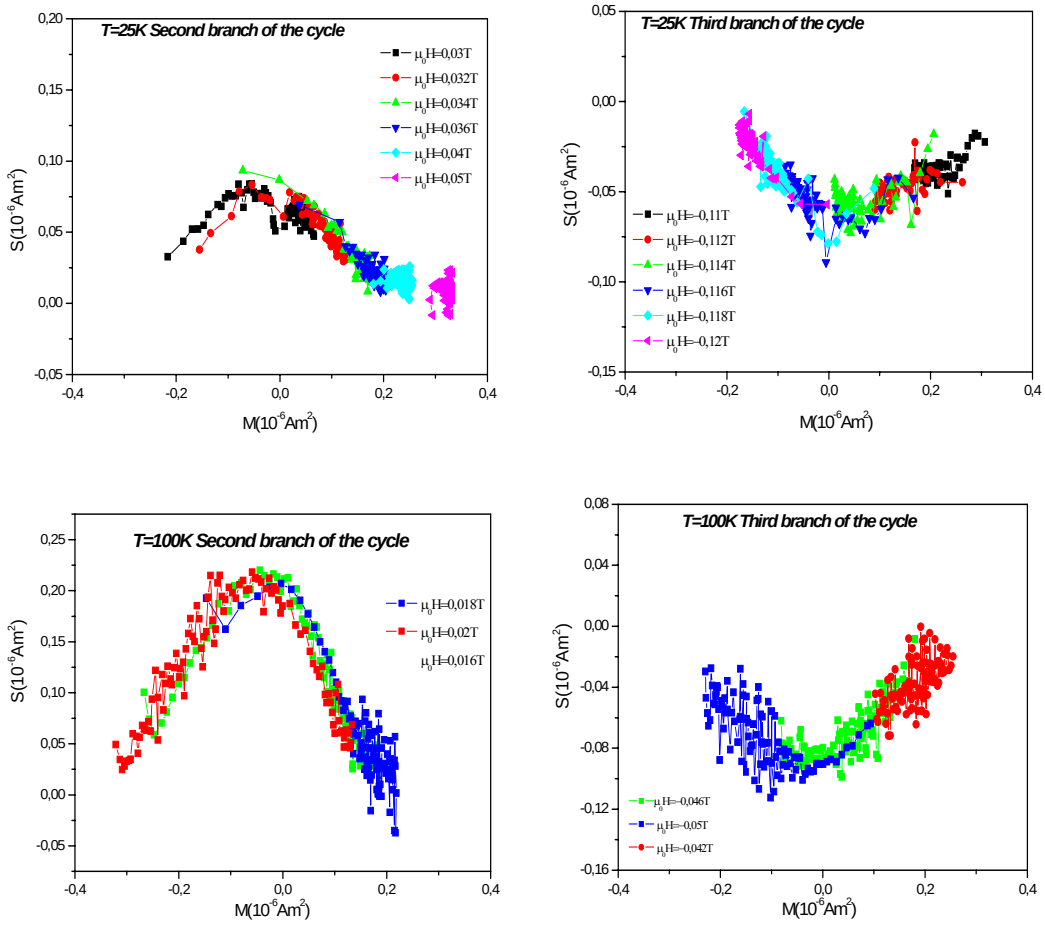

Figure 6.10. *Magnetic viscosity versus magnetization for sample S_2.*

An important feature already emerge: at a given temperature, the various S (M) curves measured under different applied fields constitute a unique curve.

The other parameter required to derive the magnetic viscosity coefficient $S_v = S / \chi_{tot} - \chi_{rev}$ is the susceptibility $\chi_{tot} - \chi_{rev} (\approx \chi_{irr})$. The χ_{rev} contribution was derived by small field excursions along the hysteresis cycle.

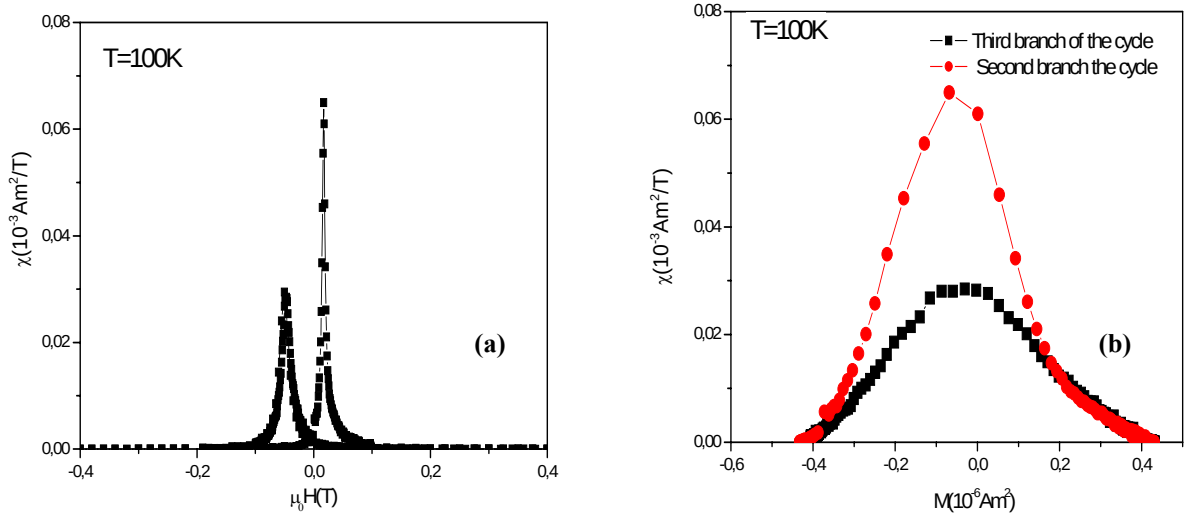

Figure 6.11. *a) Irreversible susceptibility χ_{irr} as a function of Field; b) Irreversible susceptibility χ_{irr} as a function of magnetization.*

From $\chi_{tot} - \chi_{rev}$ (H) shown in Figure 6.11 .a, $\chi_{tot} - \chi_{rev}$ (M) was derived (Figure 6.11.b).

At a given temperature, the magnetization dependence of $\chi_{tot} - \chi_{rev}$ matches exactly the S(M) (see Figure 6.12).

Altogether these striking results have several implications:

(i) The fact that magnetic viscosity and susceptibility may be compared when plotted as a function of the magnetization implies that along a given branch a given magnetic state of the system is determined to the first approximation by the magnetization value only.

(ii) The proportionality between S(M) and $\chi_{tot} - \chi_{rev}(M)$ establishes that magnetic after effect may adequately be represented by an effective magnetic field .

(iii) The fact that the magnetization dependence of $\chi_{tot} - \chi_{rev}$ mimics that of S implies that S_v is a constant (see Chapter 2, section.2.2.2.).This will be discussed further in the next section. Further, the S_v values obtained are about the same on both hysteresis cycle branches. This is illustrated in Figure 6.13. where S_v(T) is plotted from T=25K to T=100K.

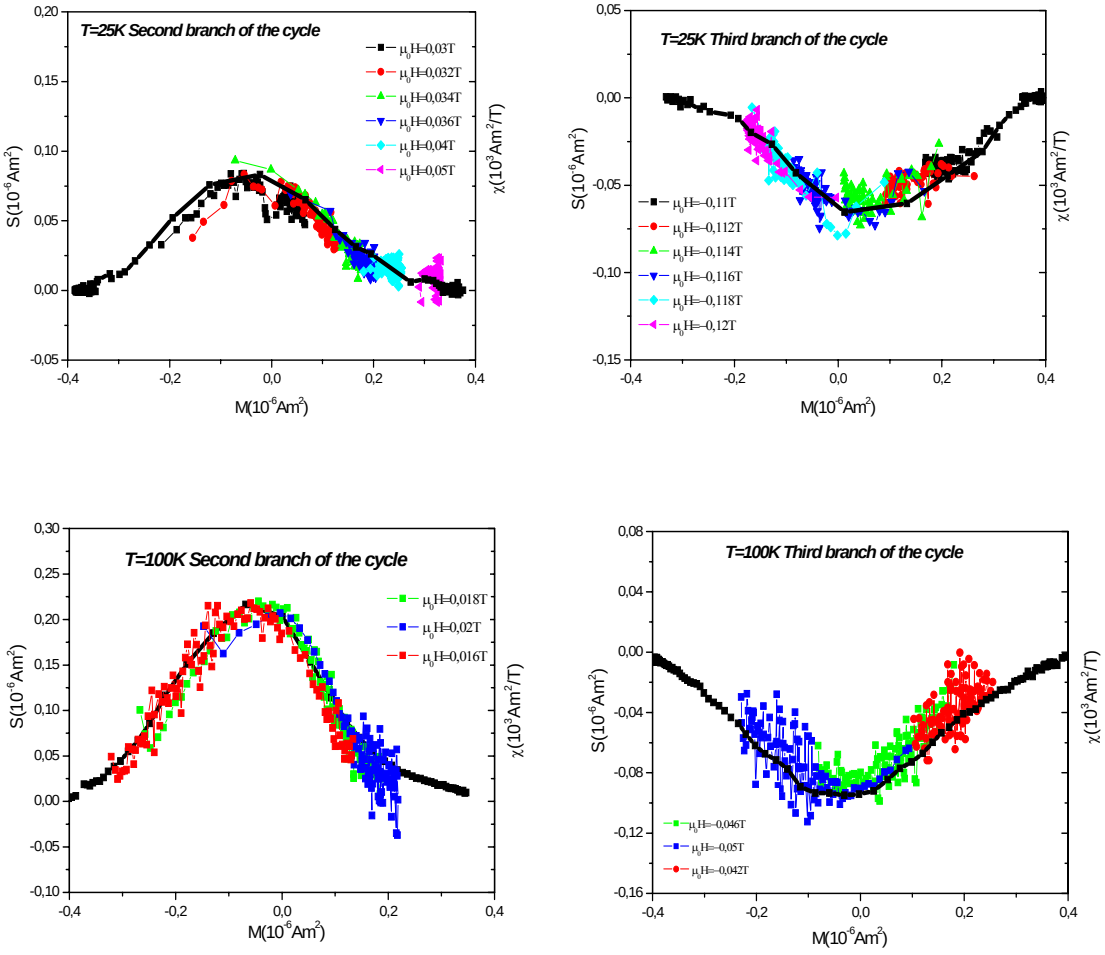

Figure 6.12. *Magnetic viscosity versus susceptibility for sample S_2.*

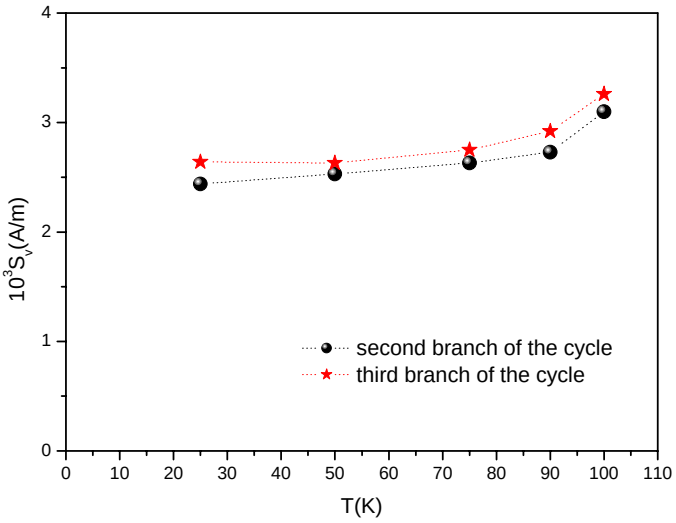

Figure 6.13. *Viscosity coefficient versus temperature on the 2nd and 3rd branch of the hysteresis cycle in sample S_2.*

6.2. Analysis and discussion of time dependent effects

6.2.1 Thermal activation on the 1st branch of the hysteresis cycle

As we already showed in section 6.1.1.and 6.1.2, the Fatuzzo- Labrune model describes the properties of the present systems along the 1st branch of the hysteresis cycle. Good agreement between experimental data and calculated ones was obtained when considering that the reversal on the first branch is dominated by nucleation over a single energy barrier (k ≈ 0).

Let Δ(H) be the height of the field dependent energy barrier. As shown by Victora [3] for an isotropic system, the energy barrier Δ involved in a thermally activated process may be expressed as:

$$\Delta(H) \propto (H_0 - H)^{3/2} \tag{6.4}$$

where H_0 refers to the energy barrier Δ_0 in zero applied magnetic field.

Δ(H) in relation (6.4) was approximated by $\Delta(H) = kT\ln(\tau/\tau_0)$ with $\tau = t_{50}/\ln 2$ and $\tau_0 = 10^{-9}s$, an arbitrary classical value. At each temperature T, $\Delta^{2/3}$ thus deduced was plotted as a function of (H_0-H) (Figure 6.14) .For such an exchange bias system, the reference H_0 field may be defined either with respect to the applied magnetic field or with respect to the bias field. In the former case, the energy barrier Δ_0 may be expressed phenomenological as:

$$\Delta_0 = v\mu_0 M_S H_0 \tag{6.5}$$

In the later case, the energy barrier Δ'_0 is given by the relation:

$$\Delta'_0 = v\mu_0 M_S H'_0 = v\mu_0 M_S (H_0 - H_B) \tag{6.6}$$

The energy barriers Δ_0 and Δ'_0 obtained at different temperatures are listed in Table 1.

T(K)	H_1(T)	H_E(T)	H_C(T)	Δ'_0 $*10^{-20}$J	Δ_0 $*10^{-20}$J	H_{0extr} (T)	H_0-H_E (T)	$v = \frac{\Delta_0}{\mu_0 M_S H_0}$ (nm^3)	$v = \frac{\Delta'_0}{\mu_0 M_S (H_0 - H_E)}$ (nm^3)
15	0,310	0,146	0,168	1,6	3,04	0,44	0,30	32	24
50	0,210	0,087	0,125	4,2	6,57	0,34	0,25	89	77
75	0,160	0,063	0,096	5,4	7,82	0,28	0,22	129	115
100	0,081	0,024	0,057	6,1	7,06	0,24	0,21	136	135
120	0,056	0,013	0,043	6,4	7,38	0,18	0,165	191	180

Table1. *Values of Δ_0 and Δ'_0 calculated by extrapolation to H=0 and to H=H_E respectively, in the case of sample S_1.*

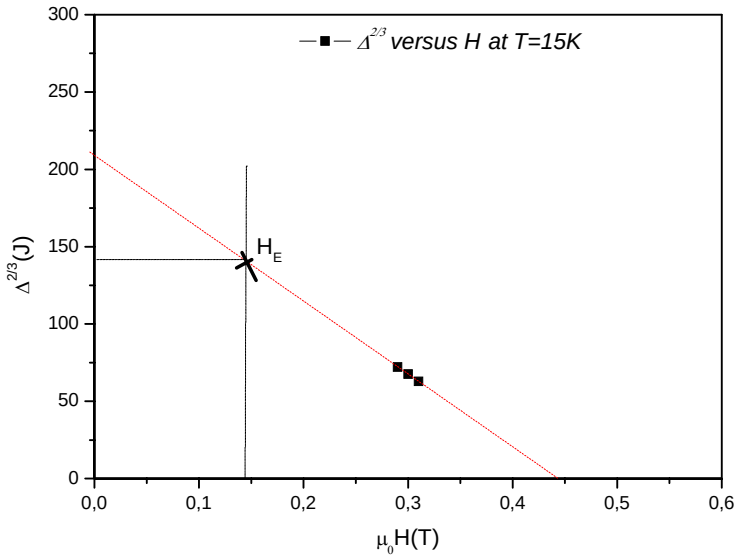

Figure 6.14. *$\Delta^{2/3}$ versus H at T=15K on the first branch of the hysteresis cycle for sample S_1.*

For both cases (Δ_0, H_0) and (Δ'_0, H'_0) the activation volume may be deduced. In principle the two values should obviously be identical. This is verified to $\pm$ 10%, except at T=15K where the two values differ by 30%.

The variation of the activation volume versus temperature on the first branch of the hysteresis cycle is presented in Figure 6.15.

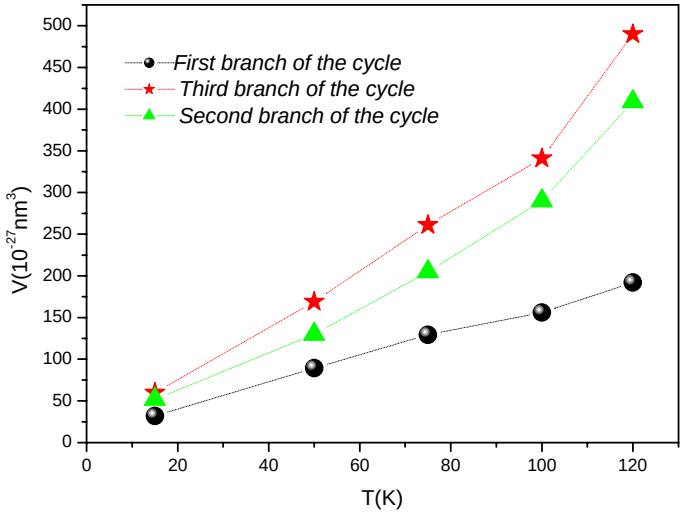

Figure 6.15. *Variation of the activation volume versus temperature on the first part of the cycle (in black) dominated by nucleation for sample S_1 .*

The activation volume increases with temperature, a property which is very generally observed in hard magnetic systems. Since domain wall nucleation involves the formation of a magnetization heterogeneity which must resemble a domain wall, it is usual to compare $v^{1/3}$ to the domain wall thickness. In the present case, $v^{1/3}$ increases from 3nm at T=15K to 6nm at T=120K.

6.2.2. Activation volume along the 2nd and 3rd branches of the cycle

The activation volumes versus temperature on the second and third branches of the cycle are plotted in Figure 6.16.for samples S_1 and S_2 .

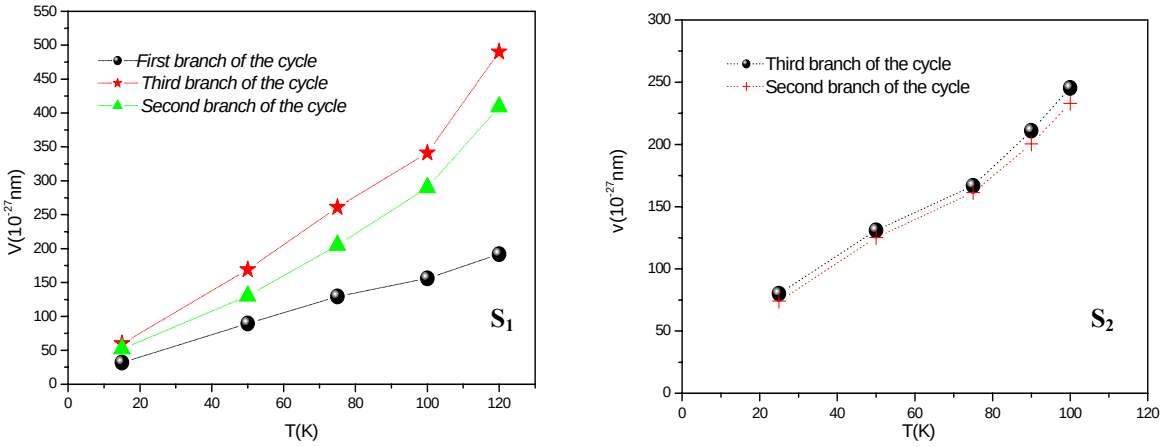

Figure 6.16. *Activation volume versus temperature for sample S_1 and S_2.*

As it was the case on the 1st branch of the hysteresis cycle, the activation volume increases with temperature.

Three main observations can be made:

- ✓ As already mentioned the activation volume has a constant value along a certain branch of the hysteresis cycle.
- ✓ At all measuring temperatures the activation volume has the same value along the 2nd and 3rd branches of the cycle.
- ✓ The activation volume is two to three times larger than along the 1st branch of the cycle.

6.2.3. General remarks concerning the activation volume

The viscosity coefficient is inversely proportional to the activation volume, $S_v = \frac{1}{v_a}$ (see relation 2.30). Further, as shown by Barbier [quoted by Wohlfarth in [4]] it is approximately proportional to the coercive field. Thus, it is natural to find a smaller value for the activation volume on the first branch of the hysteresis cycle (see Figure 6.16).

In hard magnets the activation volume is generally found to be of the order of $v \approx 10\delta^3$, where δ is the domain wall width (Nd_2Fe_4B $\delta \approx 5.3nm$, K=15MJ/m^3 at T=4.2K). In our Co/MnPd samples, $v_a \approx 80nm^3$ at T=15K, whereas, δ^3 for Co is much larger, of the order of $10^3 nm^3$.The coupling between the ferromagnetic and antiferromagnetic layer may be the source of an additional anisotropy. However, this will not influence δ and thus the expected value of v_a in this approach very significantly.

The above result suggests that in the present system, the activation volume as compared to δ^3 is smaller than in usual hard magnetic systems. This may be attributed to the highly disordered nature of the interface structure. Several authors [5, 6] have shown that exchange bias systems present properties which are reminiscent of spin- glass systems. In such systems, it is well known that a number of states with similar energies exist and the magnetization variation occurs by overcoming a large number of small energy barriers.

The large distribution in reversal fields which is seen on the hysteresis cycle is related in usual hard magnets to a distribution of energy barriers and a distribution in activation volume should be found as well. By contrast, the constant value of the activation volume found here indicates that the distribution in reversal field is not due to a distribution in energy barrier. A natural way to account for this is to assume that there exists a distribution in bias fields, which would lead to a distribution in the total local field acting on the ferromagnetic moments. The identical values in the activation volume along the two other branches of the hysteresis cycle may be interpreted with the same argument.

6.2.4. Coercive field model along the 2nd and 3rd branches of the cycle

In the case of hard magnets, Givord *et al*. [7] showed that (see section 2.2.3 in chapter 2), the activation volume may be related to the coercive field through the following relation:

$$\mu_0 H_R = \alpha \frac{A}{v^{2/3} M_S(T)} - \mu_0 N_{eff} M_S \qquad (6.7)$$

where the first term represents the coercivity strength and the second term represents dipolar interactions within matter.

We have applied the same approach to the studied Co/MnPd systems. The coercive field versus $1/v_a^{2/3}$ for sample S_1 and S_2 is shown in Figure 6.17.

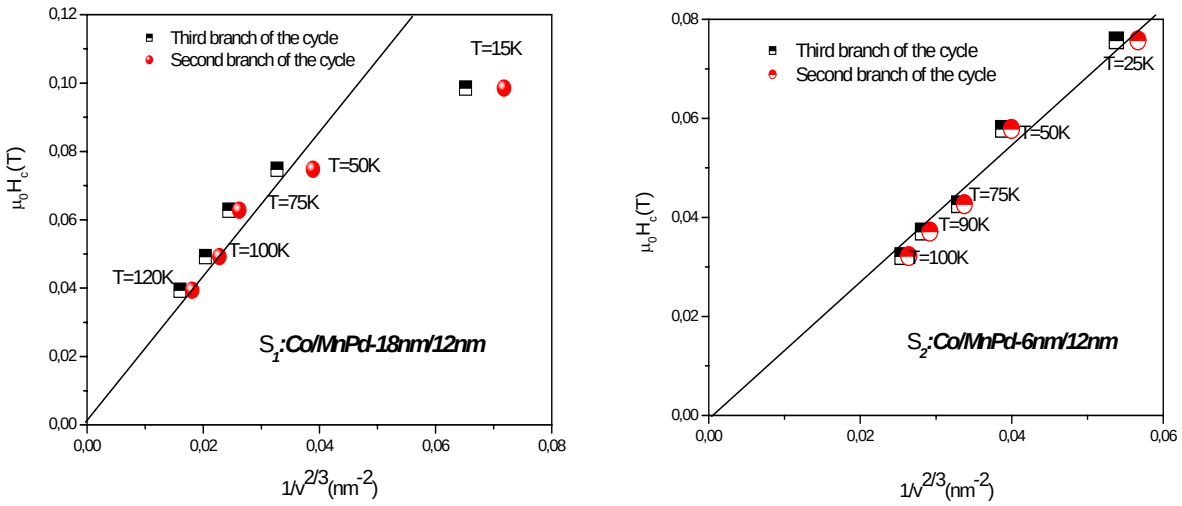

Figure 6.17. *Activation volume $V^{2/3}$ versus coercive field in samples S_1 and S_2.*

An approximate linear variation is obtained (except for the points corresponding to measurements at T=15K in sample S_1) and the line cut the axes at origin. In the present case, the exchange constant A= A_{Co} =10^{-11}J/m and the saturation magnetization M_S = M_{Co} = 1.37*10^6A/m. The phenomenological parameters α and N_{eff} are derived to be: α= 0,2 and N_{eff} =0.

The parameter α is significantly weaker than in usual hard magnets. This is not surprising when considering the highly disordered nature of the studied systems so that reversal involves a large distribution of relatively weak barriers.

The value N_{eff}= 0 means that reversal is not significantly influenced by dipolar interactions. This is often found in systems where magnetization reversal involves propagation of domain wall.

Altogether this analysis indicates that magnetization reversal in exchange bias systems resemble the one in hard magnets.

References-Chapter 6

[1] E.FATUZZO, *Theoretical considerations of the switching transient in ferroelectrics,* Phys. Rev. vol.127, p1999 (1962).

[2] M.LABRUNE, S.ANDRIEU, F.RIO, *Time dependence of magnetization process of RE-TM alloys,* J. Magn. Magn. Mater. vol.80, p211 (1989).

[3] R.H.VICTORA, *Predicted time dependence of the switching field for magnetic materials,* Phys. Rev. Lett. vol.63, p457 (1989).

[4] E.C.STONER, E. P.WOHLFARTH, *A mechanism of magnetic hysteresis in heterogeneous alloys,* Phil. Trans. Roy. Soc, vol. A240, p599 (1948).

[5] N.S.AJDHIYE, S.BHATTACHARYYA, *Exchange bias and spin-glass like ordering in ε-Fe_3N-CrN nano composites,* J.J.Apl.Phys.vol.46, p980 (2007).

[6] M.GRUYTERS, *Spin glass like behaviour in CoO nanoparticles and the origin of exchange bias in layered CoO/Ferromagnet structures,* Phys.Rev.Let, vol.95, p077204 (2005).

[7] D.GIVORD, M.ROSSIGNOL, V.M.T.S.BARTHEM, *The physiscs of coercivity,* J. Magn. Magn. Mater. vol.1-5, p258 (2003).

Conclusion

In this thesis, I have studied **exchange-bias** in three different Co/MnPd samples.

Having analysed the results obtained in various exchange-bias systems previously studied as well as models developed to describe this phenomenon, I embarked on the study of a system which was a priori well adapted to the study exchange-bias in the whole temperature range from low T up to the Néel Temperature of the antiferromagnet.

Unfortunately it turned out to be difficult to characterise properly the structural and magnetic properties of the MnPd antiferromagnetic layer. Thus, we were led to assume that this layer had the same properties (magnetic structure in particular) as reported for MnPd alloys of similar composition [1, 2, 3]. The exchange-bias field, H_E, and coercive field, H_c, were determined in the whole temperature range, up to T_N of MnPd. The value of the interfacial coupling energy was found to be significantly larger than in most exchange-bias systems previously studied. In a certain temperature range (T=120K-130K), the bias-field H_E could be increased under a sufficiently large field applied at a given temperature. By contrast, above 130K, the exchange-bias field was found to be reduced under H_{app}. These features, never observed previously, indicate that the interfacial AFM moment configuration is modified under H_{app}.

In view of approaching the physical understanding of exchange-bias, a simple phenomenological model of exchange-bias was developed, in which the interfacial molecular field created by the ferromagnet on the antiferromagnet was modelled essentially as an external applied field. This model has similarities with the Koon's or Schulthess and Butler's approaches. However, an unexpected result was to show that for a range of realistic molecular field coefficient, the moments in the first antiferromagnetic layer almost aligns along the ferromagnetic moments. This has very significant consequences for the coupling mechanism. A striking feature is to suggest that the H_E field may be determined by the coupling existing between the first and the second antiferromagnetic layers. Exchange bias fields which are consistent with experimental values are then obtained.

Magnetic after effect was studied in great detail for the first time in an exchange -bias system. We showed that the Fatuzzo-Labrune model permits thermal activation to be described along the first branch of the hysteresis cycle. This implies that reversal is governed by nucleation over a very small number of barriers. Along the second and further branches of the hysteresis cycle, magnetization reversal involves overcoming energy barriers which are characterised by a broad energy distribution so that the models which are usually used to describe magnetization reversal in hard magnetic materials are now adequate.

Conclusion

A striking difference with usual hard magnets, is the fact that a very large fraction of the hysteresis cycle may be described by thermal activation alone under fixed applied magnetic field. This property is related to the very small size of the activation volume ($v \approx \delta^3$, instead of $v \approx 10\ \delta^3$), a property which characterises more generally highley disordered systems, such as spin glasses [4, 5]. Further this large thermal activation effect permitted us to reveal the validity of the usual analogy made between the effects of thermal activation and those of an applied magnetic field.

As final concluding remarks, I would like to indicate possible directions of research which could be initiated to progress further into the understanding of exchange-bias. In particular, it would be meaningful to test the generality of results obtained in this work by examining other exchange-bias systems. This would permit to test the validity of the model proposed in our work, as well as to examine whether the original features of magnetic after effect found in MnPd/Co exist in other EB systems as well. Additionally, in the spirit of the Malozemoff's description of exchange-bias, the magnitude of the uncompensated interfacial antiferromagnetic moment is determined by the size of some characteristic correlation length of the system. In this respect, the study of exchange-bias in nanostructures, may offer another promising approach to the understanding of this phenomenon. Very few results were already published on this topic, and they are often contradictory. This type of studies is now being developed in Institut Néel.

Conclusion

Dans cette thèse, j'ai étudié le phénomène de décalage d'échange dans trois échantillons différentes de Co / MnPd.

Après avoir analysé les résultats obtenus dans les différents systèmes a la décalage d'échange précédemment étudié, ainsi que les modèles développés pour décrire ce phénomène, j'ai entrepris l'étude d'un système qui était a priori bien adapté à l'étude de exchange bias dans une grande gamme de température a partir de basse température jusqu à la température Néel du couche antiferromagnétique.

Malheureusement, il s'est difficile de caractériser correctement les propriétés structurales de la couche antiferromagnétique MnPd. Ainsi, nous avons été amenés à penser que cette couche as les mêmes propriétés magnétiques (structure magnétique en particulier) comme indiqué pour les alliages MnPd de composition similaire [1, 2, 3]. Les valeurs du champ bias H_E, et du champ coercitif, H_C ont été déterminées dans toute la plage de température, jusqu'à la température Néel T_N du MnPd. La valeur de l'énergie interfaciale d'échange est sensiblement plus importante que dans la plupart des systèmes d'échanges précédemment étudiés. Dans une certaine plage de température (T = 120K-130K), la valeur du champ bias H_E, augmente pour une certaine valeur du champ appliqué et pour une température donnée. En revanche, au-dessus de 130K, la valeur du champ bias H_E était réduite sous H_{app}. Ces caractéristiques, jamais observé auparavant, indiquent que la configuration interfaciale de moment AFM est modifiée sous H_{app}.

Pour une meilleure compréhension des phénomènes physiques implique dans le phénomène de décalage d'échange, un simple modèle phénoménologique a été développé, dans lequel le champ moléculaire interfacial créé par la couche ferromagnétique sur la couche antiferromagnétique a été modélisé essentiellement comme un champ externe appliquée. Ce modèle présente des similitudes avec les approches du Koon ou Schulthess et Butler. Toutefois, un résultat inattendu a été montré : pour des valeur réaliste du cœfficient champ moléculaire, les moments dans la première couche antiferromagnétique sont presque alignée le long des moments ferromagnétiques. Ceci a des conséquences très importantes pour le mécanisme d'échange. Une caractéristique frappante est de suggérer que le champ bias H_E peut être déterminé par le couplage existant entre la première et la deuxième couches antiferromagnétique. Des valeur compatibles avec les valeurs expérimentales sont alors obtenus pour le champ d'decalage.

Les effet traînage magnétique on été étudié dans le détail pour la première fois dans un système a la décalage d'échange. Nous avons montré que le model de Fatuzzo-Labrune permet la description de l'activation thermique sur la première branche du cycle d'hystérésis.

Cela implique que le renversement est dominé par la nucléation sur un très petit nombre de barrières d'énergie. Pour les deuxième et troisième branches du cycle, le renversement d'aimantation implique la surmonte des barrières d'énergie caractérisés par une large distribution de l'énergie afin que les modèles qui sont généralement utilisés pour décrire la renversement de l'aimantation en matériaux magnétiques durs sont désormais adéquates.

Une différence frappante par rapport ou aimants durs habituels, c'est le fait qu'une très grande partie du cycle d'hystérésis peut être décrit par l'activation thermique sous un champ magnétique appliqué fixe. Cette propriété est liée à la très petite taille du volume d'activation ($v \approx \delta^3$ par rapport au $v \approx 10\delta^3$) une propriété qui caractérise les systèmes très désordonnés, comme les verres de spin [4, 5]. Ce large effet d'activation thermique nous a permis de faire un lien entre les effets de l'activation thermique et celles d'un champ magnétique appliqué.

Comme dernière conclusion, je tiens à indiquer les orientations possibles dans la recherche qui pourrait être entrepris pour progresser dans la compréhension des systèmes à la décalage d'échange. En particulier, il serait utile de tester la généralité des résultats obtenus dans ce travail en examinant d'autres systèmes de type exchange bias. Cela permettrait de tester la validité du modèle proposé dans nos travaux, ainsi que d'examiner si les caractéristiques originaux des effet traînage trouvée dans MnPd / Co existent dans d'autres systèmes. Dans l'esprit du model du Malozemoff, l'ampleur des moments interfacials antiferromagnétiques noncompensée est déterminée par la taille de certaines longueurs caractéristiques du système. À cet égard, l'étude de décalage d'échange dans les nanostructures, peut offrir une autre approche prometteuse pour la compréhension de ce phénomène. Très peu de résultats ont été publiés sur ce sujet, et ils sont souvent contradictoires. Ce type d'études est en cours de développement dans l'Institut Néel.

References-Conclusions

[1] K.BABA, Y.NIKI, Y.SAKAMATO, *The phase transition in palladium-manganese alloys with up to 33,3at.% Mn*, J. of. Alloys and Compounds vol.179,p321 (1992).

[2] E.KREAN, G.KADAR, *Crystal and magnetic structures in the Mn-Pd system near $MnPd_3$* , Phys. Lett. vol. 29A, p340 (1969).

[3] E.KREAN, G.KADAR, M.MARTON, *Neutron diffraction study of the $MnPd_3$ phase,* Sol.Stat.Com. vol.10, p1195 (1972).

[4] N.S.AJDHIYE, S.BHATTACHARYYA, *Exchange bias and spin-glass like ordering in ε-Fe_3N-CrN nano composites,* J..Apl.Phys.vol.46,p980 (2007).

[5] M.GRUYTERS, *Spin glass like behaviour in CoO nanoparticles and the origin of exchange bias in layered CoO/Ferromagnet structures,* Phys.Rev.Let, vol.95, p077204 (2005).

List of Figures

Figure 1.1. Hysteresis loops at 77K of partially oxidized Co particles. 17

Figure 1.2. Schematic diagram of the spin con-figuration of an FM/AFM bilayer at different stages (i) - (v) of an exchange- bias hysteresis loop 18

Figure 1.3. Hysteresis loop, m(H), of FeF_2/Fe bilayer at T=10K after cooling. 19

Figure 1.4. Hysteresis loops for a FeF_2/Fe bilayer at T=10K cooled in zero field from T=85K in different magnetization states..... 20

Figure 1.5. Dependence of exchange bias H_E (square symbols) and coercivity H_C (triangular symbols) for the [111]oriented sample for 32 and 70Å $Ni_{80}Fe_{20}$ systems 22

Figure 1.6. Dependence of exchange bias H_E (square symbols) and coercivity HC (triangular symbols) for the [011]oriented sample for 32 and 70Å $Ni_{80}Fe_{20}$ systems 22

Figure 1.7. Exchange bias field H_E and coercive field H_C versus measurement temperature for two permalloy (200Å)/CoO samples..... 23

Figure 1.8. Hysteresis loop for the Fe-MnF_2 sample and the orientation of the cooling field, H_{FC}= 0,64T, relative to the MnF_2domains..... 24

Figure 1.9. Magnetic hysteresis loops of (a) a uniform FeF_2(200 Å)/Fe(150 Å)/Al(40 Å) film, and (b) a uniform FeF_2(200 Å)/networked-Fe(150 Å)Al(40 Å) at 10 K, after field cooling in 0.5T from 300 K. 24

Figure 1.10. Coercive fields for the increasing field branch, H_α, and decreasing field branch, H_β, of the hysteresis loop as a function of measurement order, n, for an Fe20Ni80/ FeNiMn bilayer at room temperature 25

Figure 1.11. Schematic diagram of angels involved in an exchange-bias system 27

Figure 1.12. Magnetic model for the interface of a thin ferromagnetic film on a thick antiferromagnetic substrate 28

Figure 1.13. Schematic side view of FM/AFM bilayer with FM domain wall driven by an applied field..... 30

Figure 1.14. Schematic view of a vertical domain wall in the AFM layer 31

Figure 1.15. (a) Magnetic structure of a <1 1 0 > oriented AFM body centered tetragonal crystal. (b) Lowest energy spin configuration near the interface plane. 32

Figure 1.16. Energy per unit area of a 15/15ML (110) FM/AFM bilayer as a function of the angle between FM and AFM magnetization axes. ……………………..………..……. ..……33

Figure 1.17. Spin configuration of the AFM interface monolayer and both the FM and the two AFM monolayers closest to the interface, after it is field-cooled through T_N. …………………………………………………………………….……….………..……….......34

Figure 1.18. Schematic diagram showing line defects [(a) and (b)] and step defects [(c) and (d)] at compensated and uncompensated interfaces 36

Figure 1.19. The natural angle θ_{nat} as a function of defect spacing for compensated and uncompensated interfaces. 37

Figure 2.1. Energy barrier at the origin of coercivity in the Stoner-Wohlfarth model…...............45

Figure 2.2. Schema of the nucleation and expansion process. .... …..46

Figure 2.3. Schematic view of the energy barriers overcome by the domain wall ……….........48

Figure 2.4. Schematic view of the energy states. .... …49

Figure 2.5. Temperature dependence of the mean nucleation (Hn_1) and propagation fields (Hp) for a GdFe(1000 Å)/TbFe(2 Å)/GdFe(500 Å). 50

Figure 2.6. Scheme of Magnetization reversal by nucleation (a), propagation (b, c) and coalescence (d). 51

Figure 2.7. (a) Magnetization change versus time for different applied field; (b) same curves expressed in reduced time t_R. 52

Figure 2.8. Calculated magnetization reversal curves for different values of the parameter k….53

Figure 2.9. Energy function associated to the energy barrier 55

List of Figures

Figure 3.1. RF sputtering principle. 61

Figure 3.2. Pd target with square Mn chips bonded to it..... 62

Figure 3.3. The target configuration of sputtering machine: (a) Magnetron type; (b) Facing targets type 63

Figure 3.4. Schematic view of XRD measurements in the θ-2θ mode.. 64

Figure 3.5. Schematic drawing of the electron source…… …….. 65

Figure 3.6. Example of an EXD spectrum 67

Figure 3.7. Schematic view of the energy shells……..…….67

Figure 3.8. θ/2θ -Scan: The condition of incident angle ω = (2θ)/2 = θ - outgoing angle is satisfied ..... ….68

Figure 3.9. Measuring coil of an VSM…….…….73

Figure 3.10. Schematic view of the operating principle of the SQUID 74

Figure 3.11. Cross Section of the SQUID. 75

Figure 4.1. Various Mn-Pd phases appearing in the composition range between Pd-10% Mn and Pd-33,3% Mn 79

Figure 4.2. The room temperature lattice parameters of the α phase in Pd-Mn alloys as a function of manganese content, together with previously reported results 80

Figure 4.3. Scheme illustrating the stacking of the layers constituting the various samples……81

Figure 4.4. X-ray diffraction measurement for the 180nm MnPd film……. ….....82

Figure 4.5. EDX spectrum for the MnPd sample with t=180nm 83

Figure 4.6. SEM observation on the Co/ MnPd films. 84

Figure 4.7. EDX spectrums for the sample S_1, S_2 and S_3……. ……85

Figure 4.8. X-ray specular reflectivity and fit for sample S_1. 87

Figure 4.9. X-ray specular reflectivity and fit for sample S_2……..……88

Figure 5.1. Hysteresis cycle measured at T=15K (sample S_2)……..……91

List of Figures

Figure 5.2. Ireversible susceptibility versus applied magnetic field for sample S_2 at T=15K…….. …….. ……..….....92

Figure 5.3. (a). Irreversible susceptibility values versus magnetization for sample S_2 at T=15K. **(b).** Irreversible susceptibility values versus magnetization for sample S_2 at T=100K…….. …….. …….93

Figure 5.4. Hysteresis cycles measured at different temperatures on sample S_2…….....94

Figure 5.5. (a) Field values versus temperature for samples S_1. **(b)**Bias field and coercive field versus temperature for samples S_1……...……..95

Figure 5.6. (a) Field values versus temperature for samples S_2. **(b)**Bias field and coercive field versus temperature for samples S_2…….. ……..95

Figure 5.7. (a) Field values versus temperature for samples S_3. **(b)**Bias field and coercive fie-ld versus temperature for samples S_3.……..…….……..96

Figure 5.8. Irreversible susceptibility values versus temperature for sample S_1 and S_3 on diffe-rent branches of the hysteresis cycle…….. ……..96

Figure 5.9. The coercivity and exchange bias field of as-deposited MnPd/Co bilayers versus MnPd thickness measured at 15 K.……....……97

Figure 5.10. Hysteresis loops of sample S_1 as a function of the cooling tempera-ture…….....….98

Figure 5.11. Values of the reversal field as a function of the cooling temperature, under a field of 0.4T……..……...99

Figure 5.12. Hysteresis cycles measured at T=120K and T=130K for sample S_2 ……...……....….....100

Figure 5.13. Hysteresis cycles measured at T=130K and T=140K for sample S_2. …….....…….101

Figure 5.14. Magnetic moment versus applied field for $Gd_2(SO_4)_3$ *8 H_2O at a given temperature……...……....……..102

Figure 5.15. Schematic wiev of the angle notation used in the model... ... ... ……....….106

Figure 5.16. Calculated values for $\theta_{AFM1,}$ θ_{AFM2} in a fully compensated case and different uncompensated situations.……....…….107

List of Figures

Figure 5.17. Scheme of the spin configuration in an uncompensated layer in order to obtain bias field…….. ……..…….109

Figure 5.18. Bias field versus molecular field coefficient W_{A-F}…….. ……...…110

Figure 6.1. Hysteresis cycle measured at T=50K for sample S_1 showing the knee at $\mu_0 H$= -0,21T on the first branch of the hysteresis cycle…...……...……...…….114

Figure 6.2. Variation of magnetization versus time at T=50K for sample S_1……..….....114

Figure 6.3. (a) Normalized experimental curves $b(t_R)$versus t obtained for different field values. (b) Normalized experimental curves $b(t_R)$versus t_R obtained for different field values…...….....115

Figure 6.4. Normalized experimental curves obtained for different field values and temperature values up to T=120K…..……...….....116

Figure 6.5. Experimental curve versus theoretical curves obtained with Fatuzzo- Labrune's model for the first branch of the hysteresis cycle.....…….117

Figure 6.6. Hysteresis cycle measured at T=100K for sample S_1 (the fields at which magnetic after effect was measured are indicated by crosses)……...…….118

Figure 6.7. Variation of magnetization function of time in sample S_1 on the second and third branch of the hysteresis cycle at T=100K……..……...….....118

Figure 6.8. Normalized experimental data for the2nd and 3rd branch of the hysteresis cycle at T=100K……...……...……...……..119

Figure 6.9. Magnetization dependence versus lnt for sample S_2 at T=25K and T=100K on the 2nd and 3rd branch of the hysteresis cycle…. ……...……...120

Figure 6.10. Magnetic viscosity versus magnetization for sample S_2…...……...…….120

Figure 6.11.a) Irreversible susceptibility χ_{irr} as a function of Field; b) Irreversible susceptibility χ_{irr} as a function of magnetization.……...……..121

Figure 6.12. Magnetic viscosity versus susceptibility for sample S_2 ……...…..122

Figure 6.13. Viscosity coefficient versus temperature on the 2nd and 3rd branch of the hysteresis cycle in sample S_2……..122

Figure 6.14. $\Delta^{2/3}$ versus H at T=15K on the first branch of the hysteresis cycle for sample S_1. ……..….....124

List of Figures

Figure 6.15. Variation of the activation volume versus temperature on the first part of the cycle (in black) dominated by nucleation for sample S_1 …….……...…124

Figure 6.16. Activation volume versus temperature for sample S_1 and S_2……...…...125

Figure 6.17. Activation volume $V^{2/3}$ versus coercive field in samples S_1 and S_2. ……...…127

List of symbols and abbreviations

AMR	Anisotropic Magnetoresistance
AFM	Antiferromagnetic/Antiferromagnet
EDX	Energy Dispersive X-Ray
EB	Exchange bias
FC	Field Cooling
FM	Ferromagnetic/Ferromagnet
FMR	Ferromagnetic Resonance
GMR	Giant Magnetoresistance
HD	Hard Disk
MRAM	Magnetic Random Access Memory
MB	Meiklejohn and Bean's model
PEB	Positive Exchange Bias
SEM	Scanning Electron Microscope
VSM	Vibrating sample magnetometer
XRD	X-ray Diffraction
ZFC	Zero Field Cooling
α	Angle between M_{AFM} and AFM anisotropy axis
β	Angle between M_{FM} and the FM anisotropy axis
φ	Angle between applied field and cooling field
μ_B	Bohr magnetron
J	Interface exchange
θ	Angle between H and the FM anisotropy axis
ξ	Thickness of the interface between AFM and FM
ΔE	Interface energy
A	Exchange stiffness
a	Lattice constant
M	Magnetization
g	Gyromagnatic ratio
H_{appl}	Applied magnetic field
H_R	Reversal field
H_{dip}	Dipolar field
H_n	Nucleation field
Hc	Coercive field
H_{pass}	Passage field
H_{depin}	Depinning field
H_{expans}	Expansion field
H_E	Exchange bias field

List of symbols and abbreviations

H_{FC}	Cooling field
J_{AFM}	AFM exchange interaction constant
J_{FM}	FM exchange interaction constant
M_r	Remanent magnetization
K_{AFM}	AFM anisotropy constant
K_C	Cubic anisotropy
K_E	Exchange anisotropy
K_{FM}	FM anisotropy constant
K_U	Uniaxial anisotropy
T_B	Blocking temperature
T_C	Curie temperature
T_N	Néel temperature
t_{AFM}	Thickness of AFM layer
t_{FM}	Thickness of FM layer
Θ_{nat}	Natural angle

EXCHANGE BIAS IN **Co/MnPd** SYSTEM

Abstract:

This thesis concerns the study of Co/MnPd an **exchange-biased** system.

The samples were structurally characterised using X-ray diffraction and reflectometry and magnetically VSM and SQUID magnetic measurements.

In view of approaching the physical understanding of exchange-bias, a simple phenomenological model of exchange-bias was developed, in which the interfacial molecular field created by the ferromagnet on the antiferromagnet is essentially equivalent to an external applied field. A striking feature is to show that the H_E field is determined by the coupling existing between the first and the second antiferromagnetic layers. Exchange bias fields which are consistent with experimental values are then obtained.

Magnetic after effect was studied in great detail for the first time in an exchange -bias system. We showed that the Fatuzzo-Labrune model permits thermal activation to be described along the first branch of the hysteresis cycle. This implies that reversal is governed by nucleation over a very small number of barriers. Along the second and further branches of the hysteresis cycle magnetization reversal involve overcoming of energy barriers which are characterised by a broad energy distribution so that the models which are usually used to describe magnetization reversal in hard magnetic materials are now adequate.

Keywords:
magnetism, magnetic measurements, model, thermal activation, nucleation, propagation, magnetic after effect, energy barrier.

DECALAGE D'ECHANGE DANS LE SYSTEME **Co/MnPd**

Résume :

Ce travail de thèse porte sur l'étude du décalage d'échange dans le system Co / MnPd.

Les échantillons ont été caractérisée structuralement en utilisant la diffraction et la réflectométrie de rayons X et magnétiquement en utilisant un magnétomètre VSM et un magnétomètre SQUID pour les mesures magnétiques.

Compte tenu de la difficulté dans la compréhension des phénomènes physiques impliqués dans le décalage d'échange, un modèle phénoménologique simple a été développé dans lequel le champ magnétique moléculaire sur la couche antiferromagnétique est modélisé comme un champ magnétique extérieur appliqué. La valeur du champ de décalage est déterminée par le couplage existant entre la première et la deuxième couche AFM.

L'étude des effets traînage dans les systèmes à décalage d'échange, constitue une originalité de ce travail. Le modèle de Fatuzzo Labrune, très souvent utilisé pour décrire le renversement de l'aimantation dans les couches magnétiques dures a permis la description de l'activation thermique sur la première partie du cycle dé hysteresis. Ce modèle est valable lorsqu'on considère une seule barrière d'énergie dans la nucléation des domaines magnétiques et une seule barrière pour la propagation des parois. Au delà du premier cycle d'hysteresis, les résultat expérimentaux ne peuvent être décrits par ce modèle. Les modèles qui supposent l'existence d'une large distribution des barrières d'énergie permet alors une très bonne description des effets observés.

Mots clés :
magnétisme, mesures magnétique, model, activation thermique, nucléation, propagation, traînage magnétique, barrière d'énergie.